

# Neutron Generation in Dense Femtosecond Laser Plasma of a Structured Solid Target

R. V. Volkov\*, D. M. Golishnikov\*, V. M. Gordienko\*, P. M. Mikheev\*, A. B. Savel'ev\*\*,\*\*\*, V. D. Sevast'yanov\*\*\*, V. S. Chernysh\*, and O. V. Chutko\*

\* International Laser Center, Faculty of Physics, Moscow State University, Vorob'evy Gory, Moscow, 119899 Russia

\*\* e-mail: savelev@femto.phys.msu.su

\*\*\* All-Russia Research Institute of Physicotechnical and Radio Engineering Measurements, Mendeleevo, Moscow region, 141570 Russia

Received September 8, 2000

We report neutron production by the  ${}^2\text{H}(d, n){}^3\text{He}$  reaction induced upon the illumination of a solid nanostructured target by femtosecond laser pulses of intensity  $20 \text{ PW/cm}^2$  ( $1 \text{ PW} = 10^{15} \text{ W}$ ). The target was structured through the preliminary illumination by a laser pulse of the same intensity. © 2000 MAIK "Nauka/Interperiodica".

PACS numbers: 25.45.-z; 25.60.Pj; 29.25.Dz; 52.40.Nk; 52.50.Jm

1. In recent years, the observation of the processes occurring in plasma produced by a subpicosecond laser pulse has been reported in a number of works. Among these are nuclear activation, laser-induced nuclear fission [1–3], thermonuclear reactions, and neutron generation [4–6].

Neutrons produced by the  ${}^2\text{H}(d, n){}^3\text{He}$  reaction in laser plasma were first observed in work [7] devoted to controlled thermonuclear fusion. Compared to plasma produced by a nanosecond or subnanosecond laser pulse, a high rate of energy absorption in a solid material in the case of a femtosecond (subpicosecond) laser pulse (even at a relatively low energy of 0.1–100 mJ) leads to an "instantaneous" heating of plasma electrons to temperatures higher than 1000 eV. However, most experiments [2, 3, 5, 6] with ultrashort laser pulses were carried out in the so-called relativistic regime of interaction between radiation and matter with intensities higher than  $10^{18} \text{ W/cm}^2$ . At the same time, the use of tabletop femtosecond systems operating in the non-relativistic interaction regime opens up the way to practical use of neutron and other ultrashort-duration sources.

This work reports neutron production by the  ${}^2\text{H}(d, n){}^3\text{He}$  reaction in a solid nanostructured target irradiated by a femtosecond laser pulse of intensity  $20 \text{ PW/cm}^2$  ( $1 \text{ PW} = 10^{15} \text{ W}$ ).

2. The ions in plasma produced by an ultrashort laser pulse are heated to temperatures of 10–100 eV in 1–10 ps due to the electron-ion collisions. At such ion temperatures, thermonuclear reaction rates are low [8]. At the same time, as a result of the plasma free expansion, ion energy may become as high as tens of kilo-

electronvolts. To produce plasma with a near-solid density and high ion temperature, we proposed in [9] to use nanostructured targets. In such targets, an ultrashort laser pulse may initiate explosion of some structural elements, each one being scattered in a three-dimensional fashion. The collisions of ion "jets" give rise to the cumulative effect and lead to the formation, within 100–500 fs, of plasma with an ion temperature higher than 10 keV.

Up to now, neutrons produced by thermonuclear reactions in ultrashort pulse plasma have been observed for the case of a low plasma average density, on the order of and below its critical value. In [4], the ion component was heated in a plasma channel formed upon relativistic self-focusing of the laser pulse. A different approach is based on the fast heating of jets of nanometer-sized clusters to induce their Coulomb explosion and generate light ions with energies as high as 10 keV. Collisions of the deuterium ions from different clusters initiate the  ${}^2\text{H}(d, n){}^3\text{He}$  reaction yielding neutrons [6]. However, since the plasma average density is low, the reaction yield is also low because the number  $N_n$  of neutrons produced in plasma is proportional to the square of the deuteron density  $n_D$ :

$$N_n \approx 0.25 n_D^2 \langle \sigma v \rangle_{DD} \tau V, \quad (1)$$

where  $\tau$  is the lifetime of the dense plasma and/or the time of its cooling,  $V$  is the plasma volume, and  $\langle \sigma v \rangle_{DD}$  is the thermonuclear reaction rate averaged over the Maxwellian distribution [8].

In [9], we suggested using solid nanostructured deuterium-saturated targets for the neutron generation.

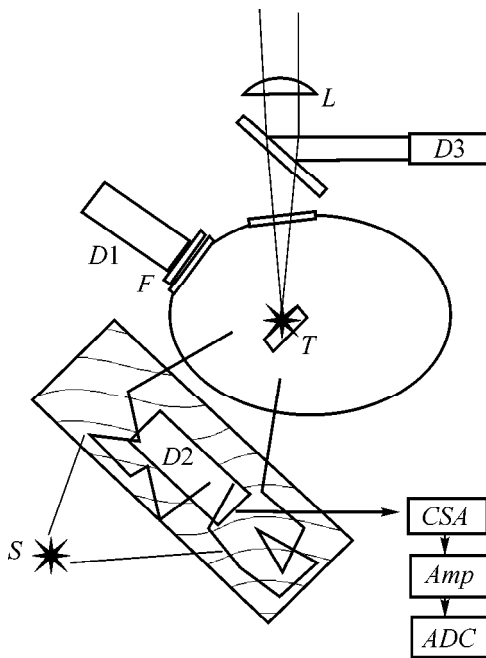


Fig. 1. Scheme of the experiment.

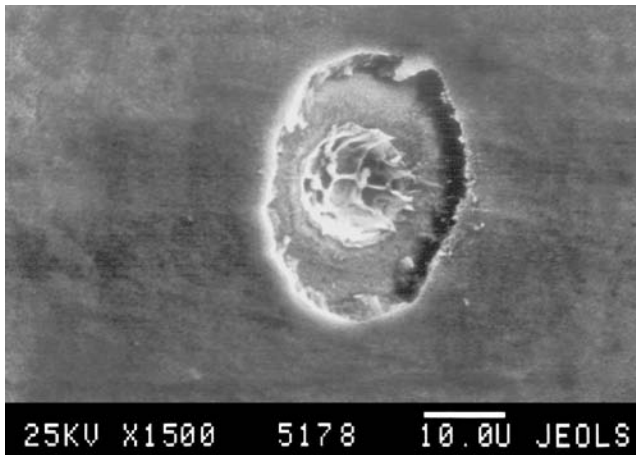


Fig. 2. Electron diffraction pattern of a crater on a Ti surface (the normal to the sample surface forms an angle of  $30^\circ$  with the beam). The white horizontal bar at the bottom of the image corresponds to  $10\ \mu\text{m}$ .

This idea underlies the experimental work presented below. An important point is that the neutron pulse duration  $\tau$  in this regime is limited by a time shorter than  $10\ \text{ps}$  because of the fast decrease in plasma density upon its free expansion.

**3. Experiments** (Fig. 1) were conducted using emission of a femtosecond dye laser system [10] with a pulse duration of  $200\ \text{fs}$  and energy  $W$  (monitored by detector  $D3$ ) of up to  $1\ \text{mJ}$ . Pulse intensity contrast was no worse than  $10^5$ . Focusing this radiation by an aberration-free lens  $L$  with a focal length of  $6\ \text{cm}$  provided

an intensity of  $10\text{--}50\ \text{PW}/\text{cm}^2$  on a target. The accuracy of tuning the focusing lens was monitored by measuring X-ray output at energies higher than  $9\ \text{keV}$  by detector  $D1$  [scintillation counter  $\text{NaI}(\text{Te})$ ] equipped with filter  $F$  ( $200\ \mu\text{m}$  of Be and  $100\ \mu\text{m}$  of Al). Targets  $T$  were placed in a small chamber of size  $5 \times 5 \times 5\ \text{cm}$  with a residual gas pressure no higher than  $10^{-2}\ \text{torr}$ . The small size of the vacuum interaction chamber and the positioning of the neutron detector at a distance of  $12\ \text{cm}$  from the plasma focus allowed the experiments to be conducted with low laser energies of  $\sim 1\ \text{mJ}$ .

The experiments were carried out with several deuterated targets (Ti, Si, and Pd), but the best results were obtained for titanium. The sample was a  $300\text{-}\mu\text{m}$ -thick molybdenum platelet coated with a titanium layer with surface density  $2.2\ \text{mg}/\text{cm}^2$ . Titanium was saturated with deuterium to an average atomic concentration of  $1.65$ . The data on hydrogen Rutherford backscattering suggested that the deuterium concentration at a depth of  $0.3\ \mu\text{m}$  was equal to  $0.6$  of the atomic concentration.

We developed a two-pulse method of obtaining laser-modified targets. The first pulse forms a crater with a highly developed surface with a diameter of the order of  $5\ \mu\text{m}$  and a depth of about  $1\ \mu\text{m}$  (Fig. 2). The second pulse (several seconds after) produces plasma with an anomalously high ion temperature at the crater surface. The estimate, by the method suggested in our work [11], of the temperature of plasma electrons suggested that the electron temperature ( $T \sim 6\ \text{keV}$ ) in plasma produced in the crater is comparable to the temperature obtained upon illumination of a flat target ( $T \sim 4\ \text{keV}$ ). Note that the second pulse also modifies the target crater, allowing its use for further irradiation. As a result, the crater depth increases. The maximum number of possible shots without displacing the target was estimated from a decrease in the signal of detector  $D1$  and proved to be  $5\text{--}6$  shots in the same crater.

Individual neutrons with energies  $2.3\text{--}2.6\ \text{MeV}$  were recorded by a spectrometric neutron detector  $D2$  consisting of a counter filled with a mixture of  $\text{He}^3$  and Ar and operating in the ionization chamber mode. The counter was placed in a polyethylene moderator made in the form of a rectangular parallelepiped of dimensions  $10 \times 10 \times 20\ \text{cm}$ . The signal from detector  $D2$  was fed through a low-noise charge-sensitive amplifier (CSA) and a linear amplifier (Amp) into a fast-response analog-to-digital converter (ADC) with a buffer memory of  $32\ \text{KB}$ . Triggering of the ADC was rigidly locked with the laser pulse. A typical signal recorded for an individual neutron is shown in the inset in Fig. 3.

The measuring circuit was calibrated and adjusted using test source  $S$  ejecting  $11\ 200$  neutrons with energy  $3.2\ \text{MeV}$  per second. When calibrating detector  $D2$ , the source  $S$  was placed on the opposite side of the detector symmetrically about the laser plasma. Figure 3 shows the pulse amplitude histogram for source  $S$ , together with the noise histogram. The individual

counts with large amplitudes in the latter are due to the background neutrons (1 neutron in 10–15 s).

A threshold of 40 mV was chosen for the experimental detection of neutrons from laser plasma (see vertical line in Fig. 3). Using the known neutron yield of source  $S$ , the detection efficiency was estimated at 0.04% for the neutrons with energy 2–3 MeV and the detection threshold chosen.

It should be noted that neutron detection in a circuit with digital oscilloscope allowed one to correct for a slow drift of the CSA “null” and select the neutron signal, according to its amplitude and shape, from noise and other interference. A time interval of 5 ms during which neutrons were recorded after the ignition of laser plasma was dictated by the lifetime of thermal neutrons in the moderator. Measurements of the proper neutron background under our experimental conditions showed that, for the sampled value of 5 ms, the probability of detecting a background neutron was equal to  $5 \times 10^{-4}$ .

Several sets of experiments with the analyses from 500 to 2000 laser shots were performed. On the average,  $5 \pm 2$  neutrons with amplitudes higher than 40 mV were recorded in 2000 shots (see abscissa axis in Fig. 3). Based on the known probability of detecting background neutron in a single shot, the probability that one of the detected neutrons will be background is close to unity, while the probability for all the detected neutrons to be background is 0.04. Therefore, with allowance made for the quantum efficiency of the neutron detector, the average number of neutrons in a single shot in plasma bulk was  $5 \pm 2$ .

Let us compare the obtained values with estimate (1). According to the time-of-flight measurements [12], the deuteron energy is equal to 1–3 keV. The corresponding reaction rate is  $\langle \sigma v \rangle_{DD} \approx 10^{-20} - 10^{-22} \text{ cm}^3 \text{ s}^{-1}$  [8]. For the total number of neutrons in the plasma bulk, one obtains  $N_n \approx 0.2 - 20$  ( $n_D \approx 3 \times 10^{22} \text{ cm}^{-3}$ ,  $\tau \approx 5 \text{ ps}$ , and  $V \approx 10^{-12} \text{ cm}^3$ ), in reasonable agreement with the experimentally measured value.

A comparative analysis of our results and the results obtained in [6], where femtosecond laser emission of the same intensity was brought into interaction with a deuterium cluster jet, shows that the neutron number recalculated to a unit absorbed energy is equal to  $\sim 10^5$  neutron/J in both cases. At the same time, the efficiency of neutron generation in our experiments [ $\eta \equiv N_n / W n_D V \approx 10^{-6}$  neutron/(J atom)] is 1000 times higher than in the case of cluster targets. No doubt this is caused by the near-solid concentration of deuterium atoms in our targets.

**4.** The total number of neutrons per single laser shot may be increased in our targets by increasing the pulse energy and, as a result, increasing the plasma volume. However, the elevation of the plasma ion temperature (by improving surface organization for the nanostructured metallic targets) or the use of reactions with large cross sections seems to be a more efficient way of

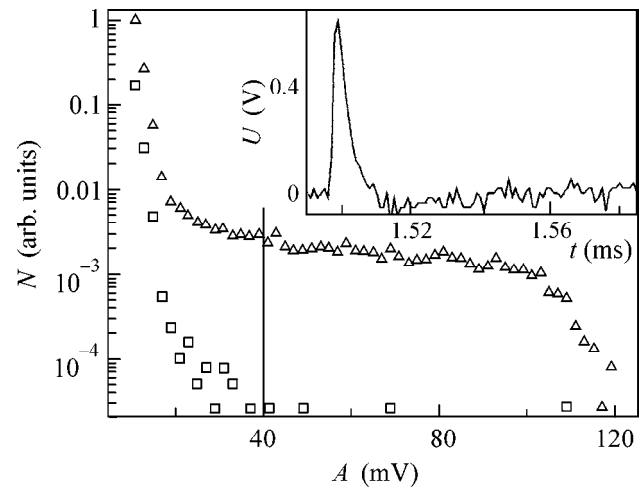


**Fig. 3.** Histogram of the number  $N$  of pulses with a given amplitude  $A$  at the output of the detecting system. Squares: without the external neutron source. Triangles: with the external source.

enhancing the reaction rate. For example, the cross section for the  ${}^3\text{H}(d, n){}^4\text{He}$  reaction is larger than that for the  ${}^2\text{H}(d, n){}^3\text{He}$  reaction by at least two orders of magnitude [8]. Our approach may also prove to be efficient in the generation of picosecond pulses of high-energy neutrons, protons, and alpha particles.

In summary, the production of a dense high-temperature femtosecond laser plasma in nanostructured targets allows the realization of new opportunities associated with the generation of ultrashort pulses of energetic particles such as neutrons, protons, etc. This, in turn, is of considerable interest for nuclear physics, materials science, and other studies with pico- and subpicosecond time resolution.

We are grateful to V.S. Kulikauskas for measuring deuterium concentration profiles in near-surface layers of the samples and to A.A. Serov for electron diffraction studies of the craters. This work was supported by the Russian Foundation for Basic Research (project no. 99-02-18343a) and the State Scientific and Technical Programs “Fundamental Metrology” and “Russian Universities.”

## REFERENCES

1. A. V. Andreev, R. V. Volkov, V. M. Gordienko, *et al.*, *Pis'ma Zh. Éksp. Teor. Fiz.* **69**, 343 (1999) [*JETP Lett.* **69**, 371 (1999)].
2. K. W. D. Ledingham, I. Spencer, T. McCanny, *et al.*, *Phys. Rev. Lett.* **84**, 899 (2000).
3. T. E. Cowan, A. W. Hunt, T. W. Phillips, *et al.*, *Phys. Rev. Lett.* **84**, 903 (2000).
4. G. Pretzler, A. Saemann, A. Pukhov, *et al.*, *Phys. Rev. E* **58**, 1165 (1998).
5. P. A. Norreys, A. P. Fews, F. N. Begg, *et al.*, *Plasma Phys. Controlled Fusion* **40**, 175 (1998).

6. J. Zweiback, R. A. Smith, T. E. Cowan, *et al.*, Phys. Rev. Lett. **84**, 2634 (2000).
7. N. E. Basov, S. D. Zakharov, P. G. Kryukov, *et al.*, Pis'ma Zh. Éksp. Teor. Fiz. **8**, 26 (1968) [JETP Lett. **8**, 14 (1968)].
8. K. Brakner and S. Jorna, *Laser Driven Fusion* (KMS Fusion, 1973; Atomizdat, Moscow, 1977).
9. V. M. Gordienko and A. B. Savel'ev, Usp. Fiz. Nauk **169**, 78 (1999).
10. R. V. Volkov, V. M. Gordienko, M. S. Dzhidzhoev, *et al.*, Kvantovaya Élektron. (Moscow) **24**, 1114 (1997).
11. R. V. Volkov, V. M. Gordienko, P. M. Mikheev, and A. B. Savel'ev, Kvantovaya Élektron. (Moscow) **27** (9), (2000) (in press).
12. V. M. Gordienko, O. V. Chutko, D. M. Golishnikov, *et al.*, in *Abstracts of 3rd International Symposium on Modern Problems of Laser Physics, Akademgorodok, Novosibirsk, July 2–7, 2000*, p. 62.

*Translated by V. Sakun*

# Multiple-Pomeron Splitting in QCD—A Novel Antishadowing Effect in Coherent Dijet Production on Nuclei<sup>1</sup>

N. N. Nikolaev<sup>\*,\*\*</sup>, W. Schäfer<sup>\*\*</sup>, and G. Schwiete<sup>\*\*</sup>

<sup>\*</sup> Landau Institute for Theoretical Physics, Russian Academy of Sciences, ul. Kosygina 2, Moscow, 117940 Russia

<sup>\*\*</sup> Institut für Kernphysik (Th), FZ Jülich, D-52425 Jülich, Germany

Received September 18, 2000

We discuss the salient features of the Pomeron splitting mechanism for coherent diffraction of pions into hard dijets on nuclei. Our findings include antishadowing multiple-Pomeron splitting expansion for diffractive amplitudes, exact cancellation of nuclear attenuation, and broadening/antishadowing effects to leading twist and parameter-free perturbative calculation of nuclear-rescattering-driven higher twist correction. We comment on the pQCD interpretation of the E791 results on diffractive dijets. © 2000 MAIK “Nauka/Interperiodica”.

PACS numbers: 11.80.La; 13.85.-t; 13.87.-a; 25.80.Hp

At the QCD parton level, diffraction dissociation of photons and hadrons is modeled by excitation of  $q\bar{q}$ ,  $q\bar{q}g$ , ... Fock states, which are lifted on their mass shell through the  $t$ -channel exchange of a QCD Pomeron with the target hadron. The color singlet two-gluon structure of the Pomeron gives rise to two distinct forward  $q\bar{q}$  dijet production subprocesses: the first one, in Fig. 1a, is a counterpart of the classical Landau, Pomeranchuk, Feinberg, and Glauber [1–3] mechanism of diffraction dissociation of deuterons into the proton–neutron continuum and can be dubbed the splitting of the beam particle into the dijet, because the transverse momentum  $\mathbf{k}$  of jets comes from the intrinsic transverse momentum of quarks and antiquarks in the beam particle. Specific to QCD is the mechanism in Fig. 1b, where jets receive a transverse momentum from gluons in the Pomeron. In an extension of their earlier work [4], Nikolaev and Zakharov showed in 1994 [5] that the second mechanism dominates at a sufficiently large  $\mathbf{k}$  and in this regime, diffractive amplitudes are proportional to the differential (unintegrated) gluon structure function  $\mathcal{F}(x, \mathbf{k}^2) = \partial G(x, \mathbf{k}^2)/\partial \log \mathbf{k}^2$ . Correspondingly, this mechanism has been dubbed splitting of the Pomeron into dijets. In diffractive DIS, the Pomeron splitting dominates at  $k \gg Q$ , whereas the somewhat modified Landau *et al.* mechanism dominates at  $k \lesssim Q$ .

Motivated by the recent data from the E791 Fermilab experiment [6], we discuss in this communication the peculiarities of the Pomeron splitting contribution to diffractive excitation of pions into dijets on free nucleon and nuclear targets. First, because of the non-

pointlike nature of the  $\pi \rightarrow q\bar{q}$  vertex, it is precisely the Pomeron splitting mechanism which dominates at large  $\mathbf{k}$ . Second, in the Pomeron splitting regime, the diffraction amplitudes are found to be proportional to the much-discussed pion distribution amplitude [7]. Third, we show that multiple-Pomeron splitting emerges as the sole mechanism of nuclear broadening of the jet momentum distribution. Fourth, we derive an antishadowing property of a multiple-Pomeron splitting expansion of nuclear diffraction amplitudes. Fifth, we establish model independence of the higher twist effect from nuclear rescatterings.

We first turn to the description of the nucleon amplitude  $\pi p \rightarrow (q\bar{q})p$ , which is a building block of the nuclear multiple scattering series. In a slight adaptation of the results of [4, 5], one should replace the pointlike  $\gamma^* q\bar{q}$  vertex  $eA_\mu \bar{\Psi} \gamma_\mu \Psi$  by the nonpointlike  $\pi q\bar{q}$  vertex  $i\Gamma(M^2) \bar{\Psi} \gamma_5 \Psi$ . Here,  $M^2 = (\mathbf{k}^2 + m_f^2)/z(1-z)$  is the invariant mass squared of the dijet system and the pion momentum is shared by the jets in the partitioning  $z, 1-z$ . The explicit form of the spinor vertex reads

$$\begin{aligned} & \bar{\Psi}_\lambda(\mathbf{k}) \gamma_5 \Psi_{\bar{\lambda}}(-\mathbf{k}) \\ &= \frac{\lambda}{\sqrt{z(1-z)}} [m_f \delta_{\lambda-\bar{\lambda}} - \sqrt{2} \mathbf{k} \cdot \mathbf{e}_{-\lambda} \delta_{\lambda\bar{\lambda}}], \end{aligned} \quad (1)$$

where  $m_f$  is the quark mass,  $\lambda$  and  $\bar{\lambda}$  are the quark and antiquark helicities, and  $\mathbf{e}_\lambda = -(\lambda \mathbf{e}_x + i \mathbf{e}_y)/\sqrt{2}$ . The two helicity amplitudes  $\Phi_0(z, \mathbf{k}, \Delta)$  for  $\lambda + \bar{\lambda} = 0$  and

<sup>1</sup> This article was submitted by the authors in English.

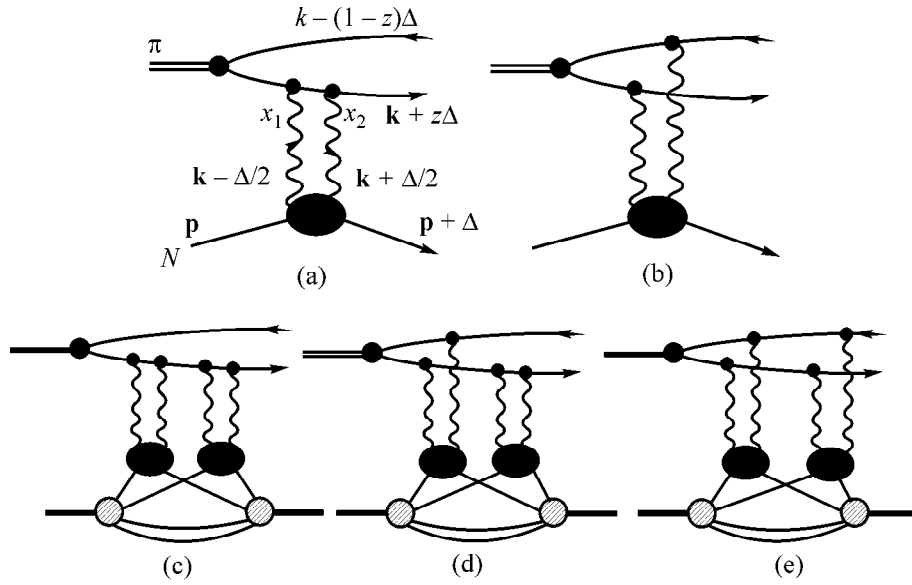


**Fig. 1.** Sample Feynman diagrams for diffractive dijet excitation in  $\pi N$  collisions (diagrams 1a, 1b), and typical rescattering corrections to the nuclear coherent amplitude (diagrams 1c, 1d, 1e).

$\Phi_1(z, \mathbf{k}, \Delta)$  for  $\lambda + \bar{\lambda} = \pm 1$ , can be cast in the form (we concentrate on the forward limit  $\Delta = 0$ )

$$\Phi_0(z, \mathbf{k}) = \alpha_s(\mathbf{k}^2) \sigma_0 \left[ \int d^2 \boldsymbol{\kappa} m_f \psi_\pi(z, \mathbf{k}) f^{(1)}(\boldsymbol{\kappa}) - \int d^2 \boldsymbol{\kappa} m_f \psi_\pi(z, \boldsymbol{\kappa}) f^{(1)}(\mathbf{k} - \boldsymbol{\kappa}) \right], \quad (2)$$

and  $\Phi_1$  is obtained from the substitution  $m_f \psi(z, \mathbf{k}) \rightarrow \mathbf{k} \psi(z, \mathbf{k})$ . We introduced

$$\sigma_0 = \frac{4\pi}{3} \int d^2 \mathbf{k} \frac{\mathcal{F}_f\left(\frac{1}{2}x_{\text{IP}}, \mathbf{k}^2\right)}{\mathbf{k}^4}, \quad (3)$$

$$f^{(1)}(\mathbf{k}) = \frac{4\pi}{3\sigma_0} \frac{\mathcal{F}_f\left(\frac{1}{2}x_{\text{IP}}, \mathbf{k}^2\right)}{\mathbf{k}^4},$$

$x_{\text{IP}} = M^2/W^2$  and  $W$  is the total  $\pi p$  CM energy; below, the argument  $x = x_{\text{IP}}/2$  of the unintegrated gluon structure function accounts for the skewedness of the  $t$ -channel gluons [8]. The distribution  $f^{(1)}(\mathbf{k})$  is normalized to unity,  $\int d^2 \mathbf{k} f^{(1)}(\mathbf{k}) = 1$ , and  $\sigma_0$  is the soft gluon exchange-dominated nonperturbative parameter. The radial wave function of the  $q\bar{q}$  Fock state of the pion is related to the  $\pi q\bar{q}$  vertex function as

$$\psi_\pi(z, \mathbf{k}) = \frac{N_c}{4\pi^3} \frac{\Gamma_\pi(M^2)}{z(1-z)(M^2 - m_\pi^2)} \quad (4)$$

and is normalized to the  $\pi \rightarrow \mu\nu$  decay constant  $F_\pi = 131$  MeV through

$$F_\pi = \int d^2 \mathbf{k} dz m_f \psi_\pi(z, \mathbf{k}) = F_\pi \int_0^1 dz \phi_\pi(z), \quad (5)$$

where  $\phi_\pi(z)$  is the pion distribution amplitude [7]. Finally, our normalization of helicity amplitudes is such that the differential cross section for forward dijet production equals

$$\left. \frac{d\sigma_D}{dz d\mathbf{k}^2 d\Delta^2} \right|_{\Delta=0} = \frac{\pi^3}{24} \{ |\Phi_0|^2 + |\Phi_1|^2 \}. \quad (6)$$

We turn to the discussion of the asymptotics for large jet momenta  $\mathbf{k}$ . The first term in Eq. (2) comes from the Landau *et al.* pion splitting mechanism in Fig. 1a, whereas the second one is the contribution from the Pomeron splitting in Fig. 1b. Because it is a convolution  $\psi_\pi \otimes f^{(1)}$ , it is necessarily a broader function than  $\psi_\pi(z, \mathbf{k})$  and thus will take over only if  $\mathbf{k}$  is large enough. For the quantitative estimate, we remind the reader that, for  $x \sim 10^{-2}$  relevant to the kinematics of E791, the large- $\mathbf{k}$  behavior of  $f^{(1)}(\mathbf{k})$  is well described by the inverse power law  $f^{(1)}(\mathbf{k}) \propto k^{-2\delta}$  with an exponent  $\delta \sim 2.15$  [9]. Clearly,  $f^{(1)}(\mathbf{k})$  decreases much slower than  $\psi(z, \mathbf{k})$  and, hence, the asymptotics of the convolution integral is controlled by the asymptotics of  $f^{(1)}(\mathbf{k})$ :

$$\int d^2 \boldsymbol{\kappa} m_f \psi_\pi(z, \boldsymbol{\kappa}) f^{(1)}(\mathbf{k} - \boldsymbol{\kappa}) \approx f^{(1)}(\mathbf{k}) \int d^2 \boldsymbol{\kappa} m_f \psi_\pi(z, \boldsymbol{\kappa}) = f^{(1)}(\mathbf{k}) \phi_\pi(z) F_\pi, \quad (7)$$

which shows that, in this regime, the dijet momentum comes entirely from the momentum of gluons in the Pomeron. Furthermore, in the same regime, diffraction into dijets probes the pion distribution amplitude  $\phi_\pi(z)$ . We note parenthetically that the explicit proportionality to the unintegrated gluon structure function  $\mathcal{F}(x, \mathbf{k}^2)$  is in marked contrast to the erroneous claims in [10], where the diffractive amplitude was alleged to be proportional to the *integrated* gluon structure function  $G(x_{\text{IP}}, \mathbf{k}^2)$ .

The generalization to the nuclear target is most conveniently made in the  $q\bar{q}$  color dipole representation [11]; for brevity, we focus on  $\Phi_0$ , which takes the form

$$\Phi_0(z, \mathbf{k}) = \int d^2\mathbf{r} e^{-i\mathbf{k}\mathbf{r}} \sigma(x, \mathbf{r}) m_f \Psi_\pi(z, \mathbf{r}), \quad (8)$$

Here, the color dipole cross section  $\sigma(x, \mathbf{r})$  for the interaction of a color dipole of transverse size  $\mathbf{r}$  and the color dipole distribution amplitude  $\Psi_\pi(z, \mathbf{r})$  in the pion in the impact parameter plane are defined through

$$\begin{aligned} \sigma(x, \mathbf{r}) &= \alpha_s(\mathbf{k}^2) \sigma_0 \int d^2\mathbf{\kappa} f^{(1)}(\mathbf{\kappa}) [1 - e^{i\mathbf{\kappa}\mathbf{r}}], \\ \Psi_\pi(z, \mathbf{r}) &= \int \frac{d^2\mathbf{k}}{(2\pi)^2} \Psi_\pi(z, \mathbf{k}) e^{i\mathbf{k}\mathbf{r}}. \end{aligned} \quad (9)$$

The Glauber–Gribov representation [12, 13] of the nuclear amplitude is readily obtained [11] by substituting in Eq. (8)

$$\begin{aligned} \sigma(x, \mathbf{r}) &\longrightarrow \sigma_A(x, \mathbf{r}) \\ &= 2 \int d^2\mathbf{b} \left( 1 - \exp\left(-\frac{1}{2} \sigma(x, \mathbf{r}) T_A(\mathbf{b})\right) \right), \end{aligned}$$

where  $\mathbf{b}$  is the pion–nucleus impact parameter,  $T_A(\mathbf{b})$  is the nuclear optical thickness, and  $\int d^2\mathbf{b} T_A(\mathbf{b}) = A$ . Typical nuclear double scattering diagrams in Figs. 1c–1e can conveniently be classified as nuclear shadowing of the pion splitting (Fig. 1c), nuclear shadowing of single Pomeron splitting (Fig. 1d), and double Pomeron splitting (Fig. 1e) contributions. The  $j$  Pomeron splitting is due to the diagrams, in which  $j$  of the Pomerons exchanged between the color dipole and the nucleus couple with one gluon to the quark and with one gluon to the antiquark and involve the  $j$ -fold convolutions of the unintegrated gluon distribution

$$\begin{aligned} &f^{(j)}(\mathbf{k}) \\ &= \int d^2\mathbf{\kappa}_1 \dots d^2\mathbf{\kappa}_j f^{(1)}(\mathbf{\kappa}_1) \dots f^{(1)}(\mathbf{\kappa}_j) \delta\left(\mathbf{k} - \sum_{i=1}^j \mathbf{\kappa}_i\right). \end{aligned} \quad (10)$$

After some algebra, we obtain the central result of this paper—the multiple-Pomeron splitting expansion for the nuclear diffractive amplitude:

$$\Phi_0^{(A)}(z, \mathbf{k}, \Delta) = 2m_f \int d^2\mathbf{b} e^{-i\mathbf{b}\Delta}$$

$$\begin{aligned} &\times \left\{ \Psi_\pi(z, \mathbf{k}) \left[ 1 - \exp\left(-\frac{\sigma_{\text{eff}}(\mathbf{k}^2)}{2} T_A(\mathbf{b})\right) \right] \right. \\ &\quad \left. - \sum_{j \geq 1} \int d^2\mathbf{\kappa} \Psi_\pi(z, \mathbf{\kappa}) f^{(j)}(\mathbf{k} - \mathbf{\kappa}) \right. \\ &\quad \left. \times \frac{1}{j!} \left[ \frac{\sigma_{\text{eff}}(\mathbf{k}^2) T_A(\mathbf{b})}{2} \right]^j \exp\left[-\frac{\sigma_{\text{eff}}(\mathbf{k}^2)}{2} T_A(\mathbf{b})\right] \right\}. \end{aligned} \quad (11)$$

Here, we reinstated a dependence on the momentum transfer  $\Delta$ , which in the final result can be related to the nuclear charge form factor  $G_{em}(\Delta^2)$ . Those Pomeron exchanges in which both gluons couple to the same constituent in the color dipole give rise to nuclear attenuation with an effective cross section  $\sigma_{\text{eff}} = \alpha_s(\mathbf{k}^2) \sigma_0$ , the appearance of the strong coupling at the hard scale  $\mathbf{k}^2$  being a reminder of color transparency. Remarkably, all the multiple Pomeron splittings enter with the same sign and are an antishadowing, i.e., enhancement, contribution to the impulse approximation, i.e., single-pomeron splitting, term  $\propto f^{(1)}(\mathbf{k})$ . Again, one may obtain  $\Phi_1^{(A)}$  by substituting  $m_f \Psi_\pi(z, \mathbf{k}) \longrightarrow \mathbf{k} \Psi_\pi(z, \mathbf{k})$ . Obviously, similar formulas apply to dijet photoproduction, as well as to deep inelastic diffractive scattering. As we argued above, for the pion beam, the multiple Pomeron splitting terms will rather quickly take over.

We estimate the large- $\mathbf{k}$  behavior of  $f^{(j)}(\mathbf{k})$  and of their convolution with the pion wave function by making use of the small- $\mathbf{\kappa}$  expansion of  $f^{(1)}(\mathbf{k} - \mathbf{\kappa})$ . To the next-to-leading twist, one can readily derive that the power law asymptotic form  $f^{(1)}(\mathbf{k}) \propto k^{-2\delta}$  entails the large- $\mathbf{k}$  behavior of  $f^{(j)} \otimes \Psi_\pi$  given by

$$\begin{aligned} &\int d^2\mathbf{\kappa} m_f \Psi_\pi(z, \mathbf{\kappa}) f^{(j)}(\mathbf{k} - \mathbf{\kappa}) = F_\pi \phi_\pi(z) j f^{(1)}(\mathbf{k}) \\ &\quad \times \left[ 1 + \frac{\delta^2}{\mathbf{k}^2} \left( \langle \kappa_\pi^2(z) \rangle + \frac{4\pi^2}{3\sigma_0} (j-1) G(x, \mathbf{k}^2) \right) \right]. \end{aligned} \quad (12)$$

Here, the proportionality to  $j$  of the leading twist reflects the broadening properties of the multiple convolution. Note that, due to the factor  $j-1$ , this broadening is still stronger for nuclear higher twist. The higher twist induced by intrinsic momentum of constituents in the pion is controlled by the nonperturbative parameter  $\langle \kappa_\pi^2(z) \rangle = m_f \int d^2\mathbf{\kappa} \kappa^2 \Psi_\pi(z, \mathbf{\kappa}) / \phi_\pi(z) F_\pi$ . Realistic soft wave functions of the pion give  $\langle \kappa_\pi^2(z) \rangle \sim 0.15\text{--}0.2 \text{ GeV}^2$  [14].

Making use of the explicit  $j$  dependence of the large- $\mathbf{k}$  asymptotic expression (12) in the multiple-Pomeron splitting expansion (11), one readily finds the most intriguing result—an *exact cancellation* of the

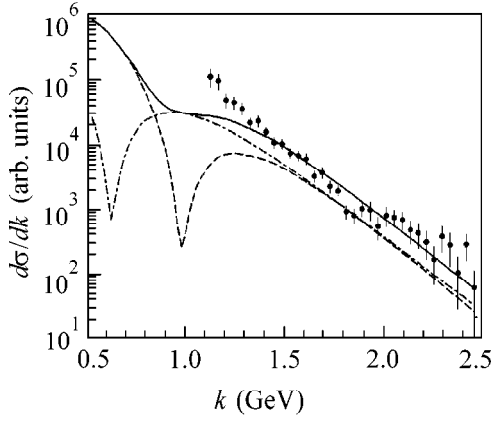


**Fig. 2.** The E791 data [6] for the differential diffractive dijet cross sections  $d\sigma/dk$  for the  $^{196}\text{Pt}$  target with the theoretical calculations. The data are not normalized. The dash-dotted line shows the contribution of the helicity amplitude  $\Phi_0^{(A)}$ , and the dashed line is the contribution from  $\Phi_1^{(A)}$ . The solid line is the total result.

broadening and antishadowing and the soft shadowing effects to both the leading and next-to-leading order,

$$\Phi_0^{(A)}(z, \mathbf{k}, \Delta = 0) \approx -A \frac{4\pi F_\pi \phi_\pi(z) \alpha_s(\mathbf{k}^2) \mathcal{F}(x, \mathbf{k}^2)}{3\mathbf{k}^4} \times \left\{ 1 + \frac{\delta^2}{\mathbf{k}^2} \left[ \langle \kappa_\pi^2(z) \rangle + \frac{\pi C_A A \alpha_s(\mathbf{k}^2) G\left(\frac{1}{2}x_{\text{IP}}, \mathbf{k}^2\right)}{2\langle R_{ch}^2 \rangle} \right] \right\} \quad (13)$$

Namely, in contrast to the nonperturbative higher twist  $\propto \langle \kappa_\pi^2(z) \rangle$ , the arguably dominant, nuclear-rescattering, higher twist is parameter-free and perturbatively calculable. It is controlled by the scaling violations in the gluon structure function  $G(x, Q^2)$  and rises for heavy nuclei  $\propto A^{1/3}$ . Although for both leading and next-to-leading twists any dependence on the soft rescattering parameter  $\sigma_{\text{eff}}(\mathbf{k}^2)$  disappears, this does not imply that higher order rescatterings are unimportant: the rescatterings up to  $j = 9-10$  do contribute, and  $\langle j \rangle = 4.2$  for the  $^{192}\text{Pt}$  target and  $\langle j \rangle = 2.05$  for the  $^{12}\text{C}$  target. In contrast to  $\Phi_0(z, \mathbf{k}, \Delta)$ , the large- $\mathbf{k}$  asymptotic form of  $\Phi_1(z, \mathbf{k})$  is that of a pure higher twist:

$$\Phi_1^{(A)}(z, \mathbf{k}, \Delta = 0) \approx -A \times \frac{4\pi F_\pi \phi_\pi(z) \alpha_s(\mathbf{k}^2) \mathcal{F}(x, \mathbf{k}^2) \delta \langle \kappa_\pi^2(z) \rangle}{3m_f \mathbf{k}^4 \mathbf{k}^2}. \quad (14)$$

For large  $\mathbf{k}$ , where the terms  $\propto \Psi_\pi(z, \mathbf{k})$  die out, using Eq. (12), we obtain, upon integration over the transverse momentum transfer  $\Delta$ , the following simple form

for the large- $\mathbf{k}$  asymptotic behavior of the diffractive dijet cross section:

$$\frac{d\sigma_D}{dz d\mathbf{k}^2} = \frac{2\pi^5}{27} F_\pi^2 \phi_\pi^2(z) G_{em}^2(x_{\text{IP}}^2 m_N^2) \alpha_s^2(\mathbf{k}^2) \times \left[ \frac{\mathcal{F}(x, \mathbf{k}^2)}{\mathbf{k}^4} \right]^2 \frac{3A^2}{\langle R_{ch}^2 \rangle} \left\{ 1 + \frac{\delta^2}{\mathbf{k}^2} \left[ 2\langle \kappa_\pi^2(z) \rangle + \frac{\langle \kappa_\pi^2(z) \rangle^2}{m_f^2} \right] \right. \quad (15)$$

$$\left. + \frac{2\pi C_A A \alpha_s(\mathbf{k}^2)}{3\langle R_{ch}^2 \rangle} G(x, \mathbf{k}^2) \right\}.$$

Here, the parameter  $C_A \approx 1$  depends slightly on the shape of the nuclear matter distribution,  $R_{ch}$  is the nuclear charge radius, and the factor  $G_{em}^2(x_{\text{IP}}^2 m_N^2)$  accounts for the finite longitudinal momentum transfer  $x_{\text{IP}} m_N$  to the target nucleus. The second term in curly braces in Eq. (15) is the higher twist contribution  $\propto \Phi_1^2$ . Note that the behavior  $\propto k^{-8}$  expected from naive dimensional counting receives potentially large corrections from the scaling violations in  $\mathcal{F}(x, \mathbf{k}^2)$ . Remarkably, the leading twist term does not contain any free parameters and thus is a perturbatively calculable quantity. The  $z$  dependence of the nonperturbative parameter  $\langle \kappa_\pi^2(z) \rangle$  is sufficiently weak and does not preclude the determination of the pion distribution amplitude from the  $z$ -distribution of dijets.

The detailed numerical analysis for the kinematics of the E791 experiment will be reported elsewhere. In Fig. 2, we only show the numerical result of the  $\mathbf{k}$  dependence of the dijet cross section with the (unnormalized) preliminary data from E791. We note in passing that the region of jet momenta  $k \lesssim 1.5$  GeV is contaminated by diffractive excitation of heavy mesons  $a_1$ ,  $\pi'$ , etc., and in this region the use of plane wave parton model formulas is not warranted. Our calculations for smaller  $k$  only serve to give an idea of how the pion splitting dominates at small  $k$  and how the pomeron splitting mechanism takes over beyond the dip in  $\Phi_0^2$  and  $\Phi_1^2$ . In the pomeron splitting dominance region of  $k > 1.5$  GeV, we find good agreement with experiment. We wish to warn the reader, however, that for the kinematics of E791 the dijet cross section receives huge contributions from higher twists, which is exemplified by the large contribution from higher twist amplitude (14), i.e., the second term in the curly braces in the expansion (15).

We are grateful to Danny Ashery for correspondence on the E791 data and to B.G. Zakharov for discussions in the early stages of this study. This work was supported in part by the INTAS, grant no. 97-30494.

## REFERENCES

1. L. D. Landau and I. Ya. Pomeranchuk, Zh. Éksp. Teor. Fiz. **24**, 505 (1953).
2. I. Ya. Pomeranchuk and E. L. Feinberg, Dokl. Akad. Nauk SSSR **93**, 439 (1953); E. L. Feinberg, Zh. Éksp. Teor. Fiz. **28**, 242 (1955) [Sov. Phys. JETP **1**, 177 (1955)]; E. L. Feinberg and I. Ya. Pomeranchuk, Nuovo Cimento Suppl. **4**, 652 (1956); A. I. Akhiezer and A. G. Sitenko, Zh. Éksp. Teor. Fiz. **32**, 794 (1957) [Sov. Phys. JETP **5**, 652 (1957)]; Zh. Éksp. Teor. Fiz. **33**, 1040 (1957) [Sov. Phys. JETP **6**, 799 (1957)].
3. R. J. Glauber, Phys. Rev. **99**, 1515 (1955).
4. N. N. Nikolaev and B. G. Zakharov, Z. Phys. C **53**, 331 (1992).
5. N. N. Nikolaev and B. G. Zakharov, Phys. Lett. B **332**, 177 (1994).
6. D. Ashery, Invited talk at X International Light-Cone Meeting, Heidelberg, June 2000; hep-ex/0008036.
7. V. L. Chernyak and A. R. Zhitnitsky, Phys. Rep. **112**, 173 (1984); P. Kroll,  $\pi N$  Newslett. **15**, 205 (1999); R. Jakob and P. Kroll, Phys. Lett. B **315**, 463 (1993); Erratum: **319**, 545 (1993); G. P. Lepage and S. J. Brodsky, Phys. Rev. D **22**, 2157 (1980); S. J. Brodsky, H.-C. Pauli, and S. S. Pinsky, Phys. Rep. **301**, 299 (1998).
8. A. V. Radyushkin, Phys. Lett. B **385**, 333 (1996); K. Golec-Biernat, J. Kwiecinski, and A. D. Martin, Phys. Rev. D **58**, 094001 (1998).
9. I. P. Ivanov and N. N. Nikolaev, hep-ph/0004206.
10. L. L. Frankfurt, G. A. Miller, and M. I. Strikman, Phys. Lett. B **304**, 1 (1993).
11. N. N. Nikolaev and B. G. Zakharov, Z. Phys. C **49**, 607 (1991).
12. R. J. Glauber, in *Lectures in Theoretical Physics*, Ed. by W. Brittain and L. G. Dunham (Interscience, New York, 1959), Vol. 1; R. J. Glauber and G. Matthiae, Nucl. Phys. B **21**, 135 (1970).
13. V. N. Gribov, Zh. Éksp. Teor. Fiz. **56**, 892 (1969) [Sov. Phys. JETP **29**, 483 (1969)].
14. W. Jaus, Phys. Rev. D **44**, 2851 (1991); G. Schwiete, Diploma Thesis (Univ. of Bonn).

## On the Possibility of Observation of $a_0$ - $f_0$ Mixing in the $pn \rightarrow da_0$ Reaction

A. E. Kudryavtsev and V. E. Tarasov

*Institute of Theoretical and Experimental Physics, ul. Bol'shaya Cheremushkinskaya 25, Moscow, 117259 Russia*  
*e-mail: kudryavtsev@vxitep.itep.ru and tarasov@vxitep.itep.ru*

Received September 19, 2000

It is shown that, if isospin is not conserved in  $a_0^0$ - and  $f_0$ -meson mixing, forward-backward asymmetry arises in the  $pn \rightarrow da_0^0$  reaction. This effect increases near the reaction threshold. The asymmetry is estimated within the framework of a model in which the  $a_0^0$ - $f_0$  mixing is due to the virtual  $\pi^0 \longleftrightarrow \eta$  transition and the difference in masses of the charged and neutral kaons in decay channels. The angular asymmetry near the threshold of the  $pn \rightarrow da_0^0$  reaction was found to be large, of the order of 8–15%. © 2000 MAIK "Nauka/Interperiodica".

PACS numbers: 13.60.Le; 13.75.Cs; 14.40.Cs

The origin of the lightest, virtually mass-degenerate, scalar mesons  $a_0(980)$  ( $I^G J^{PC} = 1^- 0^{++}$ ) and  $f_0(980)$  ( $0^+ 0^{++}$ ) is one of the most important problems of hadron physics. Different assumptions exist about the structure of these mesons, from the standard  $q\bar{q}$  states [1] and their modifications (see, e.g., [2] and references therein) to the 4-quark configurations [3] and the lightest scalar mesons as "minions" in the Gribov confinement model [4]. The problem of the structure of  $a_0$  and  $f_0$  mesons is closely related to the problem of  $a_0$ - $f_0$  mixing.

If the  $a_0$  and  $f_0$  mesons have close structures, then the mixing with violation of isospin conservation could be large. Along with the direct  $a_0^0 \longleftrightarrow f_0$  transition due to isospin violation in the quark sector, these mesons can mix due to the isospin-violating interaction in the decay channels. Different mixing mechanisms are illustrated in Fig. 1. Note that the vertex of the direct  $a_0^0$ - $f_0$  interaction in Fig. 1a depends on the quark content of scalar mesons and should be extracted from the experiment. At the same time, the mixing due to the decay processes presented in Figs. 1b and 1c can be estimated rather reliably.

It is convenient to examine  $a_0^0$ - $f_0$  mixing in the reaction of production of a neutral  $a_0$  meson:

$$pn \rightarrow da_0^0. \quad (1)$$

Note that the forward-backward asymmetry in reaction (1) is absent if the isospin is conserved. As will be

shown below, observation of this asymmetry would testify to the presence of isospin-violating  $a_0^0$ - $f_0$  mixing, and the asymmetry effect should be stronger near the threshold of reaction (1).

If isospin is conserved, an isovector  $a_0$  meson can be produced near the threshold of reaction (1) only in the  $p$  wave with respect to the deuteron. At the same time, if an isoscalar  $f_0$  meson is produced in the reaction

$$pn \rightarrow df_0, \quad (2)$$

the final orbital angular momentum  $L$  of the  $df_0$  system may be zero. This conclusion follows from the isospin ( $I$ ), parity ( $P$ ), and angular momentum ( $J$ ) conservation laws. The possible quantum numbers for reactions (1) and (2) yielding final systems with the smallest orbital angular momenta ( $p$  and  $s$  waves for the  $da_0^0$  and  $df_0$  systems, respectively) are listed in the table. The total spin of the system is denoted by  $S$ . The quantum numbers presented in the table are consistent with the requirement for antisymmetry of the system with respect to the initial fermions.

Thus, if isospin is conserved, reactions (1) and (2) should have different energy and angular dependences. In particular, for the near-threshold production of stable mesons, one has

$$\sigma(pn \rightarrow da_0^0) \sim Q^{3/2}, \quad \sigma(pn \rightarrow df_0) \sim Q^{1/2} \quad (3)$$

$$(Q = \sqrt{s - m_d - \bar{m}}),$$

where  $Q$  is the energy release in the respective reaction;  $\sqrt{s}$  is the total CM energy; and  $m_d$  and  $\bar{m}$  are the deuteron and meson masses, respectively.

Let us assume that the  $f_0 \rightarrow a_0^0$  transition can proceed without isospin conservation. Then, the  $a_0$  meson in reaction (1) can be produced in the  $s$  wave with respect to the final deuteron. As is seen from the table, the initial spin state of nucleons in both reactions  $pn \rightarrow da_0^0$  and  $pn \rightarrow df_0 \rightarrow da_0^0$  is the same ( $S=1$ ). Therefore, the  $p$ -wave amplitude of the main process (1) interferes with the  $s$ -wave amplitude of the isospin-violating process  $pn \rightarrow df_0 \rightarrow da_0^0$ . Due to this interference, an asymmetry arises in the forward-backward escape of the  $a_0$  meson in reaction (1). In this case, the process with isospin conservation is energetically suppressed in the range of low  $Q$  values, as follows from Eqs. (3). For this reason, the angular asymmetry in the  $a_0$ -meson production may be large near the threshold.<sup>1</sup>

The asymmetry  $A$  for reaction (1) is defined as

$$A = \frac{\sigma_+ - \sigma_-}{\sigma_+ + \sigma_-}, \quad \sigma_{\pm} = \frac{d\sigma}{d\Omega}(z = \pm 1), \quad z = \cos\theta, \quad (4)$$

where  $\theta$  is the polar CM angle of  $a_0^0$ -meson escape, with the polar axis coinciding with the initial beam.

For the numerical estimations of asymmetry  $A$ , we first consider the  $\Lambda_{af}$  vertex determined by the diagram in Fig. 1b for the  $a_0^0 \rightarrow f_0$  transition. The  $\lambda_{\pi\eta}$  vertex corresponding to the  $\pi^0 \leftrightarrow \eta$  transition in this diagram is known from the theoretical analysis of the  $\eta \rightarrow 3\pi^0$  reaction [6] (see also [5]). We take  $\lambda_{\pi\eta} \approx -5000 \text{ MeV}^2$  as an estimate, which is the average of the theoretical values given in [5, 6]. Direct calculation of the diagram in Fig. 1b yields the following result for the contribution  $\Lambda_{\pi\eta}$  of the process indicated in Fig. 1b to  $\Lambda_{af}$ :

$$\Lambda_{\pi\eta} = \frac{\lambda_{\pi\eta} g_{a\pi\eta} g_{f\pi^0\pi^0}}{16\pi^2 \bar{m}^2} \times \left( \frac{\bar{m}^2}{m_\eta^2} \ln \frac{\bar{m}^2 - m_\eta^2}{\bar{m}^2} - \ln \frac{\bar{m}^2 - m_\eta^2}{m_\eta^2} + i\pi \right) \approx (118 - 186i) \text{ MeV}^2. \quad (5)$$

Here,  $m_\eta$  is the  $\eta$ -meson mass,  $\bar{m} = 980 \text{ MeV}/c^2$  is the mass of the  $a_0$  and  $f_0$  mesons, and  $g_{a\pi\eta}$  and  $g_{f\pi^0\pi^0}$  are the vertices of the  $a_0 \rightarrow \pi\eta$  and  $f_0 \rightarrow 2\pi^0$  decays. Estimate (5) was obtained with zero pion mass  $m_\pi = 0$  and

<sup>1</sup> Note that, for the  $pn \rightarrow d\pi^0$  reaction discussed in [5], the angular asymmetry of the near-threshold cross section is suppressed. This is due to the fact that the process with isospin conservation yields the  $d\pi^0$  system in the  $s$  wave.

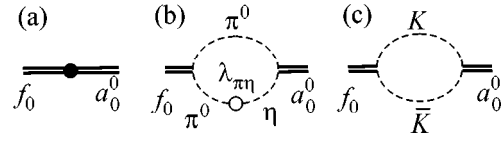


**Fig. 1.** Different types of interactions resulting in the  $a_0^0$ - $f_0$  mixing: (a) direct (or contact), (b) due to the virtual  $\pi^0 \leftrightarrow \eta$  transition, and (c) due to the mass difference between  $K^\pm$  and  $K^0$  mesons.

under the assumption that the widths of the  $a_0$  and  $f_0$  mesons with nominal mass  $\bar{m}$  are  $\Gamma(\bar{m}) \equiv \Gamma_0 = 50 \text{ MeV}/c^2$  and determined only by the decays through the  $\pi\eta$  and  $\pi\pi$  channels, respectively. Then,  $g_{a\pi\eta}^2 = 8\pi\bar{m}^2\Gamma_0/q_{\pi\eta}$ ,  $g_{f\pi\pi}^2 = 8\pi\bar{m}^2\Gamma_0/q_{\pi\pi}$ , and  $g_{f\pi^0\pi^0} = g_{f\pi\pi}/\sqrt{3}$ , where  $q_{\pi\eta}$  and  $q_{\pi\pi}$  are the relative momenta in the  $\pi\eta$  and  $\pi\pi$  systems. For the  $a_0^0$ - $f_0$  mixing angle, Eq. (5) gives the estimate  $\sin\theta_{af} \approx |\Lambda_{(\pi\eta)}/\bar{m}\Gamma_0| \approx 0.0045$ .

The mechanism of external mixing due to the  $K\bar{K}$  decay channel was recently discussed in [7], where it was found that the kinematic isospin violation due to the difference in masses of the  $K^\pm$  and  $K^0$  mesons is large and considerably stronger than that due to the  $\pi$ - $\eta$  mixing. At the same time, the strong isospin violation is concentrated in a narrow range of  $a_0$ -meson masses near the thresholds of the decays through the  $K\bar{K}$  channels.

The vertex  $\Lambda_{K\bar{K}}$  corresponding to the  $a_0^0 \leftrightarrow f_0$  transition (Fig. 1c) has the form

$$\Lambda_{K\bar{K}}(\bar{m}) = \frac{g_{aK\bar{K}} g_{fK\bar{K}}}{32\pi} \times i \left( \sqrt{\frac{\bar{m} - 2m_{K^+}}{m_K} + i0} - \sqrt{\frac{\bar{m} - 2m_{K^0}}{m_K} + i0} \right), \quad (6)$$

where  $m_{K^+} = 493.7 \text{ MeV}/c^2$  and  $m_{K^0} = 497.7 \text{ MeV}/c^2$  are the masses of, respectively, charged and neutral kaons [8];  $m_K = (m_{K^+} + m_{K^0})/2$ ; and  $g_{aK\bar{K}}$  and  $g_{fK\bar{K}}$  are the vertices of the  $a_0 \rightarrow K\bar{K}$  and  $f_0 \rightarrow K\bar{K}$  decays,

**Table**

	$pn \rightarrow da_0$		$pn \rightarrow df_0$	
$I$	1	1	0	0
$S$	1	1	1	1
$L$	1, 3	1	0, 2	0
$P$	-1	-1	1	1

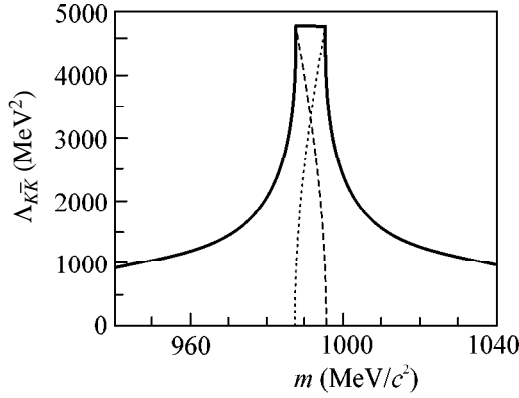


**Fig. 2.** Vertex function  $\Lambda_{K\bar{K}}$  (6) vs.  $a_0$ -meson mass  $m$ . The solid, dashed, and dotted curves correspond to its absolute value, real part, and imaginary part, respectively. The dashed (dotted) curve coincides with the solid curve for  $m < 2m_{K^+}$  ( $m > 2m_{K^0}$ ).

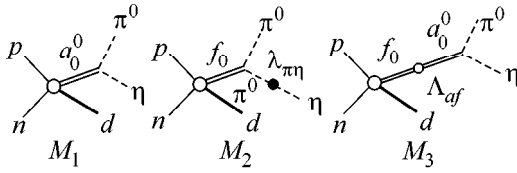


**Fig. 3.** Zero- and first-order isospin-violating diagrams of the  $pn \rightarrow d\pi^0\eta$  process.

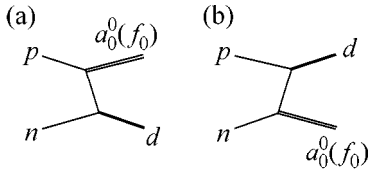


**Fig. 4.** Diagrams for the  $a_0(f_0)$ -meson production in impulse approximation.

respectively. In addition,  $g_{aK\bar{K}}^2 = 2g_{aK^+K^-}^2$ ,  $g_{fK\bar{K}}^2 = 2g_{fK^+K^-}^2$ ,  $g_{aK^0\bar{K}^0} = -g_{aK^+K^-}$ , and  $g_{fK^0\bar{K}^0} = g_{fK^+K^-}$ . To numerically estimate Eq. (6), we set  $g_{aK\bar{K}} = g_{a\pi\eta}$ , in agreement with the experimental restriction  $g_{aK\bar{K}}^2/g_{a\pi\eta}^2 = 0.91 \pm 0.11$  [9]. We also assume that  $g_{fK\bar{K}}^2 = g_{aK\bar{K}}^2$  and  $g_{aK^+K^-} = -g_{fK^+K^-}$  [the relative signs of the  $a_0$ - and  $f_0$ -meson decay vertices are consistent with the predictions of SU(3) symmetry].<sup>2</sup> The function  $\Lambda_{K\bar{K}}(m)$  is shown in Fig. 2. This function sharply changes near the

<sup>2</sup> It is assumed that the  $a_0$  isotriplet and  $f_0$  isosinglet belong to the same scalar meson octet.

thresholds of the  $K^+K^-$  and  $K^0\bar{K}^0$  systems within the mass intervals comparable to the  $2m_{K^0} - 2m_{K^+} \approx 8 \text{ MeV}/c^2$  difference, which is considerably smaller than the width of the  $a_0$  and  $f_0$  mesons. It is seen that  $|\Lambda_{K\bar{K}}| \gg |\Lambda_{\pi\eta}|$  near the  $K\bar{K}$  thresholds.

Let us assume that the signal from the  $a_0^0$ -meson production is detected by identifying the  $\pi^0\eta$  final state. In this case, the use of perturbation theory for the isospin-violating interaction gives three diagrams dominating the cross section for the process. They are shown in Fig. 3. The  $M_1$  diagram corresponds to the process with isospin conservation. The  $M_2$  and  $M_3$  diagrams are first-order corrections in the isospin-violating interaction to the diagram  $M_1$ . The  $M_2$  diagram is irrelevant to the  $a_0$ -meson production but does contribute to the  $s$ - $p$  interference under discussion. This contribution corresponds to the interference of diagrams  $M_2$  and  $M_1$  through the  $a_0^0$ - $f_0$  mixing mechanism (Fig. 1b). The respective amplitudes  $M_{1,2,3}$  are

$$M_1 = M_a G_a g_{a\pi\eta}, \quad M_2 = M_f G_f \frac{g_{f\pi^0\pi^0} \lambda_{\pi\eta}}{m_\eta^2 - m_\pi^2}, \quad (7)$$

$$M_3 = M_f G_f \Lambda_{af} G_a g_{a\pi\eta},$$

where  $\Lambda_{af} = \Lambda_{\text{dir}} + \Lambda_{\pi\eta} + \Lambda_{K\bar{K}}$  is the vertex corresponding to the  $a_0^0 \leftrightarrow f_0$  transition. The vertex  $\Lambda_{\text{dir}}$  of direct interaction (Fig. 1a) was not taken into account; i.e.,  $\Lambda_{af} = \Lambda_{\pi\eta} + \Lambda_{K\bar{K}}$ . In Eqs. (7),  $G_a$  and  $G_f$  are the propagators of the  $a_0$  and  $f_0$  mesons, respectively:

$$G_a = G_f = \frac{1}{2\bar{m}m - \bar{m} + i\Gamma(m)/2}, \quad (8)$$

$$\Gamma(m) = \Gamma_0 + \frac{g_{aK\bar{K}}^2}{8\pi\bar{m}^2} \sqrt{m_K(m - 2m_K) + i0},$$

where the width  $\Gamma(m)$  takes into account that the resonances may decay through the  $K\bar{K}$  channel [10] and  $m$  is the mass of the  $\pi\eta$  system. In Eq. (7),  $M_a$  and  $M_f$  denote the amplitudes of production of the  $a_0$  and  $f_0$  mesons in reactions (1) and (2), respectively. These amplitudes can be estimated from the diagrams of the impulse approximation (Fig. 4). With allowance made only for the  $s$ -wave component of the deuteron wave function (WF), the expressions for  $M_a$  and  $M_f$  antisymmetrized over the initial nucleons have the form

$$M_a = g_{aNN} \sqrt{m_N} (u(q_1) - u(q_2)) X, \quad (9)$$

$$M_f = g_{fNN} \sqrt{m_N} (u(q_1) + u(q_2)) X.$$

Here,  $g_{aNN}$  and  $g_{fNN}$  are the vertices for the  $a_0$ - and  $f_0$ -meson coupling to the nucleon;  $m_N$  is the nucleon

mass;  $u(q)$  is the deuteron WF;  $q_1(q_2)$  is the relative momentum in the deuteron vertex corresponding to the emission of an  $a_0^0$  or  $f_0$  meson by the initial proton (neutron); and  $X = \varphi_p^T \sigma_2 \epsilon \cdot \sigma \varphi_n$  is the spin factor, where  $\varphi_p$  and  $\varphi_n$  are the proton and neutron spinors, respectively, and  $\epsilon$  is the deuteron polarization vector. Let  $\mathbf{p}$  and  $\mathbf{k}$  be the CM 3-momenta of the initial proton and the final  $\pi\eta$  system, respectively. For  $m \approx \bar{m}$ , one has  $k \ll p$  and  $q_{1,2}^2 \approx p^2 \pm (E_N/m_N)(\mathbf{p} \cdot \mathbf{k})$  near the threshold  $Q = \sqrt{s} - m_d - \bar{m} \approx 0$  of reaction (1), where  $E_N \approx m_N + \bar{m}/2$  is the total nucleon CM energy. Then, Eq. (9) takes the form

$$M_a = 2g_{aNN}\sqrt{m_N}\frac{du(p)}{dp^2}\frac{E_N}{m_N}(\mathbf{p} \cdot \mathbf{k}) \times X, \quad (10)$$

$$M_f = 2g_{fNN}\sqrt{m_N}u(p) \times X.$$

It follows from these expressions that at small  $k$  values the amplitude  $M_a$  of  $a_0$ -meson production is much smaller than the amplitude  $M_f$  of  $f_0$ -meson production. Note that the relative contributions of the  $p$ - and  $s$ -wave amplitudes  $M_a$  and  $M_f$  to the cross section for reaction (1) depend on the width of the  $a_0$  and  $f_0$  mesons and on the restrictions on the mass range of the final  $\pi\eta$  system. In what follows, we set  $g_{aNN} \equiv g_{fNN}$  in Eq. (10). For the deuteron WF with momenta  $p \sim 1$  GeV/c, we take  $u(p) \sim p^{-n}$ . The Hulthen WF corresponds to  $n = 4$ ; i.e.,  $du(p)/dp^2 = -2p^{-2}u(p)$ . This approximation for the deuteron WF and the impulse approximation for the amplitudes  $M_a$  and  $M_f$  cannot give reliable estimates for the absolute values of the cross sections and are used only for estimating the asymmetry  $A$ . The differential cross section for the reaction  $pn \rightarrow d\pi^0\eta$  can be written as

$$\frac{d\sigma}{d\Omega} = N \int_{m_{\min}}^{m_{\max}} |M_1 + M_2 + M_3|^2 k dm. \quad (11)$$

In the range of threshold energies  $Q \sim 0$  and  $m \sim \bar{m}$  values close to the thresholds of the  $K\bar{K}$  systems, only the dependence on mass  $m$  should be taken into account. The  $m$  dependence of the amplitudes  $M_{1,2,3}$  (7) is taken into account for  $\Lambda_{K\bar{K}}$  [Eq. (6)];  $G_a, G_f$ , and  $\Gamma(m)$  [Eqs. (8)]; and for the relative momentum  $k = \sqrt{2\mu(Q + \bar{m} - m)}$ , where  $\mu = m_d\bar{m}/(m_d + \bar{m})$ . To a common factor, the amplitudes  $M_a$  and  $M_f$  (10) for the unpolarized particles can be written as  $M_a = -2(E_N/m_N)(k/p)z$  and  $M_f = 1$ . The normalization constant  $N$  in Eq. (11) contains weakly varying factors, and its magnitude is of no interest to us. The quantities  $p$  and  $E_N$  are calculated at the threshold; i.e.,  $E_N = m_N + \bar{m}/2$  and  $p = \sqrt{\bar{m}(m_N + \bar{m}/4)} \approx 1$  GeV/c.

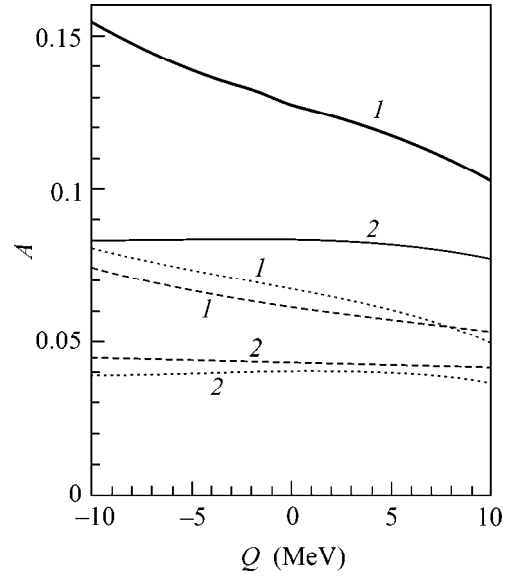


**Fig. 5.** Plots of the asymmetry  $A$  of  $a_0^0$ -meson production in reaction (1) vs. the energy release  $Q$  (3). Curves 1 and 2 correspond to two lower limits [specified by  $C = 1$  and  $C = 2$  (see text)] on the interval of  $a_0^0$  masses. The dashed (dotted) curves are calculated by taking account of the  $a_0^0$ - $f_0$  mixing through only the virtual  $\pi^0 \longleftrightarrow \eta$  transition ( $K\bar{K}$  decay channel). The solid curves are obtained with allowance made for both mixing mechanisms.

The width of the mass interval ( $m_{\min}, m_{\max}$ ) of the  $\pi^0\eta$  system (more precisely, its lower limit  $m_{\min}$ ), in which the  $a_0$  meson is detected, is an important factor for estimating asymmetry  $A$  (4). When the mass of  $\pi^0\eta$  system decreases (below the nominal mass  $\bar{m}$ ), the momentum  $k$  increases, resulting in both the enhancement in the  $p$ -wave amplitude  $M_a$ , as compared to the  $s$ -wave amplitude  $M_f$ , and the dependence of the asymmetry  $A$  on  $m_{\min}$ . In what follows, we specify integral (11) between the limits  $m_{\max} = Q + \bar{m}$  (kinematic boundary) and  $m_{\min} = \bar{m} - C(\Gamma_0/2)$ , where  $C$  is a variable parameter. The calculated [by Eqs. (4) and (11)] asymmetry  $A$  of the  $\pi^0\eta$ -system production is shown in Fig. 5 as a function of energy release  $Q$  (3). The calculations were carried out for two lower limits (corresponding to  $C = 1$  and  $C = 2$ ) on the mass of the  $\pi^0\eta$  system. A decrease in the effect with increasing parameter  $C$  is due to the increase in the role of the main (isospin-conserving) process of  $a_0$ -meson production in the  $p$  wave. Note that the contribution of the  $p$ -wave amplitude to the cross section dominates over the  $s$ -wave contribution in both variants if the  $a_0$ -meson width is taken into account. For this reason, the relative contribution of the  $s$ - $p$  interference and, hence, the asymmetry, decrease upon enhancing the  $p$  wave. The dashed

(dotted) curves in Fig. 5 correspond to the asymmetry calculations taking account of only one mixing mechanism given by the diagram in Fig. 1b (Fig. 1c), i.e., for  $\Lambda_{af} = \Lambda_{\pi\eta}$  ( $\Lambda_{af} = \Lambda_{K\bar{K}}$ ). The diagram  $M_2$  (Fig. 2) is automatically ignored in calculating the dotted curves.

As is seen in Fig. 5, the asymmetry in the near-threshold  $a_0$ -meson production is rather large (about 8–15%), which enables one to believe that it can be experimentally observed.

Note in conclusion that our estimates of the asymmetry may be improved. This is primarily true for the calculation of the amplitudes  $M_a$  and  $M_f$  of the  $a_0$ - and  $f_0$ -meson production. An approach with the inclusion of diagrams describing intermediate rescattering processes (see, e.g., [11]) seems to be more reliable than the inclusion of the pole diagrams (Fig. 4) that depend on the behavior of the deuteron WF at high momenta  $\sim 1$  GeV/c, where the WF is poorly known.

We are grateful to all participants of the Workshop on the ANKE-Spectrometer Program held at the ITEP (July 2000) and particularly to K.G. Boreskov and V.P. Chernyshev for helpful discussions and interest in this study.

## REFERENCES

1. N. A. Tornqvist, Phys. Rev. Lett. **49**, 624 (1982).
2. V. V. Anisovich, hep-ph/9712504, 1997.
3. N. N. Achasov and G. N. Shestakov, Usp. Fiz. Nauk **161**, 53 (1991) [Sov. Phys. Usp. **34**, 471 (1991)]; Usp. Fiz. Nauk **142**, 361 (1984) [Sov. Phys. Usp. **27**, 161 (1984)]; N. N. Achasov and G. N. Shestakov, Z. Phys. C **41**, 309 (1988).
4. V. N. Gribov, LU-TP-91-7; ORSAY Lectures on Confinement 1, LPT HE-ORSAY-92-60; V. N. Gribov, Eur. Phys. J. C **10**, 91 (1999); F. Close, Yu. L. Dokshitzer, V. N. Gribov, *et al.*, Phys. Lett. B **319**, 291 (1993).
5. J. A. Niskanen, nucl-th/9809009, 1998.
6. S. A. Coon and M. D. Scadron, Phys. Rev. C **51**, 2923 (1995); S. A. Coon, B. H. J. McKellar, and M. D. Scadron, Phys. Rev. D **34**, 2784 (1986); Ll. Ametller, C. Ayala, and A. Bramon, Phys. Rev. D **30**, 674 (1984).
7. B. Kerbikov and F. Tabakin, nucl-th/0006017, 2000; submitted to Phys. Rev. C.
8. Review of Particle Physics, Eur. Phys. J. C **3**, 1 (1998).
9. S. Teige, B. B. Brabson, R. R. Crittenden, *et al.*, Phys. Rev. D **59**, 012001 (1999).
10. S. M. Flatte, Phys. Lett. **63**, 224 (1975).
11. V. Yu. Grishina, L. A. Kondratyuk, E. L. Bratkovskaya, *et al.*, nucl-th/0007074, 2000; submitted to EJP A.

*Translated by R. Tyapayev*

# Microscopic Model of Optically Induced Anisotropy of Third-Order Nonlinearity in Azo-Dye Polymer Systems<sup>1</sup>

V. M. Churikov

Department of Physics, National Chung Cheng University, Ming Hsiung, Chiayi 621, Taiwan, ROC

e-mail: victor@phy.ccu.edu.tw

Received September 6, 2000

A large photoinduced reversible change of third-harmonic generation in azo-dye polymer thin films was recently observed. In this work, the microscopic interpretation of this phenomenon is given. The model presented is based on an angular hole burning and molecular reorientation due to *trans*–*cis* photoisomerization of azo-dye molecules. © 2000 MAIK “Nauka/Interperiodica”.

PACS numbers: 42.65.Ky; 42.70.Jk; 78.66.Qn

Optical phenomena related to the *trans*–*cis* photoisomerization of azobenzene molecules are of stable interest because of potential applications in integrated optics and data storage devices [1]. It is well known that isomerization with respect to the –N=N– double bond results in quasi-permanent birefringence and dichroism [2]. The mechanism of the induced anisotropy can be summarized as follows. Since the azo-dye molecule [e.g., disperse red 1 doped polymethylmethacrylate (DR1-PMMA)] in the *trans* form can be considered as a one-dimensional (rodlike) molecule, the probability of excitation by linearly polarized light can be written as  $\text{Pr}(\theta_p) = \sigma_T I_p \cos^2 \theta_p$ , where  $\sigma_T$  is the cross section for absorption of a photon by *trans* molecules parallel to the pump field,  $I_p$  is the pump intensity, and  $\theta_p$  is the angle between the light-wave electric field and the molecular axis. This selective excitation leads to angular hole burning (AHB) in the distribution of *trans* molecules, because, after excitation, the molecules tend to relax to the *cis* state with smaller polarizabilities. Reverse thermal *cis*–*trans* relaxation can proceed in two different ways: (1) to the original *trans* state and (2) to the *trans* state with a different orientation (Fig. 1). If a molecule oriented along the pump polarization is excited, the relaxation in the second way reduces the probability of repeated excitation; therefore, some molecular reorientation occurs. This molecular reorientation mechanism is important when the *cis* population is negligible (i.e., the pump intensity is low, and if the thermal relaxation from *cis* to *trans* is fast).

The simplified AHB model [3] predicts an index variation (or an optical density variation) three times larger for a probe beam polarized along the polarization of the pump beam than for a probe beam polarized per-

pendicularly ( $\Delta n_{\parallel} = 3\Delta n_{\perp}$ ). However, the variation of the index observed experimentally is relatively small ( $\Delta n \sim 3 \times 10^{-3}$ ), so it can be detected only with very sensitive techniques such as attenuated total reflection [1].

In this letter, a microscopic model of photoinduced anisotropy of cubic nonlinear susceptibility in azo-doped polymer systems is presented. Contributions of the AHB and reorientation mechanisms are distinguished. Nonlinear optical properties of the molecular distribution anisotropy are of interest, because the general expression for second hyperpolarizability  $\gamma$  contains terms resonant for  $\omega$ ,  $2\omega$ , and  $3\omega$  [4], so that the third-order effects are expected to be more sensitive to a change in the molecular conformation. Moreover, a simple third-harmonic (TH) generation technique can be used to probe the induced anisotropy.

Several simplifying assumptions based on previous results are made in our model. First, a simple three-level model is applied (Fig. 2). In fact, the reverse *cis*–*trans* photoisomerization also exists, in competition with the direct *trans*–*cis* one, but can be neglected if the pump frequency is on the red side of the *trans* absorption spectrum [2]. Second, third-order susceptibility of an azo-polymer is formed by only *trans* molecules (the contribution of the *cis* molecules and the polymer matrix is neglected). Third, second hyperpolarizability of a *trans* molecule has only one nonzero component,  $\gamma = \gamma_{1111}$ , where the subscript means the direction of the molecular axis. The general expression for  $\chi^{(3)}$  responsible for TH generation by linearly polarized light will then be

$$\chi^{(3)}(-3\omega, \omega, \omega, \omega) = f^4 \gamma \int N_T(\Omega) \cos^4 \theta d\Omega, \quad (1)$$

where  $f^4 = f_{\omega}^3 f_{3\omega}$  is a collection of the local field factors,  $N_T(\Omega)$  is the density of *trans* molecules oriented in the direction  $\Omega$ , and  $\theta$  is the angle between the probe

<sup>1</sup> This article was submitted by the authors in English.

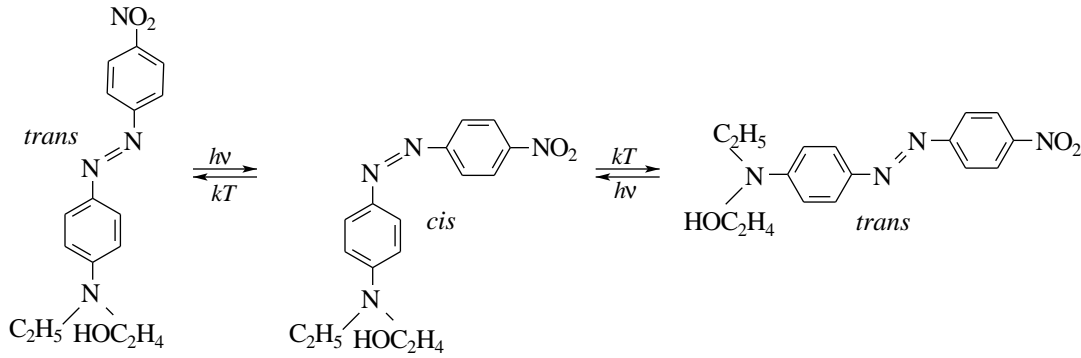


Fig. 1. *trans*–*cis* photoisomerization and reverse thermal *cis*–*trans* relaxation of DR1 molecule.

beam electric field and the molecular direction  $\Omega$ . In the three-level model, the dynamics of the *trans* population is described by the equation

$$dN_T(\Omega)/dt = -N_T(\Omega)\phi_{TC}\text{Pr}(\theta_p) + N_C(\Omega)\eta_{CT}, \quad (2)$$

where  $N_T(\Omega)$  and  $N_C(\Omega)$  are the densities of *trans* and *cis* molecules oriented in the direction  $\Omega$ ,  $\text{Pr}(\theta_p)$  is the probability of excitation of a *trans* molecule oriented at the angle  $\theta_p$ ,  $\phi_{TC}$  is the quantum yield for the *trans*-to-*cis* transition, and  $\eta_{CT}$  is the thermal relaxation rate from *cis* to *trans*. Taking into account the relation  $N_T(\Omega) + N_C(\Omega) = N/4\pi$ , where  $N$  is a density of *trans* molecules in the original isotropic distribution, one can obtain the stationary angular molecular distribution

$$N_T(\Omega) = \frac{N}{4\pi}(1 + \phi_{TC}\text{Pr}(\theta_p)/\eta_{CT})^{-1}. \quad (3)$$

In the approximation of a weak pump (i.e., far from excitation saturation), the linear development of Eq. (3) gives

$$N_T(\Omega) = \frac{N}{4\pi}(1 - AI_p \cos^2 \theta_p). \quad (4)$$

In Eq. (4), we use the expression for  $\text{Pr}(\theta)$  and introduce  $A = \sigma_T \phi_{TC}/\eta_{CT}$ . If  $I_p = 0$ , the angular distribution of molecules is isotropic and

$$\begin{aligned} \chi_{iso}^{(3)} &= \frac{1}{4\pi} f^4 \gamma N \int \cos^4 \theta d\Omega \\ &= \frac{1}{2} f^4 \gamma N \int_0^\pi \cos^4 \theta \sin \theta d\theta = \frac{1}{5} f^4 \gamma N. \end{aligned} \quad (5)$$

This result is in agreement with the Wong–Garito formula [5] applied to the case of random molecular orientation.

Now the  $\chi_{\parallel}^{(3)}(-3\omega, \omega, \omega, \omega)$  component responsible for TH generation by a probe beam polarized along the

polarization of the pump beam is calculated. In this case,  $\theta_p = \theta$  and one has

$$\begin{aligned} \chi_{\parallel}^{(3)} &= \frac{1}{2} f^4 \gamma N \\ &\times \int_0^\pi (1 - AI_p \cos^2 \theta) \cos^4 \theta \sin \theta d\theta = \chi_{iso}^{(3)} + \Delta\chi_{\parallel}^{(3)}, \end{aligned} \quad (6)$$

with  $\Delta\chi_{\parallel}^{(3)} = -\frac{1}{7} f^4 \gamma N AI_p$ . For a perpendicularly polarized probe beam,  $\cos \theta_p = \sin \theta_p \cos \alpha$ , where  $\alpha$  is an azimuthal angle (Fig. 3). Substituting this expression in Eq. (4), one has

$$\begin{aligned} \chi_{\perp}^{(3)} &= \frac{1}{4\pi} f^4 \gamma N \\ &\times \int_0^{2\pi} \int_0^\pi (1 - AI_p \sin^2 \theta \cos^2 \alpha) \cos^4 \theta \sin \theta d\theta d\alpha \\ &= \chi_{iso}^{(3)} + \Delta\chi_{\perp}^{(3)}, \end{aligned} \quad (7)$$

with  $\Delta\chi_{\perp}^{(3)} = -\frac{1}{35} f^4 \gamma N AI_p$ . Therefore, one can see that  $\chi_{\parallel}^{(3)}/\Delta\chi_{\perp}^{(3)} = 5$ . This result shows that the photoinduced anisotropy of  $\chi_{\parallel}^{(3)}(-3\omega, \omega, \omega, \omega)$  due to the AHB mechanism is appreciably larger than that of the refractive index ( $\Delta n_{\parallel}/\Delta n_{\perp} = 3$  [3]).

Another mechanism responsible for the optically induced anisotropy is angular redistribution of molecules. This mechanism was widely developed to explain photoinduced birefringence and dichroism [6]. If the pump intensity is low enough, the *trans* molecules oriented near the pump polarization finally turn out near the plane perpendicular to the pump electric-field vector. Therefore, in contrast to the AHB mechanism, the total number of *trans* molecules remains unchanged.

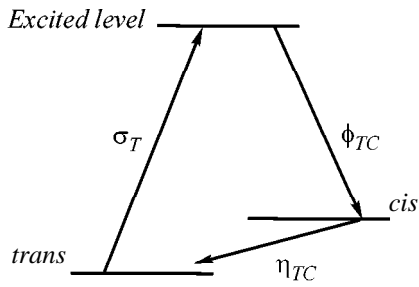


**Fig. 2.** Simplified three-level scheme for *trans*–*cis* photoisomerization. Here,  $\sigma_T$  is the cross section for absorption of a photon by molecules parallel to the pump field,  $\phi_{TC}$  is the quantum yield for the *trans*-to-*cis* transition, and  $\eta_{CT}$  is the thermal relaxation rate from *cis* to *trans*.

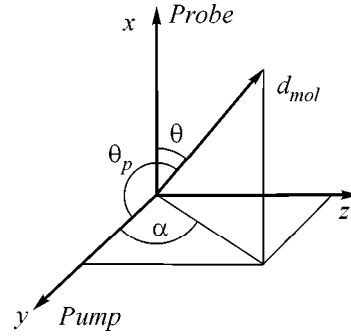


**Fig. 3.** The diagram of molecular orientation with respect to the pump and probe electric fields. The pump and probe beams are polarized perpendicularly.

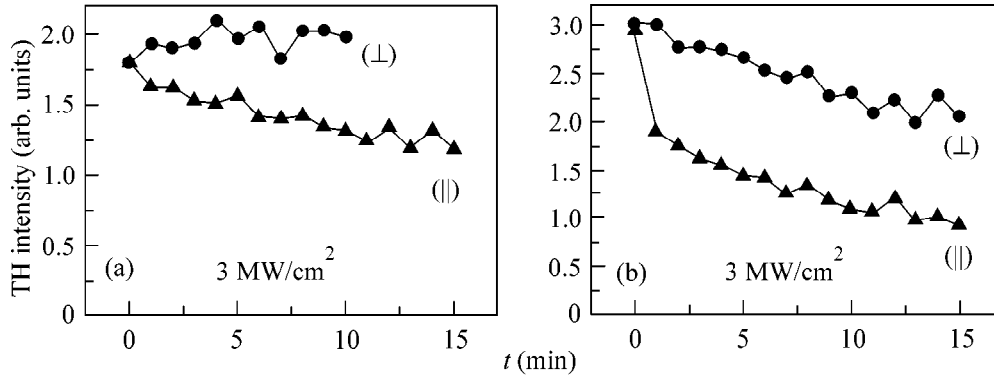


**Fig. 4.** The TH signal in DR1-PMMA thin film pumped by 532-nm light as a function of time. The pump peak intensities are (a)  $3 \text{ MW/cm}^2$  and (b)  $30 \text{ MW/cm}^2$ . The pump is switched on at the moment  $t = 0$ . The TH is generated by the probe copolarized (||) or cross-polarized ( $\perp$ ) with the fundamental frequency pump. A detailed description of the experimental setup can be found in [7].

Let us suppose that there are  $N_{\parallel}$  molecules with the orientation near the pump polarization. After reorientation, these molecules form isotropic angular distribution near the plane perpendicular to the pump electric-field vector. Taking into consideration only  $N_{\parallel}$  molecules, one has

$$\Delta\chi_{\parallel}^{(3)} = -f^4\gamma N_{\parallel}, \quad (8)$$

$$\Delta\chi_{\perp}^{(3)} = \frac{N_{\parallel}}{2\pi} f^4 \gamma N \int_0^{2\pi} \cos^4 \theta d\theta = \frac{3}{8} f^4 \gamma N_{\parallel}. \quad (9)$$

Therefore, the angular redistribution mechanism gives a positive change of  $\chi^{(3)}$  for the probe beam polarized perpendicularly:

$$\Delta\chi_{\perp}^{(3)} = -\frac{3}{8} \Delta\chi_{\parallel}^{(3)}. \quad (10)$$

Equation (10) shows that the angular redistribution of molecules can reduce the decrease in  $\chi_{\perp}^{(3)}$  caused by the AHB and, for a low-intensity pump, can even result in an increase in  $\chi_{\perp}^{(3)}$ . It should be noted that the similar

consideration for index gives the relationship  $\Delta n_{\perp} = -\Delta n_{\parallel}/2$  (see, for example, [6]).

Our recent experiments [7] have shown a remarkable decrease in TH generation in DR1-PMMA thin film pumped by the second harmonic of a Nd:YAG laser. The observed TH generation decrease was too large to be explained by a change in absorption due to *trans*–*cis* isomerization [8]. The change in the TH intensity was about 4 times for copolarized pump and probe beams and only about 20% for perpendicularly polarized beams. The decrease was almost completely reversible after a few minutes of dark relaxation. Previous dichroism experiments [8] have shown that, after the pumping beam is switched off, the *cis* population responsible for AHB disappears in a few seconds, but the anisotropy due to the molecular reorientation can survive for several hours. Therefore, one can conclude that the  $\chi^{(3)}$  anisotropy studied in [7] is mainly due to the AHB mechanism. However, lately we observed an increase in the TH generated by the probe which was polarized perpendicularly to the polarization of the low-intensity pump. Figure 4 demonstrates that, at low intensities, the reorientation mechanism dominates over the AHB mechanism, but the situation is quite the

reverse at high intensities. This observation, along with the results of [7], can serve as an evidence of the model presented here. The large change in TH generation observed in [7] is of interest for applications such as optical memories, transient gratings, and photonic band-gap devices, because it gives an opportunity for all-optical control of third-order nonlinear properties of polymer materials.

In conclusion, the model presented predicts the third-order nonlinearity anisotropy in azo-dye polymer systems pumped by linearly polarized light. The model is in agreement with the results of recent experimental study of TH generation properties in azo-doped polymer thin films.

I thank C.C. Hsu for valuable discussion of the problem. The work was supported by the National Science Council and the Academia Sinica of Taiwan.

Permanent address: South Ural State University, Nonlinear Optics Laboratory, pr. Lenina 76, Chelyabinsk, 454080 Russia.

## REFERENCES

1. L. M. Hayden, G. F. Sauter, F. R. Ore, *et al.*, J. Appl. Phys. **68**, 456 (1990).
2. M. Dumont, S. Hosotte, G. Froc, and Z. Sekkat, Proc. SPIE **2042**, 2 (1994).
3. Z. Sekkat and M. Dumont, Appl. Phys. B **B53**, 121 (1991).
4. P. N. Prasad and D. J. Williams, *Introduction to Nonlinear Optical Effects in Molecules and Polymers* (Wiley, New York, 1991).
5. K. Y. Wong and A. F. Garito, Phys. Rev. A **34**, 5051 (1986).
6. Z. Sekkat and M. Dumont, Appl. Phys. B **B54**, 486 (1992).
7. V. M. Churikov and C. C. Hsu, Appl. Phys. Lett. **77**, 2095 (2000).
8. Z. Sekkat, D. Morichere, M. Dumont, *et al.*, J. Appl. Phys. **71**, 1543 (1992).

# Conductivity of Carbon Nanotubes in a Longitudinal Magnetic Field

P. M. Ostrovsky

Landau Institute for Theoretical Physics, Russian Academy of Sciences, ul. Kosygina 2, Moscow, 117940 Russia

Received September 14, 2000

Multiwall carbon nanotubes exhibit oscillations of magnetoresistance with the period  $\Phi_0 = hc/2e$  [A. Bachtold, C. Strunk, J.-P. Salvetat, *et al.*, Nature **397**, 673 (1999)]. This effect is analogous to the Sharvin effect for a normal metal [D. Yu. Sharvin and Yu. V. Sharvin, Pis'ma Zh. Éksp. Teor. Fiz. **34**, 285 (1981)]. It is shown that, along with the magnetoresistance peaks corresponding to the flux values that are multiples of  $\Phi_0$ , additional peaks with a period three times shorter can be observed in carbon nanotubes. © 2000 MAIK “Nauka/Interperiodica”.

PACS numbers: 72.20.My; 75.50.-y

Carbon nanotubes [1] possess interesting transport properties. Depending on the geometric structure, a single-wall tube can be a dielectric, a metal, or a semiconductor [2]. Metallic tubes can be considered, to a good approximation, as one-dimensional conductors. However, in experiment [3], unique conditions were obtained for which a nanotube exhibits the properties of a two-dimensional conductor, i.e., the properties that are characteristic of normal metal tubes. In this case, we are dealing with the Sharvin effect [4, 5]: the magnetoresistance oscillates with the period  $\Phi_0 = hc/2e$  and reaches its maximal values at  $\Phi = n\Phi_0$ . Below, we will show that the specific structure of carbon nanotubes can give rise to magnetoresistance features that are not characteristic of normal metal tubes. These features consist in the appearance of additional magnetoresistance peaks which occur with a period three times shorter than the fundamental period of oscillations in the Sharvin effect.

The main experimental difficulty is related to the fact that it is practically impossible to obtain a single-wall tube with a diameter sufficiently large for observing the magnetic-field effects. In the aforementioned experiment [3], multiwall tubes were used. Following the authors of the experiment, we will assume that the current flows only in the outermost layer of the tube.

The weak localization effects, including the Sharvin effect, are observed in metals; i.e., they require large values of the parameter  $k_F l$ . For nanotubes, this is not the case because of the semimetal properties of carbon. It is known that, in pure carbon, the electronic spectrum is linear and the Fermi surface consists of separate “conic” points located at the vertices of the first Brillouin zone (see the description of the electronic spectrum of graphite and references, e.g., in [6]). However, the observation of the Sharvin effect in multiwall nanotubes indicates that, for some reasons, the outermost layer of a tube exhibits metallic (in terms of  $k_F l \gg 1$ )

properties. One such reason may be the effect of contacts. Because of the contact voltage, the Fermi level in a tube can be displaced from the conic point, which will result in a finite Fermi surface. Another possible reason is the effect of the inner layers of the tube. The difference in the curvatures of the inner and outer layers gives rise to a difference in the chemical potentials and to a redistribution of the electron density. It is also possible that the electron density changes because of doping impurities which are present inside the tube or in the substrate. For a more precise experiment, it would be expedient to make a special “gate” allowing the position of the Fermi level to be varied in the tube.

For the Sharvin effect, it is necessary that the mean free path of electrons be less than the perimeter of the tube:

$$\tau v_0 \ll r, \quad (1)$$

where  $v_0$  is the Fermi velocity,  $r$  is the tube radius, and  $\tau$  is the mean free time. This condition does not hold for single-wall tubes, but, in multiwall tubes, the inner tube layers represent a powerful source of disorder. In addition, the quantum coherence condition should be satisfied:

$$r \ll \sqrt{\tau \tau_\phi} v_0. \quad (2)$$

This can be achieved by selecting the appropriate temperature regime. The observation of the Sharvin effect in carbon nanotubes [3] can be considered as the experimental verification of the applicability of the weak localization approximation.

The model considered below assumes that the Fermi surface for the electrons of the carbon plane consists of two circles with centers at the vertices of the first Brillouin zone (Fig. 1). We will mark these valleys by the “+” and “−” signs. Since the potential is determined by the impurities whose dimensions are comparable with

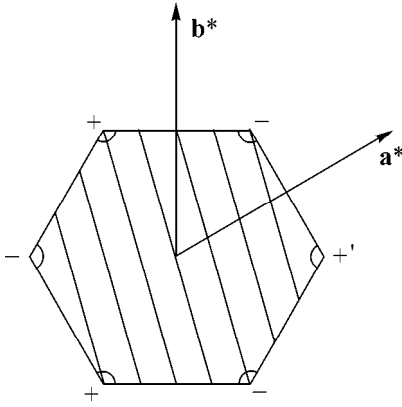


**Fig. 1.** First Brillouin zone of the carbon plane. The circular arcs near the vertices represent the Fermi surface;  $\mathbf{a}^*$  and  $\mathbf{b}^*$  represent the basis of the reciprocal lattice. The allowed lines for  $k$  are shown for a (7, 2) tube (the notation for the tube corresponds to [2]). The “+” and “-” signs indicate two parts of the Fermi surface (valleys).

the lattice period, it is necessary to take into account the dependence of the scattering amplitude on the momentum. We propose the following phenomenological approach. We introduce two mean free times, which correspond to the intravalley ( $\tau_0$ ) and intervalley ( $\tau'$ ) scattering:

$$\begin{array}{c} + \quad + \\ \hline \rightarrow \quad \rightarrow \\ \hline + \quad + \end{array} = \begin{array}{c} + \quad + \\ \hline \rightarrow \quad \rightarrow \\ \hline - \quad - \end{array} = \frac{1}{2\pi v \tau_0}; \quad \begin{array}{c} + \quad - \\ \hline \rightarrow \quad \rightarrow \\ \hline - \quad + \end{array} = \frac{1}{2\pi v \tau'}, \quad (3)$$

where  $v$  is the density of states in one valley. Evidently,  $\tau' > \tau_0$ . The total mean free time is determined by the expression  $\tau^{-1} = \tau_0^{-1} + \tau'^{-1}$ .

Because of the periodic boundary conditions, when the plane is rolled up into a cylinder, only those momenta which lie on certain lines (Fig. 1) remain allowed [2]. However, when the mean free path is less than the perimeter of the tube, i.e., when condition (1) is satisfied, the quantization of the transverse momentum of electrons is suppressed and the conduction becomes metallic for tubes of any structure.

For one valley, the calculations are similar to those described in [5]. The quantum correction to the conductivity has the form [7]

$$\frac{\Delta\sigma}{\sigma} = -2\tau^2 \int \frac{d^2k}{(2\pi)^2} C(\mathbf{k}). \quad (4)$$

The integration is performed over all allowed momenta. Since the lifetime of a cooperon  $\tau_\phi$  is large [see condition (2)], it is necessary to take into account the dimensional quantization due to the periodic boundary condi-

tions. The cooperon propagator  $C(\mathbf{k})$  corresponds to a sum of “ladders” of the following type:

$$\begin{aligned} C(\mathbf{k} = \mathbf{p}_1 + \mathbf{p}_2) &= \begin{array}{c} \mathbf{p}_1 \\ \hline \rightarrow \\ \hline \mathbf{p}_2 \\ \hline \rightarrow \\ \hline \end{array} + \begin{array}{c} \mathbf{p}_1 \\ \hline \rightarrow \\ \hline \mathbf{p}_2 \\ \hline \rightarrow \\ \hline \end{array} + \dots \\ &= \frac{1}{2\pi v \tau^2 D k^2 - i\omega}; \quad \omega\tau, \tau D k^2 \ll 1. \end{aligned} \quad (5)$$

For a cylinder, we obtain the result similar to that presented in [5]:

$$\frac{\Delta\sigma}{\sigma} = -\frac{1}{\pi v} \sum_l \int \frac{dk_{\parallel}}{2\pi} \left[ D \left( k_{\parallel}^2 + \frac{l^2}{\tau^2} \right) + \frac{1}{\tau_\phi} \right]^{-1}. \quad (6)$$

The summation and the integration are performed within the first Brillouin zone. In a magnetic field, the  $l$  number is shifted:  $l \rightarrow l - \Phi/\Phi_0$ . Thus, the resistivity periodically depends on the field and reaches its maximum when the flux through the tube cross-section is a multiple of  $\Phi_0$ .

To take into account both valleys, we have to consider two kinds of cooperons (the electron momenta are measured from the center of the corresponding valley):

$$C_{++} = C_{--} = \begin{array}{c} + \quad + \\ \hline \rightarrow \quad \rightarrow \\ \hline + \quad + \end{array} + \begin{array}{c} + \quad + \\ \hline \rightarrow \quad \rightarrow \\ \hline + \quad + \end{array} + \dots \quad (7)$$

$$= \frac{1}{2\pi v \tau^2 D k^2 - i\omega + (\tau' - \tau)^{-1}}, \quad \omega\tau, \tau D k^2 \ll 1;$$

$$C_{+-} = C_{-+} = \begin{array}{c} + \quad - \\ \hline \rightarrow \quad \rightarrow \\ \hline - \quad + \end{array} + \begin{array}{c} + \quad - \\ \hline \rightarrow \quad \rightarrow \\ \hline - \quad + \end{array} + \dots \quad (8)$$

$$= \frac{1}{4\pi v \tau^2 D k^2 - i\omega}, \quad \omega\tau', \tau' D k^2 \ll 1.$$

Owing to the time reversal invariance, the cooperon propagator coincides with the diffuson propagator and possesses a pole corresponding to the particle number conservation. In the absence of the umklapp processes ( $\tau' \rightarrow \infty$ ), we obtain two poles ( $C_{++}$  and  $C_{--}$ ), which correspond to the conservation of the number of each individual type of electron. The positions of these poles in the reciprocal space are shown in Fig. 2.

The quantum correction takes the form

$$\frac{\Delta\sigma}{\sigma} = -\tau^2 \int \frac{d^2k}{(2\pi)^2} (C_{++} + C_{+-} + C_{-+} + C_{--}). \quad (9)$$

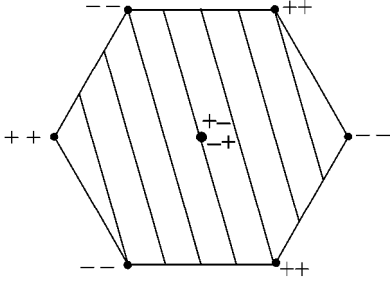


**Fig. 2.** First Brillouin zone for a cooperon. The poles  $C_{++}$  and  $C_{--}$  are at the vertices of the hexagon, and the poles  $C_{+-}$  and  $C_{-+}$  coincide in the center. The lines of the allowed momenta are shown for a (7, 2) tube.

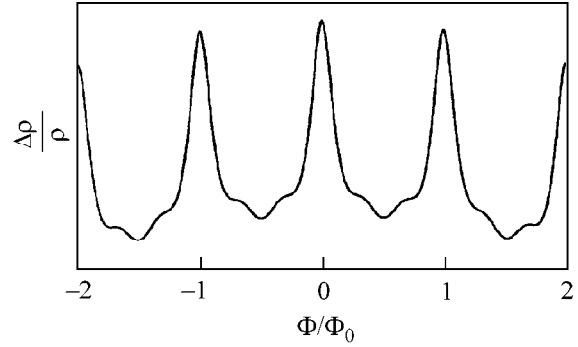


**Fig. 3.** Typical dependence of the resistivity on the magnetic field.  $\tau' = \tau_0 = 2\tau$ ,  $\tau_\phi = 4\tau$ . The scale along the ordinate axis is in arbitrary units.

Substituting the expressions for the cooperon propagators for an  $(n_1, n_2)$  nanotube, we obtain

$$\begin{aligned} \frac{\Delta\sigma}{\sigma} = & -\frac{1}{\pi v} \sum_l \int \frac{dk_{\parallel}}{2\pi} \left\{ \left[ D \left( k_{\parallel}^2 + \frac{l^2}{r^2} \right) + \frac{1}{\tau_{\phi}} \right]^{-1} \right. \\ & + \left[ D \left( k_{\parallel}^2 + \frac{1}{r^2} \left( l + \frac{n_1 + n_2}{3} \right)^2 \right) + \frac{1}{\tau' - \tau} \right]^{-1} \\ & \left. + \left[ D \left( k_{\parallel}^2 + \frac{1}{r^2} \left( l - \frac{n_1 + n_2}{3} \right)^2 \right) + \frac{1}{\tau' - \tau} \right]^{-1} \right\}. \end{aligned} \quad (10)$$

Here, as in Eq. (6), the summation and the integration are performed within the first Brillouin zone (Fig. 2). The dependence on the magnetic field is obtained as above, by replacing  $l$  by  $l - \Phi/\Phi_0$ . In this case, the resistivity also periodically depends on the field with the period  $\Phi_0 = hc/2e$ . However, when  $n_1 + n_2$  is not divisible by three, in addition to the peaks observed at  $\Phi = n\Phi_0$ , new peaks appear at  $\Phi = n\Phi_0/3$ . A typical dependence of the conductivity on the magnetic field is shown in Fig. 3.

These new features are of purely geometric nature, and their magnitude does not depend on temperature, in contrast to the main peak. However, if the intervalley umklapp processes are suppressed ( $\tau' \rightarrow \infty$ ), it is necessary to take into account the term  $\tau_{\phi}^{-1}$  in the denominator of Eq. (7). As a result, the heights of the additional

peaks will depend on temperature and become equal to the main peak height. On the other hand, it is necessary that the conditions of diffusion approximation (8) be satisfied. When  $\tau' = \infty$ , the first term in Eq. (10) will be absent and the electrons of each of the valleys will independently contribute to the magnetoresistance oscillations; these contributions are determined by Eq. (6) but are shifted to one side or another by one-third of the period. For large finite values of  $\tau'$ , the first term in Eq. (10) will have a more complex form, because the higher order terms become significant in the diffusion equation for cooperon.

## REFERENCES

1. S. Iijima, *Nature* **354**, 56 (1991).
2. N. Hamada, D.-I. Sawada, and A. Oshiyama, *Phys. Rev. Lett.* **68**, 1579 (1992).
3. A. Bachtold, C. Strunk, J.-P. Salvetat, *et al.*, *Nature* **397**, 673 (1999).
4. D. Yu. Sharvin and Yu. V. Sharvin, *Pis'ma Zh. Éksp. Teor. Fiz.* **34**, 285 (1981) [*JETP Lett.* **34**, 272 (1981)].
5. B. L. Al'tshuler, A. G. Aronov, and B. Z. Spivak, *Pis'ma Zh. Éksp. Teor. Fiz.* **33**, 101 (1981) [*JETP Lett.* **33**, 94 (1981)].
6. J. Callaway, *Energy Band Theory* (Academic, New York, 1964; Mir, Moscow, 1969).
7. L. P. Gor'kov, A. I. Larkin, and D. E. Khmel'nitskiĭ, *Pis'ma Zh. Éksp. Teor. Fiz.* **30**, 248 (1979) [*JETP Lett.* **30**, 228 (1979)].

*Translated by E. Golyamina*

# Spectra of Random Contractions and Scattering Theory for Discrete-Time Systems<sup>1</sup>

Y. V. Fyodorov and H.-J. Sommers\*

Department of Mathematical Sciences Brunel University, Uxbridge, UB8 3PH, UK

\* Fachbereich Physik, Universität-GH Essen, D-45117 Essen, Germany

Received August 15, 2000; in final form, September 15, 2000

Random contractions (subunitary random matrices) appear naturally when considering quantized chaotic maps within a general theory of open linear stationary systems with discrete time. We analyze statistical properties of complex eigenvalues of generic  $N \times N$  random matrices  $\hat{A}$  of such a type, corresponding to systems with broken time reversal invariance. Deviations from unitarity are characterized by rank  $M \leq N$  and a set of eigenvalues  $0 < T_i \leq 1$ ,  $i = 1, \dots, M$  of the matrix  $\hat{T} = \hat{\mathbf{1}} - \hat{A}^\dagger \hat{A}$ . We solve the problem completely by deriving the joint probability density of  $N$  complex eigenvalues and calculating all  $n$ -point correlation functions. In the limit  $N \gg M$ ,  $n$ , the correlation functions acquire the universal form found earlier for weakly non-Hermitian random matrices. © 2000 MAIK “Nauka/Interperiodica”.

PACS numbers: 03.65.Nk; 05.45.Mt

The theory of wave scattering can be looked at as an integral part of the general theory of linear dynamic open systems in terms of the input–output approach. These ideas and relations were developed in system theory and engineering mathematics many years ago; see papers [1, 2] and references therein. Unfortunately, that development went almost unnoticed by the majority of physicists working in the theory of chaotic quantum scattering and related phenomena; see [3, 4] and references therein. For this reason, we feel it could be useful to recall some basic facts of the input–output approach in such a context.

An Open Linear System is characterized by three Hilbert spaces: the space  $E_0$  of internal states  $\Psi \in E_0$  and two spaces  $E_\pm$  of incoming (–) and outgoing (+) signals or waves, also called input and output spaces, made of vectors  $\phi_\pm \in E_\pm$ . Acting in these three spaces are four operators, or matrices: (a) the so-called fundamental operator  $\hat{A}$ , which maps any vector from internal space  $E_0$  onto some vector from the same space  $E_0$ ; (b) two operators  $\hat{W}_{1,2}$ , with  $\hat{W}_1$  mapping incoming states onto an internal state and  $\hat{W}_2$  mapping internal states onto outgoing states; and (c) an operator  $\hat{S}_0$  acting from  $E_-$  to  $E_+$ .

We will be interested in describing the dynamics  $\Psi(t)$  of an internal state with time  $t$ , provided we know the state at initial instant  $t = 0$  and the system is subject

to a given input signal  $\phi_-(t)$ . In what follows, we consider only the case of the so-called stationary (or *time-invariant*) systems when the operators are assumed to be time-independent. Let us begin with the case of continuous-time description. The requirements of linearity, causality, and stationarity lead to a system of two dynamical equations

$$i \frac{d}{dt} \Psi = \hat{A} \Psi(t) + \hat{W}_1 \phi_-(t) \quad (1)$$

$$\text{and } \phi_+(t) = \hat{S}_0 \phi_-(t) + i \hat{W}_2 \Psi(t).$$

Interpretation of these equations depends on the nature of the state vector  $\Psi$ , as well as of the vectors  $\phi_\pm$ , and is different in different applications. In the context of quantum mechanics, one relates the scalar product  $\Psi^\dagger \Psi$  to the probability of finding a particle inside the “inner” region at time  $t$ , whereas  $\phi_\pm^\dagger \phi_\pm$  stands for the probability currents flowing in and out of the region of internal states (the number of particles coming into or leaving the inner domain per unit time). The condition for particle conservation then reads as

$$\frac{d}{dt} \Psi^\dagger \Psi = \phi_-^\dagger \phi_- - \phi_+^\dagger \phi_+. \quad (2)$$

It is easy to verify that Eq. (2) is compatible with the dynamics equation (1) only if the operators satisfy the following relations:

$$\hat{A}^\dagger - \hat{A} = i \hat{W} \hat{W}^\dagger, \quad \hat{S}_0^\dagger \hat{S}_0 = \hat{\mathbf{1}} \quad \text{and} \quad \hat{W}^\dagger \equiv \hat{W}_2 = -\hat{S}_0 \hat{W}_1^\dagger$$

<sup>1</sup> This article was submitted by the authors in English.

which show, in particular, that  $\hat{A}$  can be written as  $A = \hat{H} - (i/2)\hat{W}\hat{W}^\dagger$ , with a Hermitian  $\hat{H} = \hat{H}^\dagger$ .

The meaning of  $\hat{H}$  is transparent: it governs the evolution  $i(d/dt)\Psi = \hat{H}\Psi(t)$  of an inner state  $\Psi$  when the coupling  $\hat{W}$  between the inner space and input/output spaces is absent. As such, it is just the Hamiltonian describing the closed inner region. The fundamental operator  $\hat{A}$  then has a natural interpretation of the effective non-self-adjoint Hamiltonian describing the decay of the probability from the inner region at zero input signal:  $\phi_-(t) = 0$  for any  $t \geq 0$ . If, however, the input signal is given in the Fourier domain by  $\phi_-(\omega)$ , the output signal is related to it by

$$\begin{aligned} \phi_+(\omega) &= [\hat{S}(\omega)\hat{S}_0]\phi_-(\omega), \\ \hat{S}(\omega) &= \hat{\mathbf{1}} - i\hat{W}^\dagger \frac{1}{\omega\hat{\mathbf{1}} - \hat{A}} \hat{W}, \end{aligned} \quad (3)$$

where we assumed  $\Psi(t=0) = 0$ . The unitary matrix  $\hat{S}(\omega)$  is known in the mathematical literature as the characteristic matrix function of the non-Hermitian operator  $\hat{A}$ . In the present context, it is just the scattering matrix whose unitarity is guaranteed by the conservation law (2).

The contact with the theory of chaotic scattering is now apparent: Eq. (3) was frequently used in the physics literature [3, 4] as a starting point for extracting universal properties of the scattering matrix for a quantum chaotic system within the so-called random matrix approach. The main idea underlying such an approach is to replace the actual Hamiltonian  $\hat{H}$  by a large random matrix and to calculate the ensuing statistics of the scattering matrix. The physical arguments in favor of such a replacement can be found in the cited literature.

In particular, most recently, the statistical properties of complex eigenvalues of the operator  $\hat{A}$  were studied in great detail [4]. These eigenvalues are poles of the scattering matrix and have the physical interpretation of *resonances*—long-lived intermediate states into which discrete energy levels of the closed system are transformed due to coupling to continua.

In the theory presented above, the time  $t$  was a continuous parameter. On the other hand, a very useful instrument in the analysis of classical Hamiltonian systems with chaotic dynamics are the so-called area-preserving chaotic maps [5]. They appear naturally either as a mapping of the Poincaré section onto itself, or as the result of a stroboscopic description of Hamiltonians that are periodic functions of time. Their quantum-mechanical analogues are unitary operators which act on Hilbert spaces of a finite large dimension  $N$ . They are often referred to as evolution, scattering, or Floquet operators, depending on the physical context where

they are used. Their eigenvalues consist of  $N$  points on a unit circle (eigenphases). Numerical studies of various classically chaotic systems suggest that the eigenphases conform statistically quite accurately to the results obtained for unitary random matrices of a particular symmetry (Dyson circular ensembles).

Let us now imagine that a system represented by a chaotic map (“inner world”) is embedded in a larger physical system (“outer world”) in such a way that it describes particles which can come inside the region of chaotic motion and leave it after some time. Models of this type appeared, e.g., in [6], where a kind of scattering theory for “open quantum maps” was developed based on a variant of the Lipmann–Schwinger equation.

On the other hand, in the general system theory [2], dynamical systems with discrete time are considered as frequently as those with continuous time. For linear systems, the “stroboscopic” dynamics is just a linear map  $(\phi_-(n); \Psi(n)) \rightarrow (\phi_+(n); \Psi(n+1))$  which can be generally written as

$$\begin{pmatrix} \Psi(n+1) \\ \phi_+(n) \end{pmatrix} = \hat{V} \begin{pmatrix} \Psi(n) \\ \phi_-(n) \end{pmatrix}, \quad \hat{V} = \begin{pmatrix} \hat{A} & \hat{W}_1 \\ \hat{W}_2 & \hat{S}_0 \end{pmatrix}. \quad (4)$$

Again, we would like to consider a conservative system, and the discrete-time analogue of Eq. (2), in fact, requires the unitarity of the matrix  $\hat{V}$  in Eq. (4). It turns out that such a matrix  $\hat{V}$  can always be conveniently parametrized as (cf. [7])

$$\hat{V} = \begin{pmatrix} \hat{u}\sqrt{1-\hat{\tau}\hat{\tau}^\dagger} & -\hat{u}\hat{\tau} \\ \hat{\tau}^\dagger & \sqrt{1-\hat{\tau}^\dagger\hat{\tau}} \end{pmatrix}, \quad (5)$$

where  $\hat{u}$  is unitary and  $\hat{\tau}$  is a rectangular  $N \times M$  diagonal matrix with entries  $\tau_{ij} = \delta_{ij}\tau_j$ ,  $1 \leq i \leq N$ ,  $1 \leq j \leq M$ ,  $0 \leq \tau_j \leq 1$ . Here, we actually use the freedom to redefine input, output, and internal state by choosing an appropriate basis in the corresponding spaces. This allowed us to bring Eq. (5) to the simplest form suggesting a clear interpretation of the constituents of the model. Indeed, for  $\hat{\tau} = 0$ , the dynamics of the system amount to  $\Psi(n+1) = \hat{u}\Psi(n)$ . We therefore identify  $\hat{u}$  as a unitary evolution operator of the “closed” inner-state domain decoupled from both input and output spaces. Correspondingly,  $\hat{\tau} \neq 0$  just provides a coupling that makes the system open and converts the fundamental operator  $\hat{A} = \hat{u}\sqrt{1-\hat{\tau}\hat{\tau}^\dagger}$  to a contraction,  $1 - \hat{A}^\dagger\hat{A} = \tau\tau^\dagger \geq 0$ . As a result, the equation  $\Psi(n+1) = \hat{A}\Psi(n)$  describes an irreversible decay of any initial state  $\Psi(0)$  for zero input  $\phi_-(n) = 0$ , whereas, for a nonzero input and  $\Psi(0) = 0$ , the Fourier transforms  $\phi_\pm(\omega) =$

$\sum_{n=0}^{\infty} e^{in\omega} \phi_{\pm}(n)$  are related by a unitary scattering matrix  $\hat{S}(\omega)$  given by

$$\hat{S}(\omega) = \sqrt{1 - \hat{\tau}^{\dagger} \hat{\tau}} - \hat{\tau}^{\dagger} \frac{1}{e^{-i\omega} - \hat{A}} \hat{u} \hat{\tau}. \quad (6)$$

Assuming further that the motion outside the inner region is regular, we should be able to describe generic features of open quantized chaotic maps by choosing the matrix  $\hat{u}$  to be a member of a Dyson circular ensemble. Then one finds that  $\hat{\tau}^{\dagger} \hat{\tau} = 1 - |\overline{\hat{S}(\omega)}|^2$ , with the bar standing for the averaging of  $\hat{S}(\omega)$  in Eq. (6) over  $\hat{u}$ . Comparing this result with [3, 4], we see that the  $M$  eigenvalues  $0 \leq T_i \leq 1$  of the  $M \times M$  matrix  $\hat{\tau}^{\dagger} \hat{\tau}$  play the role of the so-called transmission coefficients and describe a particular way in which the chaotic region is coupled to the outer world.

In fact, this line of reasoning is motivated by recent papers [8, 9]. The authors of [8] considered the Floquet description of a Bloch particle in a constant force and periodic driving. After some approximations, the evolution of the system is described by a mapping  $\mathbf{c}_{n+1} = \mathbf{F} \mathbf{c}_n$ , where the unitary Floquet operator  $\mathbf{F} = \hat{S} \hat{U}$  is a product of a unitary “ $M$ -shift”  $\hat{S} : S_{kl} = \delta_{l, k-M}$ ,  $l, k = -\infty, \dots, \infty$  and a unitary matrix  $\hat{U}$ . The latter is effectively of the form  $\hat{U} = \text{diag}(\hat{d}_1, \hat{u}, \hat{d}_2)$ , where  $\hat{d}_{1,2}$  are (semi)infinite diagonal matrices and  $\hat{u}$  can be taken from the ensemble of random  $N \times N$  unitary matrices.

One can check that such dynamics can be easily brought to the standard Eqs. (4) and (5), with the fundamental operator being an  $N \times N$  random matrix of the form  $\hat{A} = \sqrt{1 - \hat{\tau}^{\dagger} \hat{\tau}} \hat{u}$ , and all  $M$  diagonal elements of the  $N \times M$  matrix  $\tau$  are equal to unity. Actually, the original paper [8] employed a slightly different, but equivalent, construction dealing with an “enlarged” internal space of the dimension  $N + M$ . We prefer to follow the general scheme because of its conceptual clarity.

Direct inspection immediately shows that the non-vanishing eigenvalues of the fundamental operator  $\hat{A}$ , as above, coincide with those of an  $(N - M) \times (N - M)$  subblock of the random unitary matrix  $\hat{u}$ . Complex eigenvalues of such “truncations” of random unitary matrices were studied in great detail by the authors of a recent insightful paper [9]. They managed to study eigenvalue correlations analytically for arbitrary  $N, M$ . In particular, they found that, in the limit  $N \rightarrow \infty$  at fixed  $M$ , these correlation functions practically coincide [8] with those obtained earlier [4] for operators of the form  $\hat{A} = \hat{H} - (i/2) \hat{W} \hat{W}^{\dagger}$  occurring in the theory of open systems with continuous-time dynamics.

Such a remarkable universality, though not completely unexpected, deserves to be studied in more detail. In fact, truncated unitary matrices represent only a particular case of random contractions  $\hat{A}$ . Actually, some statistical properties of general subunitary matrices were under investigation recently as a model of a scattering matrix for systems with absorption; see [10].

The particular case of rank-one deviations from unitarity is the simplest one to investigate and was considered in recent preprint [11]. However, generalization to arbitrary  $M$  along the lines of [11] seemed to be problematic. The main goal of this paper is to provide results for the spectra of random contractions for an arbitrary given deviation from unitarity.

The ensemble of general  $N \times N$  random contractions  $\hat{A} = \hat{u} \sqrt{1 - \hat{\tau} \hat{\tau}^{\dagger}}$  describing the chaotic map with broken time reversal symmetry can be described by the following probability measure in the matrix space:

$$\mathcal{P}(\hat{A}) d\hat{A} \propto \delta(\hat{A}^{\dagger} \hat{A} - \hat{G}) d\hat{A}, \quad G \equiv 1 - \hat{\tau} \hat{\tau}^{\dagger}, \quad (7)$$

where  $d\hat{A} = \prod_{ij} d\hat{A}_{ij} dA_{ij}^*$  and we assumed that the unitary matrix  $\hat{u}$  is taken from the Dyson circular unitary ensemble. It is natural to call the  $N \times N$  matrix  $\hat{\tau} \hat{\tau}^{\dagger} = 1 - \hat{G} \geq 0$  the deviation matrix, and we denote it by  $\hat{T}$ . It has  $M$  nonzero eigenvalues coinciding with the transmission coefficients  $T_a$  introduced above. The particular choice  $T_{i \leq M} = 1$ ,  $T_{i > M} = 0$  corresponds to the case considered in [9].

Our first step is, following [4, 9, 11], to introduce the Schur decomposition  $\hat{A} = \hat{U}(\hat{Z} - \hat{R})\hat{U}^{\dagger}$  of the matrix  $\hat{A}$  in terms of a unitary  $\hat{U}$  matrix, a diagonal matrix with the eigenvalues  $\hat{Z}$ , and an upper triangular  $\hat{R}$ . One can satisfy oneself that the eigenvalues  $z_1, \dots, z_N$  are generically not degenerate, provided all  $T_i < 1$ . Then, the measure written in terms of new variables is given by  $d\hat{A} = |\Delta(\{z\})|^2 d\hat{R} d\hat{Z} d\mu(U)$ , where the first factor is just the Vandermonde determinant of eigenvalues  $z_i$  and  $d\mu(U)$  is the invariant measure on the unitary group. The integration over  $\hat{R}$  can be performed with some manipulations using its triangularity (some useful hints can be found in [9]). As the result, we arrive at the joint probability density of all eigenvalues  $\mathcal{P}(\{z\})$  given by

$$\mathcal{P}(\{z\}) \propto |\Delta(\{z\})|^2 \times \int d\mu(U) \prod_{l=1}^N \delta(|z_l|^2 \dots |z_l|^2 - \det[1 - \hat{T} \hat{U} \hat{P}_l \hat{U}^{\dagger}]), \quad (8)$$

where  $\hat{P} = \text{diag}(1, \dots, 1, 0, \dots, 0)$ , with first  $l$  entries being equal to unity, is a projector.

Performing the remaining integration over the unitary group was mentioned as the main technical problem in [11]. Relegating details of the calculation to a more extended publication, we mention that integration can be performed in a recursive way,  $l \rightarrow l + 1$ , with the multiple use of the Itzykson–Zuber–Harish–Chandra [12] formula. After quite an elaborate manipulation, one finally arrives at the following representation:

$$\mathcal{P}(\{z\}) \propto \frac{\det^{M-N}(\hat{T})}{\det(1-\hat{T}) \prod_{\substack{c_1 < c_2 \\ c_1 < c_2}} (T_{c_1} - T_{c_2})} \prod \left( \frac{\partial}{\partial \tau_{c_1}} - \frac{\partial}{\partial \tau_{c_2}} \right) \times \int d\hat{\lambda} e^{-i\text{Tr}\hat{\lambda}} |\Delta(\{z\})|^2 \prod_{k=1}^N f(\ln|z_k|^2, \hat{\lambda}), \quad (9)$$

where we defined the diagonal matrices of size  $M$  as  $\hat{\tau} = \text{diag}(\tau_1, \dots, \tau_M)$ ,  $\hat{\lambda} = \text{diag}(\lambda_1, \dots, \lambda_M)$  and used the notations  $\tau_c = \ln(1 - T_c)$  and

$$f(a, \hat{\lambda}) = i^{M-1} \sum_{q=1}^M \frac{e^{i\lambda_q a}}{\prod_{s(\neq q)} (\lambda_q - \lambda_s)}. \quad (10)$$

The distribution (9) is written for  $|z_k|^2 \leq 1$  for any  $k = 1, \dots, N$  and vanishes otherwise. The remarkable feature of such a distribution is that it allows for calculation of all  $n$ -point correlation functions for arbitrary  $N, n, M$  with help of the method of orthogonal polynomials. Again, the particular case  $M = 1$  [11] is quite instructive and can be recommended to follow first for understanding of the general formulae outlined below.

To this end, we write

$$|\Delta(\{z\})|^2 \prod_{k=1}^N f(\ln|z_k|^2, \hat{\lambda}) = \prod_{k=1}^N N_k(\hat{\lambda}) \det \left[ \sum_{n=1}^N \frac{(z_i z_j^*)^{n-1}}{N_n(\hat{\lambda})} f(\ln|z_j|^2, \hat{\lambda}) \right]_{i,j=1,\dots,N}, \quad (11)$$

where the constants  $N_n(\hat{\lambda})$  are provided by the orthonormality condition

$$\int_{|z|^2 \leq 1} d^2 z z^{m-1} (z^*)^{n-1} f(\ln|z|^2, \hat{\lambda}) = \delta_{m,n} N_n(\hat{\lambda}), \quad (12)$$

which yields, after a simple calculation,

$$N_n(\hat{\lambda}) = \pi \prod_{c=1}^M \frac{1}{(n + i\lambda_c)}.$$

Now, by applying the standard machinery of orthogonal polynomials [13], one can find the correlation function

$$R_n(z_1, \dots, z_n) = \frac{N!}{(N-n)!} \int d^2 z_{n+1} \dots d^2 z_N \mathcal{P}(\{z\}) \quad (13)$$

as given by

$$R_n(z_1, \dots, z_n) \propto \hat{\mathcal{D}} \int d\hat{\lambda} e^{-i\text{Tr}\hat{\lambda}} \times \prod_{k=1}^N N_k(\hat{\lambda}) \det[K(z_i, z_j; \hat{\lambda})]_{(i,j)=1,\dots,n}, \quad (14)$$

where the kernel  $K$  is defined as

$$K(z_1, z_2; \hat{\lambda}) = \frac{1}{\pi} \times \sum_{n=1}^N \det(i\hat{\lambda} + n) (z_1 z_2^*)^{n-1} f(\ln|z_2|^2, \hat{\lambda}) \quad (15)$$

and the differential operator  $\hat{\mathcal{D}}$  is just the expression in front of the  $\hat{\lambda}$ -integral in Eq. (9).

In principle, all  $\lambda$ -integrations in Eq. (14) can be performed explicitly and the resulting formulas provide the desired general solution of the problem. However, for arbitrary  $N, M$ , and  $n$ , the results obtained in that way are still quite cumbersome. We present below, as an example, the lowest correlation function  $R_1(z)$  (which is just the mean eigenvalue density inside the unit circle  $|z| < 1$ ) for the case of all equivalent channels, i.e., when all the transmission coefficients  $T_c$  are equal,  $T_c = T$ . Such a function satisfies the recursive relation

$$R_1^{(M)}(z) = R_1^{(M-1)}(z) + \frac{1}{(M-1)!} \left( \frac{\partial}{\partial t} \right)^{M-1} \mathcal{R}(t, z) \Big|_{t=0}, \quad (16)$$

where the generating function is given by

$$\mathcal{R}(t, z) = \frac{1}{\pi} \frac{\partial}{\partial |z|^2} \frac{\xi^N - \eta^N}{\xi - \eta}$$

and

$$\xi = 1 + (t-1) \left( \frac{1}{|z|^2} - 1 \right) \left( \frac{1}{T} - 1 \right), \quad (17)$$

$$\eta = 1 + (t-1) (1 - |z|^2) \frac{1}{T}.$$

All the above equations are valid for arbitrary  $N \geq M, n$ . In the theory of quantum chaotic scattering, we, however, expect a kind of universality in the semiclassical limit. Translated to the random matrix language, such a limit corresponds to  $N \rightarrow \infty$  at fixed  $n, M$ . Simplifications occur after taking into account that eigenvalues  $z_i$  are, in fact, typically concentrated at distances

of order of  $1/N$  from the unit circle. Then it is natural to introduce new variables  $y_i, \phi_i$  according to  $z_i = (1 - y_i/N)e^{i\phi_i}$  and consider  $y_i$  to be of the order of unity when  $N \rightarrow \infty$ . As to the phases  $\phi_i$ , we expect their typical separation scaling to be  $\phi_i - \phi_j = O(1/N)$ . Performing now explicitly the limit  $N \rightarrow \infty$ , one can bring the correlation function (14), after some lengthy manipulations, to the form

$$R_n(z_1, \dots, z_n) \propto \prod_{k=1}^n \sum_{q=1}^M \frac{e^{-g_q y_k}}{\prod_{s \neq q} (g_q - g_s)} \quad (18)$$

$$\times \det \left[ \int_{-1}^1 d\lambda \prod_{c=1}^M (\lambda + g_c) e^{-\frac{i}{2} \lambda \delta_{ij}} \right]_{i,j=1,n}$$

with  $g_c = 2/T_c - 1$  and  $\delta_{ij} = N(\phi_i - \phi_j) - i(y_i + y_j)$ . The above expression coincides in every detail with that obtained in [4] for random GUE matrices deformed by a finite-rank anti-Hermitian perturbation and thus provides the proof of universality for finite-rank deviations.

This work was supported by the SFB 237 "Unordnung und grosse Fluktuationen" and the INTAS (grant no. 97-1342).

#### REFERENCES

1. M. S. Livsic, *Operators, Oscillations, Waves: Open Systems, Translations of Mathematical Monographs*

(American Mathematical Society, Providence, 1973), Vol. 34.

2. D. Z. Arov, *Sib. Math. J.* **20**, 149 (1979); J. W. Helton, *J. Funct. Anal.* **16**, 15 (1974).
3. C. H. Lewenkopf and H. A. Weidenmüller, *Ann. Phys. (N.Y.)* **212**, 53 (1991).
4. Y. V. Fyodorov and H.-J. Sommers, *J. Math. Phys.* **38**, 1918 (1997); Y. V. Fyodorov and B. A. Khoruzhenko, *Phys. Rev. Lett.* **83**, 65 (1999); H.-J. Sommers, Y. V. Fyodorov, and M. Titov, *J. Phys. A* **32**, L77 (1999).
5. U. Smilansky, in *Supersymmetry and Trace Formulae: Chaos and Disorder*, Ed. by I. V. Lerner *et al.* (Kluwer, New York, 1999), p. 173.
6. F. Borgonovi, I. Guarneri, and D. L. Shepelyansky, *Phys. Rev. A* **43**, 4517 (1991).
7. P. A. Mello and J.-L. Pichard, *J. Phys. I* **1**, 493 (1991).
8. M. Glück, A. R. Kolovski, and H. J. Korsch, *Phys. Rev. E* **60**, 247 (1999).
9. K. Zyczkowski and H.-J. Sommers, *J. Phys. A* **33**, 2045 (2000).
10. E. Kogan, P. A. Mello, and He Liqun, *Phys. Rev. E* **61**, R17 (2000); C. W. J. Beenakker and P. W. Brouwer, *cond-mat/9908325*.
11. Y. V. Fyodorov, nlin.CD/0002034 at xxx.lanl.gov; *Disordered and Complex Systems*, AIP Conf. Proc. (2001) (in press).
12. C. Itzykson and J. B. Zuber, *J. Math. Phys.* **21**, 411 (1980); Harish-Chandra, *Am. J. Math.* **79**, 87 (1957).
13. M. L. Mehta, *Random Matrices* (Academic, London, 1991).

# Anticrossing of Triplet Exciton Levels in Persistence Spectra of GaSe Crystal

A. N. Starukhin, D. K. Nel'son, and B. S. Razbirin

*Ioffe Physicotechnical Institute, Russian Academy of Sciences, Politekhnicheskaya ul. 26,  
St. Petersburg, 194021 Russia*

Received September 18, 2000

The effect of spin sublevel anticrossing in the persistence spectra of triplet excitons was investigated. The anticrossing signal shape was found to change substantially during the excited-state lifetime. The anticrossing signal splits into two peaks, with the separation between them increasing with time. It is shown that each of the peaks is caused by the contribution of one of the interacting states to the emission, and their lifetimes are determined. © 2000 MAIK "Nauka/Interperiodica".

PACS numbers: 71.35.-y; 78.20.Ls; 78.55.Hx

The level anticrossing effect for atomic electronic states was discovered by Eck, Foldy, and Wieder in [1] and since then has found wide spectroscopic use in studying the fine structure of electronic spectra of various systems, from atoms through crystals [2, 3]. This effect arises when a smoothly varying perturbation (e.g., magnetic field) tends to bring the system to level degeneracy (i.e., level crossing), while the other, constant, perturbation removes this degeneracy. The anticrossing signal appears because the properties of the initial states change due to their mixing, which is maximum in the region of the closest approach of energy levels. The merit of the method is that it allows one to gain information on the parameters of the energetically close interacting states under conditions where the corresponding structure in the emission spectra cannot be spectrally resolved because of a relatively large width of emission lines, e.g., owing to inhomogeneous broadening. In particular, such a situation is typical of the fine (spin) structure of exciton states in anisotropic semiconductors.

Under cw excitation, the level anticrossing effect manifests itself as a Lorentz-shaped maximum or minimum in the magnetic-field dependence of the sum of emission intensities of the states of interest [1, 2]. However, our studies of the anticrossing effect in the persistence spectra of bound triplet excitons in GaSe crystals showed that such a simple shape of anticrossing signal is just a particular case corresponding to exciton emission during a short period of time after the excitation.

The purpose of this work was to study the level anticrossing effect at different instants ( $t$ ) of the excited-state lifetime. It is shown that the signal shape undergoes a radical change during the exciton lifetime, from the absence of the signal at  $t \approx 0$  to the appearance of a

Lorentz-shaped peak at intermediate times  $t$  and, finally, to a complex structure consisting of two peaks at larger  $t$ .

The exciton luminescence was excited by the pulses of a copper vapor laser with pulse duration  $\tau_p = 20$  ns. The exciting light with photon energy  $h\nu_{\text{exc}} = 2.144$  eV  $> E_g$  ( $E_g$  is the energy gap of the GaSe crystal) was incident at a small angle to the sample normal, and the luminescence was recorded in the direction of the normal parallel to the optical axis  $c$  of the crystal. The excitation power density was about 200 W/cm<sup>2</sup>. The spectra were recorded by a diffraction spectrometer equipped with a photon counting device with a time resolution of  $\sim 30$  ns. Magnetic fields were generated by a superconducting solenoid.

The emission spectrum of the GaSe crystal in the range of its fundamental absorption edge recorded in the first 30 ns after an exciting pulse is shown in Fig. 1. The shortest wavelength line with a maximum at  $h\nu = 2.108$  eV is caused by the radiative annihilation of free excitons, and the  $\alpha$  and  $\beta$  lines with maxima at 2.096 and 2.089 eV correspond to the emission of triplet excitons bound to the ionized centers (or isoelectronic traps) [4]. The  $\beta$  line has an intense acoustic wing. In the longitudinal magnetic field  $B \geq 2$  T (Faraday geometry  $\mathbf{B} \parallel \mathbf{c} \parallel \mathbf{k}_{\text{photon}}$ ), the lines of the bound excitons split into doublets with right-hand ( $\sigma^+$ ) and left-hand ( $\sigma^-$ ) circular polarizations of the components [4]. At lower fields, the  $\alpha$  and  $\beta$  lines are not resolved because of their relatively large widths. At the same time, under conditions of cw excitation, the dependence of emission intensity of the bound excitons on the longitudinal magnetic field shows a peak [4, 5] caused by the anticrossing of spin sublevels of the triplet excitons in the

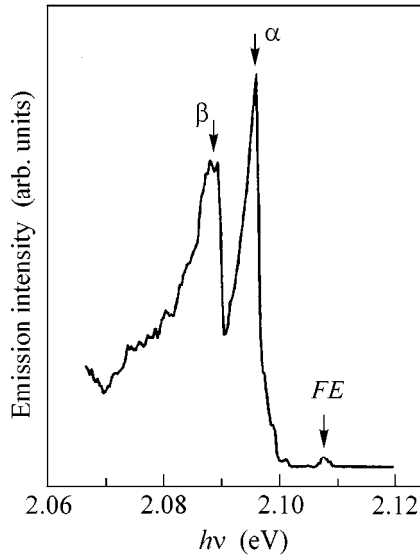


**Fig. 1.** Emission spectrum of a GaSe crystal at  $T = 2$  K.

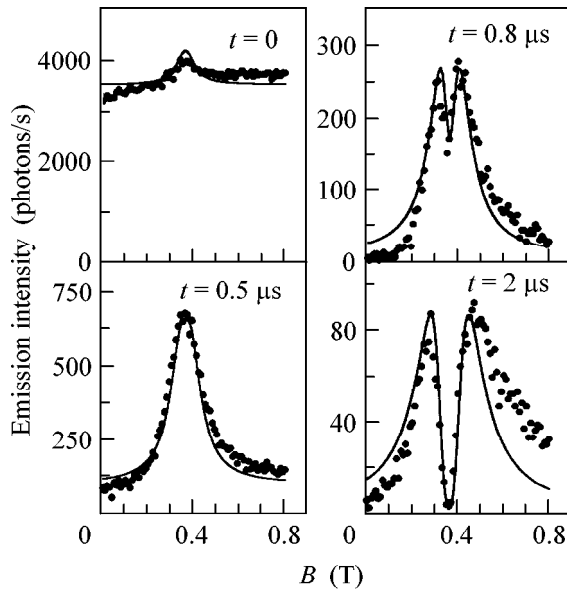


**Fig. 2.** Magnetic-field dependences of the emission intensity  $I_{\sigma^-}(B, t)$  of a bound triplet  $\beta$  exciton with polarization  $\sigma^-$  at different moments of the excited-state lifetime (the time  $t$  is indicated in the panels).  $\mathbf{B} \parallel \mathbf{c} \parallel \mathbf{k}_{\text{photon}}$ . Points are the experimental values, and solid lines are the calculated curves.

magnetic field. Since the character of magneto-optical effects is similar for the  $\alpha$  and  $\beta$  lines, below we restrict ourselves to the behavior of the  $\beta$  line.

The magnetic-field dependences of the transient intensity  $I_{\sigma^-}(B, t)$  of the  $\beta$  line with  $\sigma^-$  polarization in the Faraday geometry is shown in Fig. 2 for different

instants of time  $t$  after excitation. The recording time interval was  $\Delta t = 30$  ns. At  $t = 0$ , a very weak maximum is seen at  $B = 0.36$  T  $\equiv B'_c$  in the  $I_{\sigma^-}(B, 0)$  dependence [for  $\Delta t < 30$  ns,  $I_{\sigma^-}(B, 0)$  is virtually independent of magnetic field].

As the time delay increases in the interval  $0 < t \leq 600$  ns, the relative intensity in the range of the signal maximum sharply increases (the absolute intensity of the  $\beta$  line at  $B = 0$ , naturally, decreases in the persistence spectra) and a well-defined peak is formed in the  $I_{\sigma^-}(B, t)$  curve at  $B = B'_c$  (Fig. 2,  $t = 0.5$   $\mu$ s). In this respect, the  $I_{\sigma^-}(B, t)$  dependence in the indicated time interval is similar to the magnetic-field dependence  $I_{\sigma^-}(B)$  for the  $\beta$  line in the case of cw excitation [4, 5]. On further increase in the time delay, the relative intensity of the peak continues to increase and a shallow dip appears at the peak maximum (Fig. 2,  $t = 0.8$   $\mu$ s). As  $t$  further increases, the dip width and depth increase, and two well-resolved peaks are observed in the  $I_{\sigma^-}(B, t)$  curve, with the peak separation increasing upon further increase in  $t$  (Fig. 2). Therefore, at different moments of the bound exciton lifetime, the shape of the anticrossing signal drastically changes from an almost total absence of the signal (at  $t = 0$ ) to a complex structure with two maxima (at large  $t$ ).

To explain the observed time evolution of the anticrossing signal, let us consider the structure of energy levels for a bound triplet exciton in GaSe. The orbitally nondegenerate  $\Gamma_4$  state of an exciton bound to an ionized center (or isoelectronic trap) in the GaSe crystal, like the free exciton ground state [6], splits into the singlet and triplet states under the action of exchange interaction. The triplet excitons have the total spin  $S = 1$  and spin projections  $S_z = 0, \pm 1$  onto the  $\mathbf{c}$  axis. The transitions to the  $S_z = \pm 1$  states are allowed for the light polarization  $\mathbf{E} \perp \mathbf{c}$ , while the  $S_z = 0$  state is optically inactive [6]. Because of the crystal anisotropy, the state with  $S_z = 0$  is split off by  $\Delta$  from the states with  $S_z = \pm 1$  (see Fig. 3) [7]. The longitudinal magnetic field  $\mathbf{B} \parallel \mathbf{c}$  splits the  $S_z = \pm 1$  level into two  $S_z = -1$  and  $S_z = +1$  sub-levels emitting light with right-hand and left-hand circular polarizations, respectively [6, 7] (Fig. 3). The energies of the triplet exciton states in a longitudinal field are [7]

$$E_{1,2} = E_0 \pm 0.5 g_{zz} \mu_0 B, \quad E_3 = E_0 - \Delta, \quad (1)$$

where  $g_{zz}$  is the exciton  $g$ -factor longitudinal component and  $\mu_0$  is the Bohr magneton. The intensities of radiative transitions from the 1–3 states are determined by their radiative lifetimes  $\tau_r$  (nonzero for the 1 and 2 states) and populations, the latter being dependent on the total exciton lifetimes. In the field  $B = 2\Delta/g_{zz}\mu_0 \equiv B_c$ , the energies of states 2 and 3, according to Eq. (1), become equal; i.e., the corresponding energy levels

intersect. However, in the presence of a perturbation  $V$  (e.g., from the local field of a defect) mixing the exciton states  $|0\rangle$  and  $|\pm 1\rangle$ , the level crossing for the states 2 and 3 is replaced by their anticrossing (Fig. 3). At  $g_{zz}\mu_0 B \approx 2\Delta$ , the 2 and 3 states (i.e., the  $|-1\rangle$  and  $|0\rangle$  states) mainly mix, because the energy difference between these states is much smaller than the energy difference between states 1 and 3. In the presence of perturbation  $V$ , the wave functions  $\Psi_{a,b}$  of the states originating from the states 2 and 3 have the form

$$\Psi_a = C_2\Psi_2 + C_3\Psi_3, \quad \Psi_b = C_3\Psi_2 - C_2\Psi_3, \quad (2)$$

where the coefficients  $C_{2,3}$  depend on the magnetic field. Considering that the state 3 is optically inactive, the radiative transitions from the states  $a$  and  $b$  are polarized similarly to the transition from the 2 state. The amplitudes of the optically active state 2 in wave functions (2) determine the exciton radiative lifetimes for the states  $a$  and  $b$ ,  $\tau_{ar}(B) = [C_2^2(B)\tau_r^{-1}]^{-1}$  and  $\tau_{br}(B) = [C_3^2(B)\tau_r^{-1}]^{-1}$ , and the total exciton lifetimes in these states,  $\tau_a(B) = [\tau_{ar}^{-1}(B) + \tau_0^{-1}]^{-1}$  and  $\tau_b(B) = [\tau_{br}^{-1}(B) + \tau_0^{-1}]^{-1}$ , where  $\tau_0$  is the exciton nonradiative lifetime. For excitation by nonpolarized light with  $h\nu_{\text{exc}} > E_g$  and in the absence of exciton spin relaxation, the intensities  $I_i(B, t)$  ( $i = a$  and  $b$ ) of exciton emission from the states  $a$  and  $b$  can be written as

$$I_i(B, t) = I_0\tau_{ir}^{-1}(B)\exp[-t/\tau_i(B)], \quad (3)$$

where the  $I_0$  value, proportional to the exciton generation rate, is the same for all  $i$ . Since the optical transitions from the states  $a$  and  $b$  are spectrally unresolved, only the total emission

$$I_{\sigma^-}(B, t) = I_a(B, t) + I_b(B, t) \quad (4)$$

is observed in the experiment.

The calculated  $I_{\sigma^-}(B, t)$  dependences for different times  $t$  are shown in Fig. 2 by solid lines. [For the comparison with the experiment to be more correct, the  $I_{\sigma^-}(B, t)$  curves shown in Fig. 2 are the results of averaging over the time intervals from  $t$  to  $t + \Delta t$ ]. The theoretical curves in Fig. 2 are obtained with the following parameters:  $g_{zz} = 3.4$  [4],  $\tau_r = 1.25 \times 10^{-7}$  s,  $\tau_0 = 7 \times 10^{-6}$  s,  $\Delta' = \Delta + V_{22} - V_{33} = 0.0357$  meV, and  $2|V_{23}| = 0.0045$  meV, where  $V_{ik} = \langle \Psi_i | V | \Psi_k \rangle$  ( $i, k = 2$  and  $3$ ). The  $2|V_{23}|$  value is equal to the smallest separation between the  $a$  and  $b$  levels (at  $B = B'_c \equiv 2\Delta'/g_{zz}\mu_0$ ) (Fig. 3). The  $\tau_r$  and  $\tau_0$  values thus obtained can be used to determine the lifetimes of the bound excitons in the initial states 2 and 3:  $\tau_2 = 1.22 \times 10^{-7}$  s and  $\tau_3 = \tau_0 = 7 \times 10^{-6}$  s.

The reasons for the observed time evolution of the anticrossing signal can conveniently be revealed by analyzing the behavior of the individual emission com-

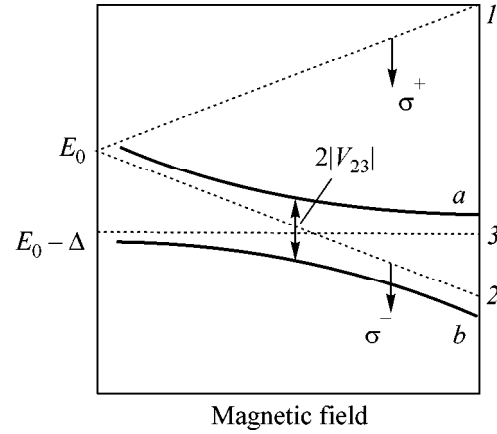


Fig. 3. Scheme of energy levels of a triplet exciton in GaSe in a magnetic field.  $\mathbf{B} \parallel \mathbf{c}$ .

ponents  $I_a(B, t)$  and  $I_b(B, t)$ . The calculations show that, at small  $t$ , the intensity  $I_a(B, t)$  of exciton emission from the state  $a$  first reaches a maximum near  $B \approx B'_c$  and then decreases with a further increase in  $B$ . The behavior of the emission component  $I_b(B, t)$  is similar, but its maximum is reached at a slightly different field strength than for  $I_a(B, t)$ . As a result, the total emission intensity  $I_{\sigma^-}(B, t)$  at not too small  $t$  has a maximum at  $B = B'_c$  (Fig. 2). (In the cw excitation regime, the shape of the anticrossing signal is mostly determined by the exciton emission in this time interval.) As the time delay  $t$  increases, the maximum of the  $I_a(B, t)$  function shifts to higher magnetic fields, whereas the maximum of the  $I_b(B, t)$  function shifts in the opposite direction. As a result, starting from a certain  $B$ , two maxima arise in the  $I_{\sigma^-}(B, t)$  curve, with the relative depth of the minimum at  $B = B'_c$  between them increasing with  $t$ . [The minimum appears because the total lifetime  $\tau_a(B) + \tau_b(B)$  of the excitons in states  $a$  and  $b$  is minimum at  $B = B'_c$ , for which reason both states are depleted in this range of magnetic fields at large  $t$ ]. It should be emphasized that one of the  $I_{\sigma^-}(B, t)$  maxima is dominated by the emission from the  $a$  state and the other corresponds to the emission from the  $b$  state. Therefore, although the radiative transitions from the  $a$  and  $b$  states are spectrally unresolved, the study of the level anticrossing effect at different moments of excited-level lifetime allows one to discriminate between the emissions from the states  $a$  and  $b$ . The analysis of this effect is also helpful in gaining information on the lifetimes of each of the states studied. Note that this effect should be rather general and manifest itself in various atomic systems.

## REFERENCES

1. T. G. Eck, L. L. Foldy, and H. Wieder, *Phys. Rev. Lett.* **10**, 239 (1963).
2. E. B. Aleksandrov, G. I. Khvostenko, and M. P. Chaïka, *Interference of Atomic States* (Nauka, Moscow, 1991).
3. P. G. Baranov, I. V. Mashkov, N. G. Romanov, *et al.*, *Pis'ma Zh. Éksp. Teor. Fiz.* **60**, 429 (1994) [*JETP Lett.* **60**, 445 (1994)].
4. E. M. Gamarts, E. L. Ivchenko, G. E. Pikus, *et al.*, *Fiz. Tverd. Tela (Leningrad)* **24**, 2325 (1982) [*Sov. Phys. Solid State* **24**, 1320 (1982)].
5. B. C. Cavenett, P. Dawson, and K. Morigaki, *J. Phys. C* **12**, L197 (1979).
6. E. Mooser and M. Schlüter, *Nuovo Cimento B* **18**, 164 (1973).
7. E. L. Ivchenko, G. E. Pikus, B. S. Razbirin, and A. N. Starukhin, *Zh. Éksp. Teor. Fiz.* **72**, 2230 (1977) [*Sov. Phys. JETP* **45**, 1172 (1977)].

*Translated by V. Sakun*

# Phonon Laser and Indirect Exciton Dispersion Engineering<sup>1</sup>

Yu. E. Lozovik\* and I. V. Ovchinnikov

Institute of Spectroscopy, Russian Academy of Sciences, Troitsk, 142190 Moscow region, Russia

\* e-mail: lozovik@isan.troitsk.ru

Received September 19, 2000

Engineering of dispersion of indirect excitons by normal electric and in-plane magnetic fields is proposed to be used for controlling the state of many-exciton system (e.g., coherent state) and its photoluminescence and for producing an inverse population in the excitonic system. The possibility of phonon laser creation on the basis of the latter effect is discussed. Phonon number distribution appears to be a fingerprint of that in exciton system. Numerical estimations for the proposed scheme are made for GaAs/AlGaAs quantum wells. © 2000 MAIK "Nauka/Interperiodica".

PACS numbers: 63.20.Dj; 71.35.Ji

Essential success has been achieved now in experiments on coherent states of indirect excitons [1, 2], making a search for different equilibrium phases [3] in the system of indirect excitons and study of their unusual properties [4, 5] promising. Recently, a change in the dispersion of indirect excitons by in-plane magnetic field was experimentally demonstrated in [6].

In this work, we propose a new method of controlling a condensate of indirect excitons in coupled quantum wells by normal electric and parallel magnetic fields. It occurs that, by using external fields, one can essentially control angular dependence and intensity of photoluminescence (PL) of a condensate and, which is of prime interest in this work, create inverse population in the system of excitons (spatially direct and indirect). The latter possibility can be used for the creation of phonon laser, whose frequency can be controlled by the in-plane magnetic field. It occurs that statistics of number of quanta in phonon mode is a "fingerprint" of that for excitons.

In a direct gap semiconductor in coupled quantum wells (CQW), *spatially* direct and indirect excitons (SDE and SIE) are direct in *momentum* space. In case of identical quantum wells (QW), both levels have two-fold degeneracy. For SIE, this is due to two different relative positions of the electron and hole (*e* and *h*) in QWs and, for SDE, to two different locations of the exciton in one of the QWs. SDE is the ground exciton level because of greater Coulomb interaction in the exciton.

Due to spatial separation of *e* and *h*, SIE has electric dipole momentum  $eD$  normal to CQW, where  $D$  is interwell distance. Thus, *moving* SIE has in-plane *magnetic* momentum normal to its velocity  $eDk\hbar/cM$ , where  $k$  is wave vector and  $M$  is effective mass of SIE.

Interaction of SIE electric dipole with normal electric field lowers one of the SIE sublevels as  $eDE/\hbar$  and, in sufficiently strong electric fields, it becomes the ground exciton level. Velocity-selective interaction of magnetic dipole of SIE with in-plane field  $eDk\hbar H/cM$ , being added to quadratic dispersion law of exciton  $\hbar k^2/2M$ , shifts the minimum of dispersion law from radiative zone<sup>2</sup> as  $K_m = eDH/c\hbar$  (e.g., for  $H = 10$  T and  $D = 10$  nm, the shift is  $K_m = 2 \times 10^6$  cm<sup>-1</sup>); this was demonstrated experimentally in [6]. Thus, electric and in-plane magnetic fields normal to CQW control SIE dispersion, while, to the first order in interaction with the fields, dispersion of SDE is unaffected (Fig. 1).

Let normal electric and in-plane magnetic fields initially be such that SIE level is a ground exciton state with the dispersion minimum away from the radiative zone (Fig. 2a). After pump, 2D SIEs gather, at sufficiently low temperatures, near minimum of their dispersion and form "dark" quasi-condensate with slightly fluctuating modulus of order parameter  $\sqrt{n_s}$  ( $n_s$  is "local superfluid density") and short phase order; at lower temperatures, as a result of Kosterlitz–Thouless transition, quasi-long order of phase and global exciton superfluidity must appear. For "dark" state, the process of SIE recombination is a process of the *second* order in interaction with phonon and photon fields through intermediate production of virtual *e-h* pair or exciton in radiative zone (PL frequency after pumping is controlled by normal electric field and is greater than pump frequency).

After that, by swiftly reducing electric field, one can tune the system to the resonance of SIE transformation into *real* SDE with production of an acoustic phonon.

<sup>2</sup> In another approach, this is equivalent to diamagnetic effect, i.e., to opposite electric currents in CQW in parallel magnetic field [4]; see also [7].

<sup>1</sup> This article was submitted by the authors in English.

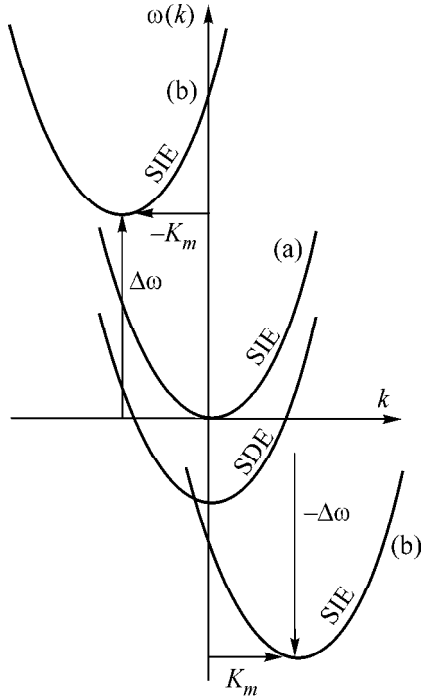


**Fig. 1.** Dispersions of spatially direct and indirect excitons; (a) without external fields; (b) in the presence of in-plane magnetic and normal electric fields,  $K_m = eDH/c\hbar$ ,  $\Delta\omega = eDE/\hbar$ .

This process has the *first* order in interaction with phonon field and its rate is much greater than the rate of SIE recombination before tuning to the resonance. The process of SDE recombination with production of a photon is the second stage of system evolution. For our purposes, it is sufficient to treat this process merely as a decay of SDE level. There are several resonances which are connected with different phonon bands. The first resonance, which is met by reducing electric field, is the one with generation of the lowest energy transverse acoustic phonon among phonon bands.

Excitons in CQW are quasi-2D, unlike 3D phonons and photons, and entire system has 2D in-plane momentum conservation law. Normal component of phonon momentum, which is not fixed by 2D momentum conservation law, is an extra degree of freedom of the system, which gives an additional possibility to conserve energy in the process  $\text{SIE} \rightarrow \text{SDE} + \text{phonon}$ . Thus, 2D momenta of resonant phonons fill continuous area. If initial SIE has  $\omega/|k| < c_v$ , it cannot create a resonant acoustic phonon, because this process is forbidden by conservation laws<sup>3</sup> ( $c_v$  is speed of sound in the medium). In opposite case, SIE with momentum  $K_m$  can produce a phonon with 2D momentum lying in the

<sup>3</sup> Dispersion laws for SDE and SIE are taken in the form  $\omega_D(\mathbf{k}) = \hbar|\mathbf{k}|^2/2M + 1/2k_0c_v$ ,  $k_0 = Mc_v/\hbar$ ,  $\omega_I(\mathbf{k}) = \hbar|\mathbf{k} - \mathbf{K}_m|^2/2M + c_v(K_m + T(E)/2k_0)$ , where  $T(E)$  is a linear function of electric field.

circle  $C: q_x^2 + (K_m - k_0 - q_y)^2 = T(E)$  (axes are oriented as in Fig. 2b). 3D wave vectors of phonons form a prolate ellipsoid of revolution with base  $C$  and ratio of radii  $\sqrt{K_m/k_0}$ .

Analogously, one can easily obtain that, in the first resonance point, photons are emitted as two rays declined to CQW plane and PL intensity abruptly increases. With further decrease in electric field, the rays widen into cones that gradually cover entire spatial angle and PL tends to become isotropic.<sup>4</sup>

To analyze statistical properties of phonon radiation, we will treat quantum fields as single quantum modes. In the interaction representation, the Hamiltonian of the system describing  $\text{SIE} \rightarrow \text{SDE} + \text{phonon}$  is

$$\hat{V} = i\frac{g\hbar}{2}(\hat{I}^\dagger \hat{D} \hat{P} - \hat{I} \hat{D}^\dagger \hat{P}^\dagger).$$

Here  $\hat{I}$ ,  $\hat{D}$ , and  $\hat{P}$  are the annihilation operators for SIE, SDE, and phonon modes and  $g$  is proportional to the transition matrix element.

Initial condition (before tuning the system to the resonance) is the populated SIE mode and the nonpopulated SDE and phonon modes.<sup>5</sup> An equation for density operator of the system is

$$\begin{aligned} \frac{\partial \hat{\rho}}{\partial t} = & -\frac{i}{\hbar}[\hat{V}, \hat{\rho}] + \frac{\gamma_P}{2}(2\hat{P}\hat{\rho}\hat{P}^\dagger - \hat{P}^\dagger\hat{P}\hat{\rho} - \hat{\rho}\hat{P}^\dagger\hat{P}) \\ & + \frac{\gamma_D}{2}(2\hat{D}\hat{\rho}\hat{D}^\dagger - \hat{D}^\dagger\hat{D}\hat{\rho} - \hat{\rho}\hat{D}^\dagger\hat{D}). \end{aligned} \quad (1)$$

Here,  $\gamma$  are decay rates of corresponding particles. We neglected decay processes of SIE, because SIE recombination has tunneling character due to spatially separated  $e$  and  $h$  and, thus,  $\gamma_D \gg \gamma_I$ . We use positive  $P$ -representation [9] of density operator:

$$\begin{aligned} \rho = & \int d^2\mathbf{x} \frac{\Theta(\mathbf{x})}{\langle \alpha_1, \beta_1, \xi_1 | \alpha_2^*, \beta_2^*, \xi_2^* \rangle} \\ & \times |\alpha_1, \beta_1, \xi_1\rangle \langle \alpha_2^*, \beta_2^*, \xi_2^*|, \\ |\alpha, \beta, \xi\rangle = & |\alpha\rangle_P |\beta\rangle_I |\xi\rangle_D, \\ \mathbf{x} = & (\alpha_1, \alpha_2, \beta_1, \beta_2, \xi_1, \xi_2), \end{aligned}$$

$$d^2\mathbf{x} = \prod_i d(\text{Re}(\mathbf{x}_i))d(\text{Im}(\mathbf{x}_i)),$$

where  $|\mathbf{x}\rangle_{P(I, D)}$  is a coherent state of phonon (SIE, SDE) field with eigenvalue  $x$  of operator  $\hat{P}(\hat{I}, \hat{D})$ . Positive

<sup>4</sup> Details will be published elsewhere.

<sup>5</sup> We analyze pulse photon laser. Stationary generating photon laser will be described elsewhere. See also [8].

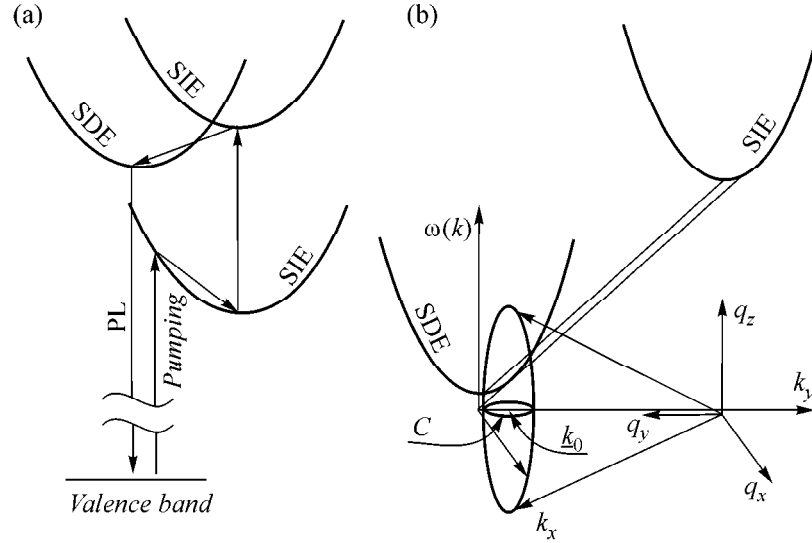


**Fig. 2.** (a) Time evolution of exciton population in the proposed scheme and (b) graphical representation of 2D momentum and energy conservation laws after tuning the system to the SIE  $\rightarrow$  SDE + phonon resonance.

$P$ -representation is convenient for evaluating normally ordered products of operators:

$$\langle (\hat{P}^\dagger)^i (\hat{I}^\dagger)^j (\hat{D}^\dagger)^k \hat{P}^l \hat{I}^m \hat{D}^n \rangle = \int d^2 \mathbf{x} \Theta(\mathbf{x}) \alpha_2^i \beta_2^j \xi_2^k \alpha_1^l \beta_1^m \xi_1^n = \overline{\alpha_2^i \beta_2^j \xi_2^k \alpha_1^l \beta_1^m \xi_1^n}.$$

Equivalent to (1) way of describing the time evolution of the system is analysis of the infinite number of equations for average values:

$$\begin{aligned} \frac{\partial}{\partial t} \overline{\prod_{k=1}^n x_{j_k}} &= \sum_{k=1}^n \overline{A_{j_k}(x)} \prod_{l=1, l \neq k}^n x_{j_l} \\ &+ \frac{1}{2} \sum_{k, l=1, k > l}^n \overline{(D_{j_k, j_l} + D_{j_l, j_k})} \prod_{m=1, m \neq k, l}^n x_{j_m}, \\ A_{\alpha_1} &= \xi_2 \beta_1 - \lambda_p \alpha_1, \quad A_{\alpha_2} = \xi_1 \beta_2 - \lambda_p \alpha_2, \\ A_{\xi_1} &= \alpha_2 \beta_1 - \lambda_D \xi_1, \quad A_{\xi_2} = \alpha_1 \beta_2 - \lambda_D \xi_2, \\ A_{\beta_1} &= -\alpha_1 \xi_1, \quad A_{\beta_2} = -\alpha_2 \xi_2, \\ D_{\alpha_1, \xi_1} &= D_{\xi_1, \alpha_1} = \beta_1, \quad D_{\alpha_2, \xi_2} = D_{\xi_2, \alpha_2} = \beta_2. \end{aligned} \quad (2)$$

Here, we used the substitution  $(g/2)t \rightarrow t$  and  $\lambda_{p,D} = \gamma_{p,D}/g$ . In real semiconductors (e.g., GaAs), the rate of SIE  $\rightarrow$  SDE + phonon transition, as well as the rate of recombination of SDE with photon generation, is much greater than the rate of phonon attenuation in the medium. Thus, we have  $\lambda_p \ll 1, \lambda_D$ .

One can show using Eq. (2) that averages with different powers of  $\alpha_1$  and  $\alpha_2$  or  $\xi_1$  and  $\xi_2$  (in other words,

phonon and SDE phase-dependent averages) depend only on the averages of the same type. All of them initially equal zero and, thus, they remain zero for all times, irrespective of whether the emitter has the phase properties or not. This is due to that phonons and SDEs share phase of SIE system (it exists only at  $T = 0$ ), and independently they have no definite phases.

Using Eq. (2), one can get the equations describing time evolution of populations of the modes:

$$\frac{\partial}{\partial t} N_p(t) = C(t) - 2\lambda_p N_p(t),$$

$$\frac{\partial}{\partial t} N_l(t) = -C(t),$$

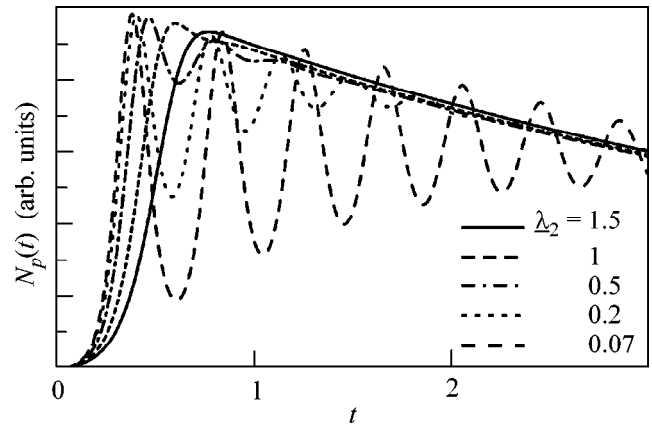


**Fig. 3.** Time evolution of phonon mode population for different values of  $\lambda_D = \lambda_D / \sqrt{N_l(0)}$ ;  $\lambda_p = 0.1$ .

$$\begin{aligned}\frac{\partial}{\partial t}N_D(t) &= C(t) - 2\lambda_D N_D, \\ \frac{\partial}{\partial t}C(t) &= 2(N_P(t)N_I(t) + N_D(t)N_I(t) \\ &\quad - N_P(t)N_D(t) + N_I(t)) - (\lambda_P + \lambda_D)C(t), \\ N_P(t) &= \overline{\alpha_1\alpha_2}, \quad N_I(t) = \overline{\beta_1\beta_2}, \\ N_D(t) &= \overline{\xi_1\xi_2}, \quad C(t) = \overline{(\alpha_1\beta_2\xi_1 + \alpha_2\beta_1\xi_2)}.\end{aligned}$$

We factorized four variable averages to obtain a closed system of equations. The solution to these equations (Fig. 3) shows that populations of SDE and SIE modes fade in times  $\approx \lambda_D^{-1}$  and population of phonon mode fades in times  $\approx \lambda_P^{-1}$ . The populations have or have not oscillating character (i.e., the effect of SIE  $\rightarrow$  SDE + photon quantum beats) with respect to whether parameter  $\lambda_2$  is greater or smaller than  $\sqrt{N_I(0)}$  (for  $N_I(0) \gg 1$ ).

When  $\lambda_P^{-1} \gg t \gg \lambda_D^{-1}$ , all quanta, initially in SIE mode, are transmitted into phonon mode, but the effect of phonon mode decay is negligible. For such times, one can omit in Eq. (2) terms proportional to  $\lambda_P$ . In such cases, the averages  $\overline{(\alpha_1\alpha_2 + \beta_1\beta_2)^n}$  are the integrals of time evolution. All averages including  $\beta_1, \beta_2$  are zero, so that

$$\left\langle (\hat{P}^\dagger(t))^n (\hat{P}(t))^n \right\rangle_{\lambda_P^{-1} \gg t \gg \lambda_D^{-1}} = \left\langle (\hat{I}^\dagger(0))^n (\hat{I}(0))^n \right\rangle, \quad (3)$$

$$n = 1, 2, \dots$$

Phonon radiation with laser properties, i.e., low-intensity fluctuations, can be viewed as quantum mode with populated Goldstone mode that is connected with phase fluctuations. Plotted as a function of variables  $\hat{X}_1 = 2^{-1/2}(\hat{P}^\dagger + \hat{P})$ ,  $\hat{X}_2 = -i2^{-1/2}(\hat{P}^\dagger - \hat{P})$ , such a population is annular with center (0, 0) and radius  $\sim \sqrt{N_P}$ . This can be characterized by relative dispersion of number of quanta in the mode:

$$v(\hat{P}^\dagger(t)\hat{P}(t)) = \frac{g^{(2)}(t) - N_P(t) - N_P(t)^2}{N_P(t)^2}.$$

Here,  $g^{(2)}(t) = \left\langle \hat{P}^\dagger(t)\hat{P}^\dagger(t)\hat{P}(t)\hat{P}(t) \right\rangle$  is second-order correlation function;  $N_P$  and  $g^{(2)}$  can be experimentally observed by measurements with, correspondingly, one (intensity measurements) and two (Hunbury–Brown–Twiss-like measurements) detectors.

At sufficiently low temperatures, SIEs have low  $n_s$  fluctuations and  $v(\hat{I}^\dagger(0)\hat{I}(0)) \ll 1$ . The lower the temperature the smaller the parameter  $v(\hat{I}^\dagger(0)\hat{I}(0))$  and,

therefore, the lower the intensity fluctuations of phonon radiation.

Initial number of SIE is  $\rho S$ , where  $S$  is the area of CQW, and they are shared by  $V_q SL_z / (2\pi)^3$  phonon quantum states, where  $L_z$  is the width of the sample in  $z$ -direction and  $V_q$  is momentum space area that phonons occupy;  $V_q$  characterizes one-phonon space coherence that determines possible interference pattern between two points of phonon radiation. This is determined by the spread of SIE ( $k_I$ ) and widths of the SIE and SDE levels. The smallest value of  $V_q$  corresponds to  $T(E) = k_0^2 + M(\gamma_I + \gamma_D)/\hbar$  and can be easily estimated from simple geometrical analysis (Fig. 2) as  $\sqrt{K_m/k_0}((k_I + k_0)^2 + 2M(\gamma_I + \gamma_D)/\hbar)^{3/2} \approx 10^{15} \text{ cm}^{-1}$ , where we took  $\gamma_D + \gamma_I \approx 10^{10} \text{ s}^{-1}$  and  $k_I \approx 10^5 \text{ cm}^{-1}$ ;  $k_I$  is mainly determined by inter-SIE dipole–dipole repulsion and can be given for estimation as  $\sqrt{U(0)\rho M/\hbar}$ , where  $U(0)$  is zero-Fourier component of the potential. Although the Kosterlitz–Thouless transition does not directly affect phonon radiation statistics, it increases the number of quanta in each phonon quantum mode by reducing the initial SIE momentum spread.

An additional condition for the phonon radiation to have laser properties is a great number of quanta in each quantum state of phonon field and, thus, the following inequality must be true:

$$L_z \ll \rho(2\pi)^3/V_q \approx 10^{-4-5} \text{ cm}. \quad (4)$$

This restriction on  $L_z$  value appeared because phonons and SIE have different dimensionalities. For convenience, we propose to use a heterostructure consisting of many CQWs. In such case, the distance between CQW must satisfy condition (4) for  $L_z$ .

At high temperatures, the source of phonon radiation—SIEs—has no low  $n_s$  fluctuations and the phonon mode is just a chaotic state that can be called the phonon avalanche.

In summary, we proposed to use SIE dispersion engineering for controlling many-exciton state and phonon laser design. Analyzing phonon radiation statistics in the proposed scheme, we obtain that phonon radiation can be viewed as a laser one in case of low temperatures and when condition (4) is fulfilled.

This work was supported by the INTAS and the Russian Foundation for Basic Research.

## REFERENCES

1. L. V. Butov and A. I. Filin, Phys. Rev. B **58**, 1980 (1998).
2. A. V. Larionov, V. B. Timofeev, J. Hvam, and C. Soerensen, Pis'ma Zh. Éksp. Teor. Fiz. **71**, 174 (2000) [JETP Lett. **71**, 117 (2000)].
3. Yu. E. Lozovik and O. L. Berman, Zh. Éksp. Teor. Fiz. **91**, 526 (1996) [JETP Lett. **64**, 573 (1996)]; Zh. Éksp. Teor. Fiz. **111**, 1879 (1997) [JETP **84**, 1027 (1997)];

- Yu. E. Lozovik, O. L. Berman, and V. G. Tsvetus, *Phys. Rev. B* **59**, 5627 (1999); I. V. Lerner and Yu. E. Lozovik, *Zh. Éksp. Teor. Fiz.* **80**, 1488 (1981) [*Sov. Phys. JETP* **53**, 763 (1981)]; D. Yoshioka and A. H. MacDonald, *J. Phys. Soc. Jpn.* **59**, 4211 (1990); J. B. Stark, W. H. Knox, D. S. Chemla, *et al.*, *Phys. Rev. Lett.* **65**, 3033 (1990); X. M. Chen and J. J. Quinn, *Phys. Rev. Lett.* **67**, 895 (1991); S. Conti, G. Vignale, and A. H. MacDonald, *Phys. Rev. B* **57**, R6846 (1998).
4. Yu. E. Lozovik and A. V. Poushnov, *Phys. Lett. A* **228**, 399 (1997); Yu. E. Lozovik and V. I. Yudson, *Zh. Éksp. Teor. Fiz.* **71**, 738 (1976) [*Sov. Phys. JETP* **44**, 389 (1976)]; *Solid State Commun.* **18**, 628 (1976).
  5. A. V. Klyuchnik and Yu. E. Lozovik, *Zh. Éksp. Teor. Fiz.* **76**, 670 (1979) [*Sov. Phys. JETP* **49**, 335 (1979)]; J. Low Temp. Phys. **38**, 761 (1980); S. I. Shevchenko, *Phys. Rev. Lett.* **72**, 3242 (1994).
  6. L. V. Butov, A. V. Mintsev, Yu. E. Lozovik, *et al.*, *Phys. Rev. B* **62**, 1548 (2000).
  7. A. A. Gorbatsevich and I. V. Tokatly, *Semicond. Sci. Technol.* **13**, 288 (1998).
  8. I. V. Volkov, S. T. Zavtrak, and I. S. Kuten, *Phys. Rev. E* **56**, 1097 (1997); S. S. Makler, I. Camps, J. Weberszpil, and D. E. Tuiyart, *J. Phys.: Condens. Matter* **12**, 3149 (2000); A. A. Zadernovskii and L. A. Rivlin, *Kvantovaya Élektron. (Moscow)* **20**, 353 (1993).
  9. P. D. Drummond and C. W. Gardiner, *J. Phys. A* **13**, 2353 (1980).

# Magnetic-Field-Induced Spin-Reorientational Transition in $\text{TbMn}_6\text{Sn}_6$

N. K. Zaïkov\*, A. N. Pirogov, N. V. Mushnikov, A. E. Teplykh,  
É. Z. Valiev, and Yu. A. Dorofeev

*Institute of Metal Physics, Ural Division, Russian Academy of Sciences,  
ul. S. Kovalevskoi 18, Yekaterinburg, 620002 Russia*

\* e-mail: [zajkov@imp.uran.ru](mailto:zajkov@imp.uran.ru)

Received September 20, 2000

Magnetic state of the intermetallic  $\text{TbMn}_6\text{Sn}_6$  compound was studied by neutron diffraction analysis in external magnetic fields of  $H = 0, 4,$  and  $5$  kOe. Magnetic moments and their orientations were determined for the Tb and Mn sublattices. Magnetic fields higher than  $4$  kOe were shown to induce spin-reorientational transition at room temperature from the  $c$  axis to the basal plane. © 2000 MAIK “Nauka/Interperiodica”.

PACS numbers: 75.25.+z, 75.30.Kz

An external magnetic field, when applied to single-crystal samples of ferro- and ferrimagnets along their hard magnetic axes, induces either smooth or jumpwise, in a certain critical field, rotation of the magnetization vector toward the field direction. The jump processes were called the first-order magnetization processes (FOMP) [1]. They are observed, e.g., in  $\text{Nd}_2\text{Fe}_{14}\text{B}$  [2],  $\text{Pr}_2(\text{Co}_{1-x}\text{Fe}_x)_{17}$  [3], and in some other rare-earth and  $3d$ -metal compounds. The available information on the FOMP was gained, as a rule, by magnetic measurements and, thus, it provides only indirect data on the behavior of the individual (rare-earth and  $3d$ -transition) magnetic sublattices. So far, neutron diffraction studies of FOMPs have not been carried out because these processes, as a rule, require high magnetic fields. We have recently shown [4] that the FOMP in the  $\text{TbMn}_6\text{Sn}_6$  intermetallic compound occurs at room temperature in a relatively weak magnetic field ( $\sim 4$  kOe). This compound has the  $\text{HfFe}_6\text{Ge}_6$ -type hexagonal structure (space group  $P6/mmm$ ). Magnetic moments of the Tb and Mn sublattices are coupled by a strong negative exchange interaction and undergo simultaneous ordering at Curie temperature  $T_C = 423$  K [5]. In the range  $305$ – $350$  K, the magnetic moments of Tb and Mn are spontaneously reoriented from the  $c$  axis to the basal plane [6].

A magnetic-field-induced jumpwise change in the magnetization of  $\text{TbMn}_6\text{Sn}_6$  was observed by J. Hu *et al.* in [7]. These authors conjectured that such behavior of magnetization is indicative of the occurrence of either the spin-flop or metamagnetic transition. However, more recent measurements with a single-crystal sample [8] showed that the magnetization jump occurs only upon magnetization along the hard magnetic axis ( $a$  axis) and not upon magnetization along the easy

magnetic axis ( $c$  axis). According to [8], this is evidence for the spin reorientation of the “axis–plane” type.

In this work, the FOMP in  $\text{TbMn}_6\text{Sn}_6$  was studied by neutron diffraction analysis and the behavior of the Tb and Mn sublattices at the spin-reorientational transition (SRT) induced by the external magnetic field was examined.

The  $\text{TbMn}_6\text{Sn}_6$  alloy was smelted from the initial high-purity components in an induction furnace in  $\text{Al}_2\text{O}_3$  crucibles under an argon atmosphere. The homogenizing annealing of the alloy was carried out at  $800^\circ\text{C}$  under argon for 10 days. The X-ray patterns of a polycrystalline  $\text{TbMn}_6\text{Sn}_6$  sample show, in addition to the lines of the main  $\text{HfFe}_6\text{Ge}_6$ -type phase, weak reflections from a foreign phase. Measurements of the initial magnetic susceptibility in an alternating magnetic field showed that  $T_C$  of the main phase was equal to  $419$  K and the spin-reorientation temperature was  $306$  K, in accordance with [5, 6]. The foreign phase was not magnetically ordered above  $25$  K, and, hence, it could not give rise to anomalies in the magnetization curve at room temperature. A powder of the  $\text{TbMn}_6\text{Sn}_6$  compound with an average particle size of  $\sim 200$   $\mu\text{m}$  was oriented in an external magnetic field of  $5$  kOe at room temperature in epoxy resin.

The neutron diffraction measurements were performed on D-2 and D-3 diffractometers of the IVV-M reactor (Zarechyi, Sverdlovsk region) with neutron wavelengths of  $1.805$  and  $2.432$  Å. A polycrystalline unoriented sample was measured on a D-3 diffractometer, and an oriented sample, on a D-2 instrument. All measurements were made at room temperature ( $293$  K). The neutron diffraction patterns were processed using the “Fullproof” program.

The results of measuring the magnetization of the oriented  $\text{TbMn}_6\text{Sn}_6$  sample in an external magnetic

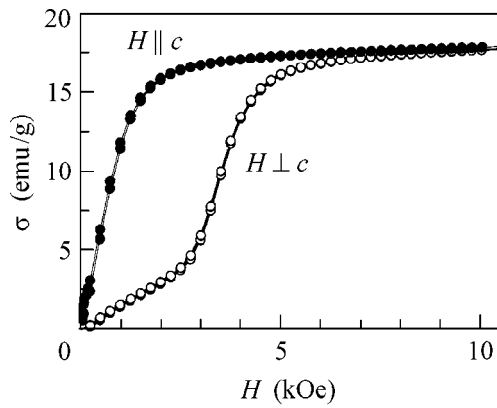


**Fig. 1.** Magnetization curves measured for the oriented  $\text{TbMn}_6\text{Sn}_6$  sample in magnetic fields (●) parallel and (○) perpendicular to the orientation direction ( $T = 293$  K).

field (Fig. 1) are consistent with the single-crystal data [8]. One can see from Fig. 1 that the magnetization jump occurs at room temperature even in fields of about 3.5 kOe. It is shown in [4] that this jump is associated with the FOMP and arises because of a relatively large magnetocrystalline anisotropy constant  $K_2$ . It is comparable in magnitude and opposite in sign to  $K_1$ .

The neutron diffraction patterns of the unoriented  $\text{TbMn}_6\text{Sn}_6$  sample measured in magnetic fields  $H = 0$ , 4, and 5 kOe are shown in Fig. 2. It is seen from Fig. 2 that the intensity of the (001) reflection markedly increases with a rise in magnetic field. The intensities of other (00 $l$ ) reflections also increase, though to a lesser extent. Since the intensities of the magnetic reflections (00 $l$ ) should increase with increasing magnetization projection onto the basal plane, one can conclude that the external field induces rotation of the magnetic moments of Tb and Mn from the  $c$  axis to the basal plane.

To determine more correctly how the magnetization orientation depends on the direction of the external field, the neutron diffraction measurements were carried out for the oriented  $\text{TbMn}_6\text{Sn}_6$  sample. The neutron scans recorded for the oriented  $\text{TbMn}_6\text{Sn}_6$  sample in a  $\Omega$ - $2\theta$  mode are shown in Fig. 3. The data were collected for two directions of external field ( $H = 5$  kOe), parallel and perpendicular to the orientation of the sample particles (to the  $c$  axis in our case). One can see from Fig. 3 that, if the external field is perpendicular to the  $c$  axis, then magnetic reflection (001) appears. If the field is aligned with the  $c$  axis, this reflection is absent. This provides evidence that, contrary to the situation

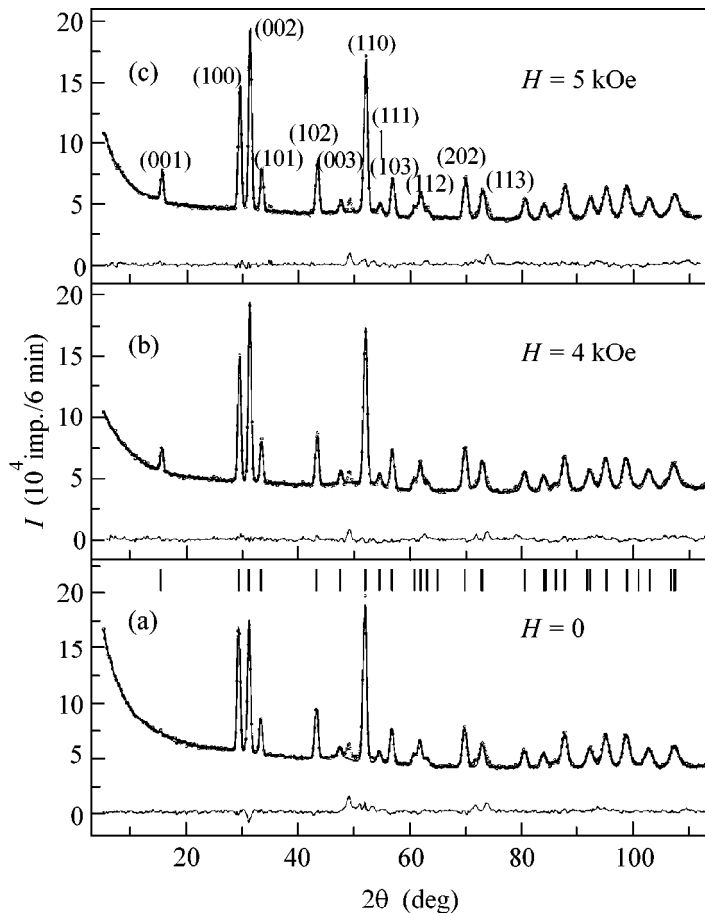


**Fig. 2.** Neutron diffraction patterns of the unoriented  $\text{TbMn}_6\text{Sn}_6$  sample in magnetic fields 0, 4, and 5 kOe at 293 K.

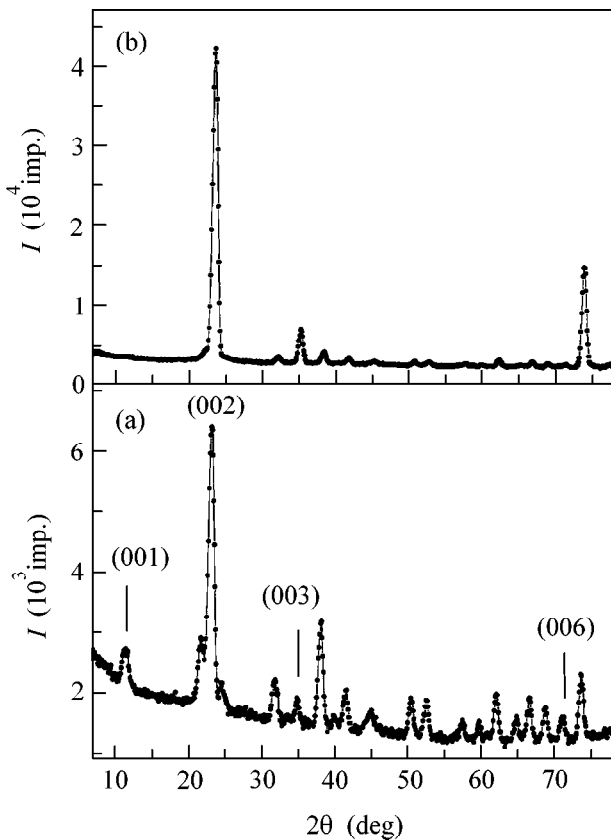


**Fig. 3.** Neutron diffraction patterns of the oriented  $\text{TbMn}_6\text{Sn}_6$  sample in magnetic fields (a) perpendicular and (b) parallel to the orientation direction ( $H = 5$  kOe).

with  $H \parallel c$ , a large projection of magnetic moment appears on the basal plane in the magnetic field  $H \perp c$ . This is in complete agreement with the data [4, 8] about the occurrence of the SRT from the  $c$  axis to the basal plane.

The measured magnetic moments of the Tb and Mn sublattices and the angles they form with the  $c$  axis are presented in the table for the unoriented sample and

Magnetic moments of the Tb and Mn sublattices and the angles they form with the  $c$  axis for three values of the external magnetic field

Atom	$\mu, \mu_B/\text{f.u.}$	$\theta, \text{deg}$
$H = 0$		
Tb	5.2(1)	7(1)
Mn	1.89(8)	7(1)
$H = 4$ kOe		
Tb	5.8(2)	44(3)
Mn	2.1(1)	37(5)
$H = 5$ kOe		
Tb	5.9(1)	51(3)
Mn	2.1(1)	37(5)

three values of the external field. The average moments of the Tb and Mn sublattices and the angle ( $7^\circ$ ) they form with the  $c$  axis in zero field agree well with the data obtained in [6]. It is seen from the table that, in the presence of an external field, the magnetic moments of the sublattices deviate by  $40^\circ$  from the  $c$  axis to the basal plane. The magnetic moments of both sublattices slightly increase in the field. This is likely favored by the ordering effect of the external field on the magnetic moments of the Mn ions, because they are oriented along the field. Due to the strong intersublattice exchange, the magnetic moment of the Tb sublattice also grows. Unfortunately, this is difficult to verify by the magnetic measurements, because the magnetic moments of the sublattices may increase in such a fashion that the mean magnetic moment per formula unit remains unchanged.

As we already pointed out in [4], our speculations on the origins of the observed SRT are based on the assumption that the sublattices are coupled by a strong intersublattice exchange, leading to their collinearity. It is seen from the table that, to within experimental accuracy, this assumption is valid.

In summary, neutron diffraction measurements were carried out for oriented and unoriented polycrystalline  $\text{TbMn}_6\text{Sn}_6$  samples to study the first-order spin-reorientational transition induced by an external magnetic field. Zero-field measurements and measurements in external magnetic fields of 4 and 5 kOe indicate that a relatively weak external field induces the SRT at room temperature from the  $c$  axis to the basal plane. The magnetic moments of the Tb and Mn sublattices and the angles they form with the  $c$  axis are obtained for different values of external magnetic field.

This work was supported by the Russian Foundation for Basic Research (project no. 98-02-16165) and the program "Neutron Studies of Materials" (project no. 4). We are grateful to A.K. Shtolz and E.G. Gerasimov for certifying the sample.

## REFERENCES

1. G. Asti and F. Bolzoni, *J. Magn. Magn. Mater.* **20**, 29 (1980).
2. F. Bolzoni, O. Moze, and L. Pareti, *J. Appl. Phys.* **62**, 615 (1987).
3. D. Melville, W. I. Khan, and S. Rinaldi, *IEEE Trans. Magn.* **12**, 1012 (1976).
4. N. K. Zajkov, N. V. Mushnikov, M. I. Bartashevich, and T. Goto, *J. Alloys Compd.* **309**, 26 (2000).
5. G. Venturini, B. Chafik, El. Idrissi, *et al.*, *J. Magn. Magn. Mater.* **94**, 35 (1991).
6. B. Malaman, G. Venturini, R. Welter, *et al.*, *J. Magn. Magn. Mater.* **202**, 519 (1999).
7. J. Hu, K. Wang, B. Hu, *et al.*, *J. Phys.: Condens. Matter* **7**, 889 (1995).
8. D. M. Clatterbuck and K. A. Gschneidner, Jr., *J. Magn. Magn. Mater.* **207**, 78 (1999).

*Translated by V. Sakun*

# Vertex Functions as a Factor of Enhancing Electron–Electron Attraction in $d$ -Wave Channel of the “Coulomb” Superconductivity Mechanism

É. A. Pashitskii and V. I. Pentegov

*Institute of Physics, National Academy of Sciences of Ukraine, pr. Nauki 46, Kiev, 03022 Ukraine*

Received September 7, 2000; in final form, September 22, 2000

It is shown that many-particle Coulomb correlations described by Coulomb vertex functions  $\Gamma_c$  in layered high- $T_c$  superconducting metal oxide cuprates substantially enhance effective electron–electron attraction in the  $d$ -wave Cooper-pairing channel. This attraction is due to the combined action of a strong in-layer anisotropy of the quasi-two-dimensional electronic spectrum and the suppression of a screened Coulomb repulsion for small transferred momenta in small-angle charge-carrier scattering from long-wavelength charge-density fluctuations. Such a “Coulomb” mechanism of anisotropic Cooper pairing may provide high superconducting transition critical temperatures ( $T_c \geq 100$  K) for optimum-doped cuprates. © 2000 MAIK “Nauka/Interperiodica”.

PACS numbers: 74.20.-z, 74.72.-h

**1.** One of the characteristic features of high- $T_c$  superconductors (HTSC) based on layered metal oxide (MO) cuprates is the experimentally observed  $d_{x^2-y^2}$  symmetry of the superconducting order parameter [1–3]. The possibility for a superconducting gap of such symmetry to occur in HTSC was discussed in [4] within the framework of the site representation of the Hubbard model and, more recently, in [5–7], where a model of a near-antiferromagnetic quasi-two-dimensional Fermi liquid with strong spin correlations was considered. However, apart from the exchange (spin-fluctuation) channel, a direct Coulomb (charge-fluctuation) channel of electron–electron interactions may occur, which was disregarded in [4–7].

In [8, 9], it was shown by the random-phase approximation calculations that the extended saddle-point singularities (SPSs) in the quasi-two-dimensional band spectrum of layered MO cuprates [10, 11] cause a strong anisotropy of the effective mass and the group velocity of quasiparticles near the Fermi surface and may be responsible for the appearance of heavily damped long-wavelength low-frequency electron-density excitations with an acoustic-type dispersion law ( $\omega_q \propto q$  at  $q \rightarrow 0$ ) in the collective electronic spectrum. These excitations are analogous to acoustic plasmons [12] in multiband metals with multiply connected Fermi surfaces, as well as in multivalley degenerate semiconductors and semimetals [13–15].

It was shown in [9] that the small-angle inelastic electron scattering from the long-wavelength collective charge-density fluctuations (CDFs) in MO cuprates with extended SPSs in their 2D-band spectra results in weakening of the screened Coulomb repulsion in the

range of small transferred momenta  $\mathbf{q}$ . In conjunction with the strong in-layer anisotropy of the quasiparticle spectrum containing extended SPSs, the minimum of Coulomb repulsion at small  $q$  (and the maximum of repulsion at the corners of the Brillouin zone [7]) gives rise to the effective electron–electron attraction in the  $d$ -wave Cooper-pairing channel.

It is demonstrated in this work that the anisotropic attraction caused by the exchange of virtual long-wavelength CDFs, much like the electron–plasmon interaction (EPI) in the isotropic  $s$ -wave channel (see [16, 17]), is strongly enhanced due to the many-particle Coulomb correlations of the type of local-field effects described by Coulomb vertex functions  $\Gamma_c$ . As a result, this “Coulomb” mechanism of Cooper pairing may provide, even in the absence of other (electron–phonon or electron–magnon) interactions, high critical temperatures  $T_c \geq 100$  K of transition to the superconducting state with the  $d_{x^2-y^2}$  symmetry of the order parameter in optimum-doped MO cuprates.

**2.** We start with the equations of the standard theory of superconductivity for the normal and anomalous self-energy parts in the strong-coupling approximation [18], in which only the screened Coulomb interaction with retardation effects caused by the exchange of virtual plasmons (long-wavelength CDFs) is taken for the electron–electron interaction.

Since the collective plasmon modes with frequencies  $\Omega \gg T_c$  make the main contribution to the effective interaction between quasiparticles, the renormalized anisotropic superconducting gap at the Fermi surface obeys the integral equation whose linearized form near

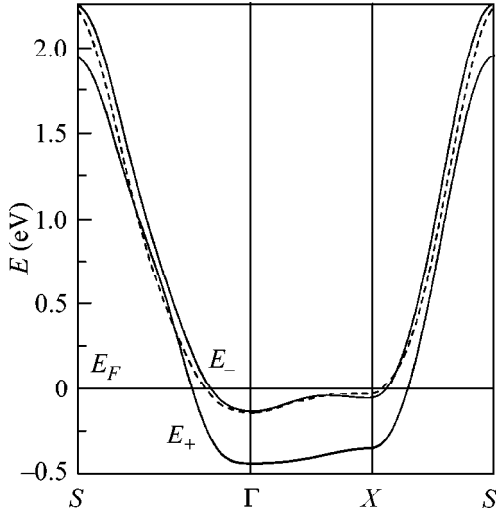


**Fig. 1.** Bonding  $E_+(k_x, k_y)$  and antibonding  $E_-(k_x, k_y)$  branches (solid lines) of the empirical spectrum suggested in [11] for the cuprate 2D layers of Y123 crystal. The  $\tilde{E}_-(k_x, k_y)$  spectrum renormalized by the electron–electron interactions is shown by the dashed curve.

the critical temperature in the strong-coupling approximation is

$$Z_c(\mathbf{k}_\parallel, 0)\Delta(\mathbf{k}'_\parallel) = -\frac{1}{2} \int \frac{d^2\mathbf{k}'_\parallel}{(2\pi)^2} \frac{\Delta(\mathbf{k}'_\parallel)}{\tilde{\xi}(\mathbf{k}'_\parallel)} \langle \tilde{V}_c(\mathbf{k} - \mathbf{k}', 0) \rangle_\perp \times \Gamma_c^2(\mathbf{k}_\parallel, 0; \mathbf{k}_\parallel - \mathbf{k}'_\parallel, 0) \text{Th} \frac{\tilde{\xi}(\mathbf{k}'_\parallel)}{2T_c}. \quad (1)$$

Here,  $Z_c(\mathbf{k}_\parallel, 0)$  is the renormalized Coulomb factor (at the Fermi surface) arising due to the retarded EPI;  $\tilde{\xi}(\mathbf{k}_\parallel) = \xi(\mathbf{k}_\parallel)/Z_c(\mathbf{k}_\parallel, 0)$  is the renormalized energy (measured from the Fermi level) of electrons with in-plane longitudinal momentum  $\mathbf{k}_\parallel$ ;  $\Gamma_c(\mathbf{k}_\parallel, 0; \mathbf{k}_\parallel - \mathbf{k}'_\parallel, 0)$  is the Coulomb vertex function in the static limit; and  $\langle \tilde{V}_c(\mathbf{k} - \mathbf{k}', 0) \rangle_\perp$  is the averaged (over the transferred transverse momentum  $q_\perp$ ) matrix element of the static screened Coulomb repulsion (SCR).

It should be emphasized that the square of the normal Coulomb vertex  $\Gamma_c$  appears on the right-hand side of Eq. (1) because of taking account of the anomalous Coulomb vertices  $\tilde{\Gamma}_c$  (see [19, 20]); it leads to a substantial enhancement of both Coulomb repulsion and effective electron–electron attraction caused by the retarded EPI.

The vertex function  $\Gamma_c$  cannot be exactly calculated because of the lack of a small parameter for the Coulomb interaction in real systems. For this reason, to make an estimation for the Coulomb vertex at nonzero temperatures  $T \neq 0$ , we use the Nambu approximation [21, 22], which satisfies Ward's identity [23] at  $\mathbf{q} \rightarrow 0$

and has the following form in the Matsubara representation:

$$\Gamma_c(\mathbf{k}_\parallel, \omega_n; \mathbf{q}_\parallel, \nu_m) = \frac{1}{2} [Z_c(\mathbf{k}_\parallel + \mathbf{q}_\parallel, \omega_n + \nu_m) + Z_c(\mathbf{k}_\parallel, \omega_n)], \quad (2)$$

where

$$Z_c(\mathbf{k}_\parallel, \omega_n) = 1 - \frac{\text{Im}\Sigma_c(\mathbf{k}_\parallel, \omega_n)}{\omega_n}, \quad (3)$$

and  $\Sigma_c$  is the normal self-energy part determined by the equation

$$\Sigma_c(\mathbf{k}_\parallel, \omega_n) = -\frac{T}{a^2 N^2} \sum_{\omega'_n} \sum_{\mathbf{k}'_\parallel} \langle \tilde{V}_c(\mathbf{k} - \mathbf{k}', \omega_n - \omega'_n) \rangle_\perp \times G \langle \mathbf{k}'_\parallel, \omega'_n \rangle \Gamma_c(\mathbf{k}_\parallel, \omega_n; \mathbf{k} - \mathbf{k}', \omega_n - \omega'_n). \quad (4)$$

In Eq. (4),  $\nu_m = 2m\pi T$  and  $\omega_n = (2n + 1)\pi T$  are the discrete frequencies of bosons and fermions, respectively ( $m, n = 0, \pm 1, \pm 2, \dots$ );  $a$  is the lattice constant;  $N^2$  is the number of discrete values of momentum within the first Brillouin zone;  $G(\mathbf{k}_\parallel, \omega_n)$  is the one-electron Green's function; and  $\langle \tilde{V}_c(\mathbf{k} - \mathbf{k}', \omega_n - \omega'_n) \rangle_\perp$  is the averaged matrix element of retarded SCR; it is determined by the renormalized electron polarization operator:

$$\tilde{\Pi}_c(\mathbf{q}_\parallel, \nu_m) = -\frac{2T}{a^2 N^2} \sum_{\omega_n} \sum_{\mathbf{k}_\parallel} G(\mathbf{k}_\parallel, \omega_n) \times G(\mathbf{k}_\parallel + \mathbf{q}_\parallel, \omega_n + \nu_m) \Gamma_c(\mathbf{k}_\parallel, \omega_n; \mathbf{q}_\parallel, \nu_m). \quad (5)$$

The set of Eqs. (2)–(5) was numerically solved by the self-consistent fast Fourier transform method on a grid containing  $N \times N = 4096$  points of the 2D Brillouin zone and up to 2048 points at the imaginary frequency axis, followed by analytic continuation to the real  $\omega$  axis using multipoint Padé approximants.

The antibonding  $E_-(k_x, k_y)$  branch of the empirical 2D band spectrum suggested in [11] for the cuprate  $\text{CuO}_2$  layers (Fig. 1) on the basis of the ARPES data on Y123 crystals was chosen as the starting electronic spectrum  $E(\mathbf{k}_\parallel)$ .

The renormalized electronic spectrum  $E_-(k_x, k_y)$  corresponding to the pole of the one-electron Green's function and shown in Fig. 1 by the dashed line is characterized by pronounced extended SPSs near the symmetric points  $(\pm\pi, 0)$  and  $(0, \pm\pi)$ .

Figure 2 shows the static Coulomb vertex  $\Gamma_c(\mathbf{k}_\parallel, 0; \mathbf{q}_\parallel, 0)$  as a function of momentum for  $k_x = k_y$  and  $k = k_F$  ( $k_F$  is the Fermi momentum). The dependence of  $\Gamma_c$  on  $(q_x, q_y)$ , as obtained from the empirical spectrum [11] using approximation (2), is displayed in Fig. 2a. For comparison, the analogous dependence for the  $1 + \Gamma_c^{(1)}$  quantity is shown in Fig. 2b, where  $\Gamma_c^{(1)}$  is

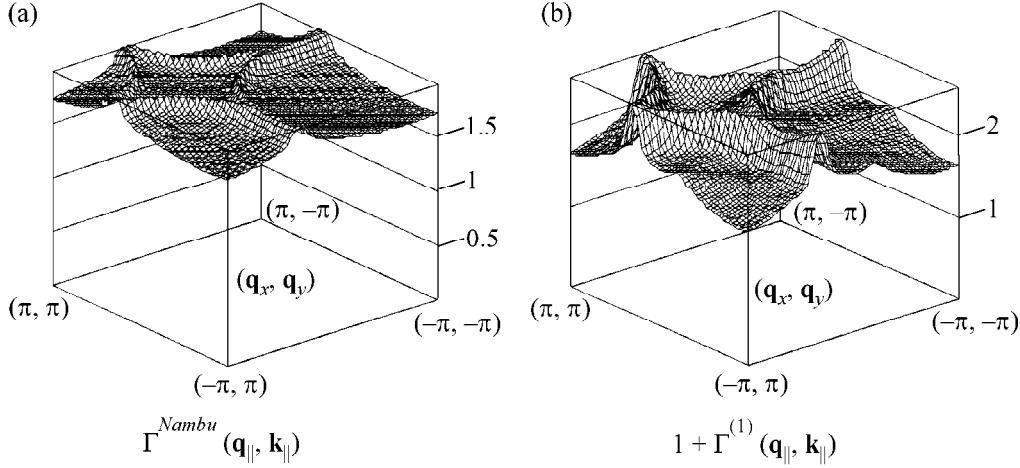


**Fig. 2.** Coulomb vertex function vs.  $q$  for  $k_x = k_y$  and  $k = k_F$  in the static limit. (a) Nambu approximation (2) for  $\Gamma_c(\mathbf{k}_\parallel, \mathbf{q}_\parallel)$ ; (b)  $1 + \Gamma_c^{(1)}(\mathbf{k}_\parallel, \mathbf{q}_\parallel)$ .

the leading correction to the Coulomb vertex function in the renormalized perturbation theory:

$$\Gamma_c^{(1)}(\mathbf{k}_\parallel, \omega_n; \mathbf{q}_\parallel, \nu_m) = \frac{T}{a^2 N^2} \sum_{\omega'_n} \sum_{\mathbf{k}'_\parallel} \tilde{V}_c(\mathbf{k}_\parallel - \mathbf{k}'_\parallel, \omega_n - \omega'_n) \times G(\mathbf{k}'_\parallel + \mathbf{q}_\parallel, \omega'_n + \nu_m) G(\mathbf{k}'_\parallel, \omega'_n). \quad (6)$$

One can see that both approximations, the Nambu approximation (2) and the inclusion of leading correction (6), provide similar momentum dependencies for  $\Gamma_c(\mathbf{k}_\parallel, 0; \mathbf{q}_\parallel, 0)$  and almost the same average values for  $\bar{\Gamma}_c$ , evidencing a rather fast convergence of the diagrammatic series for  $\Gamma_c$ .

The calculations indicate that the variations of  $Z_c$  and  $\Gamma_c$  do not exceed 10% within the Brillouin zone. Because of this, the functions  $Z_c$  and  $\Gamma_c$  in Eqs. (1) and (5) can be replaced, with good accuracy, by the  $\bar{Z}_c$  and  $\bar{\Gamma}_c$  values averaged over the Brillouin zone. In doing so, one can use Eqs. (2) and (3) and set

$$\bar{\Gamma}_c = \bar{Z}_c \equiv (1 + \bar{\lambda}_{pl}), \quad (7)$$

where  $\bar{\lambda}_{pl}$  is the averaged dimensionless coupling constant describing the isotropic EPI in the  $s$ -wave Cooper-pairing channel (see [16, 17]). The value of  $\bar{\Gamma}_c = \bar{Z}_c \approx 2.2$  obtained by our computations corresponds to the isotropic plasmon coupling constant  $\bar{\lambda}_{pl} \approx 1.2$ .

**3.** The superconducting transition critical temperature is determined by the eigenvalues of the linearized integral Eq. (1) for the gap at the Fermi surface. After

transition to the angular variables, it can be recast in the form

$$\Delta(\varphi) = \bar{\Gamma}_c \int_0^{2\pi} \frac{d\varphi'}{2\pi} K(\varphi, \varphi') \Delta(\varphi') \int_0^{\tilde{E}_F} \frac{d\xi}{\xi} \text{Th} \frac{\xi}{2T_c}, \quad (8)$$

where

$$K(\varphi, \varphi') = -v(\varphi') \tilde{V}_e(\varphi, \varphi'). \quad (9)$$

Here,  $\Delta(\varphi) \equiv \Delta(\mathbf{k}_F(\varphi))$ ,  $\tilde{E}_F$  is the renormalized Fermi energy;  $\varphi$  and  $\varphi'$  are the angles between, respectively,  $\mathbf{k}_\parallel$  and  $\mathbf{k}'_\parallel$  and the crystallographic  $a$  (or  $b$ ) axis lying in the layer plane;  $v(\varphi')$  is the angle-dependent electronic density of states (DOS) at the anisotropic Fermi sur-

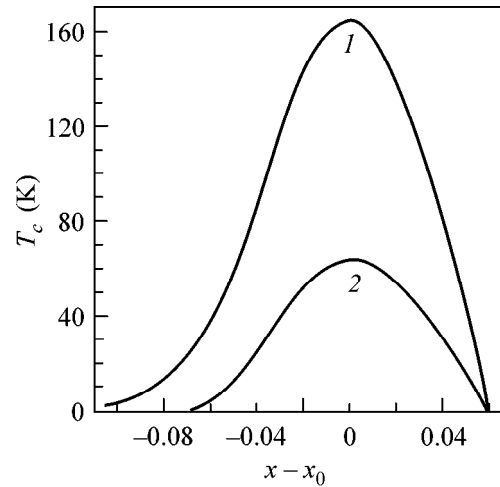


**Fig. 3.**  $T_c$  as a function of  $x$  at  $\varepsilon_\infty = (1)$  4 and (2) 6.

face; and  $\tilde{V}_c(\varphi, \varphi')$  is the  $q_z$ -averaged matrix element of the static SCR.

Equation (8) was solved by the Fourier series expansion of the  $K(\varphi, \varphi')$  kernel and the  $\Delta(\varphi)$  gap [6]. Due to two effects, namely, (a) the suppression of static SCR for small transferred momenta in the scattering from the long-wavelength CDFs (see [8, 9]) and (b) the strong anisotropy of the electronic spectrum of the 2D layers, with DOS maxima in the regions of extended SPSs, the structure of anisotropic kernel (9) is such that its largest positive eigenvalue (corresponding to the attraction) provides the  $d_{x^2-y^2}$  symmetry for the gap, whereas the  $s$  channel is suppressed by the strong Coulomb repulsion. It should be emphasized that the  $\bar{\Gamma}_c$  multiplier in Eq. (8) is responsible for the substantial enhancement of the electron–electron attraction in the  $d$ -wave Cooper-pairing channel.

In Fig. 3,  $T_c$  is shown as a function of the reduced concentration  $x$  of the doped charge carriers (holes) for different values of the high-frequency dielectric constant  $\epsilon_\infty$ , which is determined by the interband electron transitions. The curves have a maximum at the point  $x = x_0$  corresponding to the Fermi level positioning near the bottom of extended SPSs and are in qualitative agreement with the experimental data on MO cuprates.

In summary, even without invoking additional Cooper-pairing (phonon, magnon, etc.) mechanisms, the “Coulomb” mechanism of HTSC with the  $d$ -wave order parameter provides a rather high maximum (optimum-doping) critical temperature  $T_c \geq 100$  K as a result of the increase (more than twofold, as compared to the random-phase approximation [8, 9]) in the coupling constant owing to the many-particle Coulomb correlations (of the type of local-field effects) described by the vertex function  $\Gamma_c$ .

#### REFERENCES

1. D. A. Wollman, D. J. van Harlingen, J. Giapintzakis, *et al.*, Phys. Rev. Lett. **74**, 797 (1995).
2. C. C. Tsuei, J. R. Kirtley, Z. F. Ren, *et al.*, Nature **387**, 481 (1997).

3. M. R. Norman, M. Randeria, H. Ding, *et al.*, Phys. Rev. B **52**, 15107 (1995).
4. D. J. Scalapino, E. Loh, and J. E. Hirsch, Phys. Rev. B **35**, 6694 (1987).
5. A. J. Millis, H. Monien, and D. Pines, Phys. Rev. B **42**, 167 (1990).
6. T. Moriya, Y. Takahashi, and K. Ueda, J. Phys. Soc. Jpn. **59**, 1905 (1990).
7. P. Monthoux and D. Pines, Phys. Rev. B **47**, 6069 (1993).
8. E. A. Pashitskii, V. I. Pentegov, A. V. Semenov, and E. Abraham, Int. J. Mod. Phys. B **12**, 2946 (1998).
9. É. A. Pashitskiĭ, V. I. Pentegov, A. V. Semenov, and E. Abraham, Pis'ma Zh. Éksp. Teor. Fiz. **69**, 703 (1999) [JETP Lett. **69**, 753 (1999)].
10. K. Gofron, J. C. Campuzano, A. A. Abrikosov, *et al.*, Phys. Rev. Lett. **73**, 3302 (1994).
11. M. C. Schabel, C.-H. Park, A. Matsuura, *et al.*, Phys. Rev. B **57**, 6090 (1998).
12. D. Pines, Can. J. Phys. **34**, 1379 (1956).
13. O. V. Konstantinov and V. I. Perel', Fiz. Tverd. Tela (Leningrad) **9**, 3061 (1967).
14. É. A. Pashitskiĭ, Zh. Éksp. Teor. Fiz. **55**, 2387 (1968) [Sov. Phys. JETP **28**, 1267 (1968)].
15. J. Ruvalds, Adv. Phys. **30**, 677 (1981).
16. É. A. Pashitskiĭ, Pis'ma Zh. Éksp. Teor. Fiz. **57**, 639 (1993) [JETP Lett. **57**, 648 (1993)]; Zh. Éksp. Teor. Fiz. **103**, 867 (1993) [JETP **76**, 425 (1993)].
17. É. A. Pashitskiĭ, Fiz. Nizk. Temp. **21**, 995 (1995) [Low Temp. Phys. **21**, 763 (1995)]; Fiz. Nizk. Temp. **21**, 1091 (1995) [Low Temp. Phys. **21**, 837 (1995)].
18. G. M. Éliashberg, Zh. Éksp. Teor. Fiz. **38**, 966 (1960) [Sov. Phys. JETP **11**, 696 (1960)]; Zh. Éksp. Teor. Fiz. **39**, 1437 (1960) [Sov. Phys. JETP **12**, 1000 (1960)].
19. O. V. Dolgov and E. G. Maksimov, Usp. Fiz. Nauk **138**, 95 (1982) [Sov. Phys. Usp. **25**, 688 (1982)].
20. O. V. Dolgov, D. A. Kirzhnits, and E. G. Maksimov, Rev. Mod. Phys. **53**, 81 (1981).
21. Y. Nambu, Phys. Rev. **117**, 648 (1960).
22. Y. Takada, J. Phys. Chem. Solids **54**, 1779 (1993).
23. J. M. Luttinger and J. C. Ward, Phys. Rev. **118**, 1417 (1960).

*Translated by V. Sakun*